CONTRACTOR REPORT

SAND83–7108
Unlimited Release
UC–94c,b

Development of a Circulating Zinc–Bromine Battery Phase II – Final Report

R. Bellows, H. Einstein, P. Grimes, E. Kantner,
P. Malachesky, K. Newby, H. Tsien, A. Young
Exxon Research and Engineering Company
Advanced Energy Systems Laboratory
Linden, NJ 07036

Prepared by Sandia National Laboratories Albuquerque, New Mexico 87185
and Livermore, California 94550 for the United States Department of Energy
under Contract DE-AC04-76DP00789.

Printed October 1983

Issued by Sandia National Laboratories, operated for the United States Department of Energy by Sandia Corporation.

Printed in the United States of America
Available from
National Technical Information Service
U.S. Department of Commerce
5285 Port Royal Road
Springfield, VA 22161

NTIS price codes
Printed copy: A08
Microfiche copy: A01

EXXON RESEARCH AND ENGINEERING COMPANY
CORPORATE RESEARCH LABORATORIES

DEVELOPMENT OF A CIRCULATING ZINC-BROMINE BATTERY PHASE II - FINAL REPORT

EXXON RESEARCH AND ENGINEERING COMPANY

R. Bellows - Project Head
H. Einstein
P. Grimes
E. Kantner
P. Malachesky
K. Newby
H. Tsien
A. Young

April 1982

Advanced Energy Systems Laboratory

P. O. BOX 45 ■ LINDEN, NEW JERSEY 07036

TABLE OF CONTENTS

LIST OF FIGURES

LIST OF TABLES

Abstract

This report summarizes Phase II of a multi-phase program aimed at developing Exxon's circulating zinc-bromine battery into an advanced energy storage system. This effort was cost shared by Exxon Enterprises and DOE/Sandia. Previous work at Exxon had developed a basic zinc-bromine battery system approach. This approach utilizes carbon-plastic electrodes in a bipolar stack design, a circulating electrolyte with separable bromine complexes, and shunt current protection.

Phase II was highlighted by the successful scale-up and demonstration of a 20 kWh zinc-bromine battery module. Important technology improvements were demonstrated in the areas of extended life cycling, low cost stack technology, high power/high efficiency supported electrolytes, and system auxiliaries. The basic technology was augmented via increases in parametric testing, materials testing,and electrolyte studies.

Production cost estimates from Phase I ($28/kWh in 1980$) were projected to an OEM price of $37/kWh using the A. D. Little costing method. A revised cost analysis, using an approach in which all battery components are produced at the battery manufacturing facility (as compared to the original analysis based on purchase of cell components from plastics fabricators) showed essentially the same factory costs as the original estimate (~$28/kWh).

A design has been developed for a prototype 20 kWh energy storage system which will be delivered to Sandia National Laboratories in 1983 near the completion of Phase III. Project effort is continuing to show steady progress toward the attainment of this goal.

Summary

Exxon Research and Engineering Company has been developing an advanced battery system based on the zinc/bromine battery couple. Projected performance of the system makes it suitable for applications such as photovoltaic energy storage, bulk energy storage, and vehicle traction. This report summarizes Phase II of a multi-phase effort to develop Exxon's circulating zinc-bromine battery into an advanced energy storage system. The effort was cost shared by Exxon Enterprises and DOE/Sandia on Contract 40-0483. This report covers development work between February 7, 1981 and February 5, 1982.

The goals of Phase II were to incorporate the basic battery technology into a 20 kilowatt hour, multi-stack demonstrator, as well as to broaden the base technology. The 20 kWh system represents a suitable scale for residential photovoltaic storage and small electric vehicles. The goals of Phase III will be to deliver a self-contained optimized 20 kWh system to Sandia National Laboratories for testing and evaluation while continuing to expand the base battery technology.

The structure of the report corresponds section-by-section to the structure of major tasks outlined in the Phase II statement of work.

Phase II was marked by steady progress in all program areas. System scale-up to 20 kWh module proceeded smoothly, demonstrating steady performance for over 50 cycles. The six submodules in this battery utilized 80V stacks, each comprised of 52 bipolar cells. This test demonstrated all key system technical components such as bipolar carbon-plastic electrodes, separable bromine complexing agents, circulating electrolytes, microporous separators, and shunt current protection. The testing also provided new information on the operation of large systems in terms of maintenance, thermal balancing, and parallel multistack operation.

The two-piece unit cell design, the basis of cost projections for the stacks, was reduced to practice with the successful injection molding of posted microporous separators and the co-extrusion of electrodes. Promising manufacturing approaches for the cathode activation layer were developed which should remove this bottleneck in electrode production. The complete two-piece electrode technology was tested in 4 to 8 cell stacks during Phase II and showed performance generally comparable to the previous injection-molded electrode components.

Four automatic cycling stations were constructed which allowed the more rapid accumulation of life cycling data. Two 500-Wh battery stacks demonstrated over 300+ deep cycles of stable performance as opposed to 150+ deep cycles at the end of Phase I. Another 500-Wh stack demonstrated 1400+ cycles at lower loadings (5-30 mAh/cm^2).

In the area of electrolyte studies, analytical techniques were developed which allowed a detailed mass balance study to be performed on both circulating electrolytes during charge and discharge. Work with supported electrolytes showed higher power capability due to lower resistive polarizations. These electrolytes were subjected to a rapid cycling between charge and discharge as required, for example, in electric vehicle batteries with regenerative braking (the J227aD driving cycle).

Conceptual design of the 20-kWh deliverable battery, based on two parallel stacks, each with 78 bipolar cells, has continued to evolve. A new scaled-up electrode design (1200 cm^2) is being readied for eventual testing during Phase III. A stand-alone microprocessor battery controller has also been designed and will be tested during Phase III. A simplified version of this microprocessor will control the final Phase III deliverable.

Cost studies carried out during Phase II have led to increased confidence in the manufacturing cost projections from Phase I ($28/kWh in 1980$). The A. D. Little costing method, assuming large scale production, projects an OEM selling price of $40/kWh. However, as confidence in the battery technology and the cost estimates increases, the assessment of risk and uncertainty in the evolving battery market areas, such as photovoltaic and bulk energy storage and electric vehicle, is also increasing. This increasing risk probably pushes the development of large markets for energy storage systems beyond 1990. Recent technical progress indicates that the present zinc-bromine battery technology could be adapted to all of these various developing markets with some modifications.

SECTION 0

Introduction

0.1 Introduction to Report Content

This work represents the second phase of a three phase program whose goal is the development of Exxon's circulating zinc-bromine battery for advanced energy storage applications. This program built on a foundation of technology that had previously been developed by Exxon Research and Engineering Company. The present effort is cost shared by Exxon and DOE/Sandia (Contract 40-0483). Phase II had several goals among which are: continued development of the base zinc-bromine technology, conceptual development of a design for a 20-kWh photovoltaic battery, and the demonstration of a multi-stack 20-kWh battery, an intermediate scale-up on the path to a final 20-kWh design.

Steady and timely progress was made toward those goals. At the conclusion of Phase II, a number of accomplishments deserved mention, namely:

PHASE II HIGHLIGHTS

- Large Battery (20 kWh) Demonstration
  - Test Station Completed
  - 70 Plus Cycles Stable Performance
- Two Piece Cell Design Concept
  - Co-Extrusion Perfected
  - Injection Molded Daramic Successful
  - Cell Testing Successful
- Life Extension - 4 Automatic Cycling Stations Built
  - 1400 Shallow Cycles (5-30 mAh/cm^2)
  - 300+ Deep Cycles (60 mAh/cm^2)
- Improved Battery Capability and Understanding
  - Supported Electrolyte - Higher Efficiency, Power, Lower Temperature
  - Rapid Charge/Discharge Alternation (Vehicle Simulation)
  - Mass Balances Completed
- Prototype Development
  - 1200 cm^2 (12 dm^2) Electrode Designed
  - Battery Controller under Construction
  - PV Prototype Conceptual Design Completed

The structure of this final report follows the general outline of major tasks that were delineated in the original Phase II Work Statement. The report includes overall Phase II progress and concludes at the end of Phase II activities. This section has been added to furnish general information on the Phase I program and on the operation of Exxon's circulating zinc-bromine battery to readers unfamiliar with our recent progress. (A historical perspective of Exxon's zinc-bromine battery appears in the Phase I final report.[1])

0.2 Zinc-Bromine Battery System Description

The Exxon zinc-bromine battery is based on a battery module with a flowing electrolyte and utilizes two recent developments: a reversible liquid bromine complexing agent and conductive carbon-plastic technology. Previous attempts to develop the zinc-bromine battery have failed because of problems with self-discharge due to bromine diffusion between electrodes, irregular and dendritic zinc growth, and corrosion problems due to the high reactivity of bromine. In the present approach, self-discharge is controlled by use of a bromine complexing agent to store bromine outside of the cell. Electrolyte circulation gives uniform zinc deposition. Corrosion is avoided by the use of the conductive carbon-plastic and other plastic components which are bromine-resistant. In addition, carbon-plastic components provide a low cost, easily mass-produced battery module.

Advanced battery designs, based on the circulating electrolyte concept, have been proposed for various couples, such as lead-acid, zinc-nickel, iron-nickel, zinc-chlorine and zinc-bromine. Electrolyte circulation is generally useful for feeding reactants, removing products, assisting thermal management, and homogenizing the electrolyte. Although electrolyte circulation increases design complexity, it frequently allows better performance and higher specific energies. A particular advantage in the zinc-bromine battery is improved uniformity of the zinc plating during charging.

A schematic of a circulating zinc-bromine battery is shown in Figure 0-1. The system has three main components. The principal component is the electrochemical module, where the actual electrochemistry takes place. The second component is the circulating electrolyte, an aqueous solution of zinc bromide and the bromine complexing agent, which is circulated in two streams through the electrochemical module. The third component is the system of pumps and reservoirs which store and circulate the electrolyte. The operation of the zinc-bromine battery is easily understood by following a typical charge/discharge cycle. During charge, zinc is plated at the negative electrode and bromine is evolved at the positive electrode. Bromine reacts with the complexing agent to form a second phase, indicated by dots in Figure 0-1. This bromine-rich phase is circulated out of the electrochemical module and is separated by gravity in the catholyte reservoir. Long-term charge retention is excellent because the bromine is stored remotely from the zinc. During discharge, the catholyte valve is opened and the bromine complex is fed back to the module. Now, zinc and bromine electrochemically react to form the original zinc bromide solution, liberating the energy absorbed during charging. The separator prevents direct mixing of the anode and cathode loops, thereby reducing self-discharge during cycling.

ZINC-BROMINE CIRCULATING BATTERY

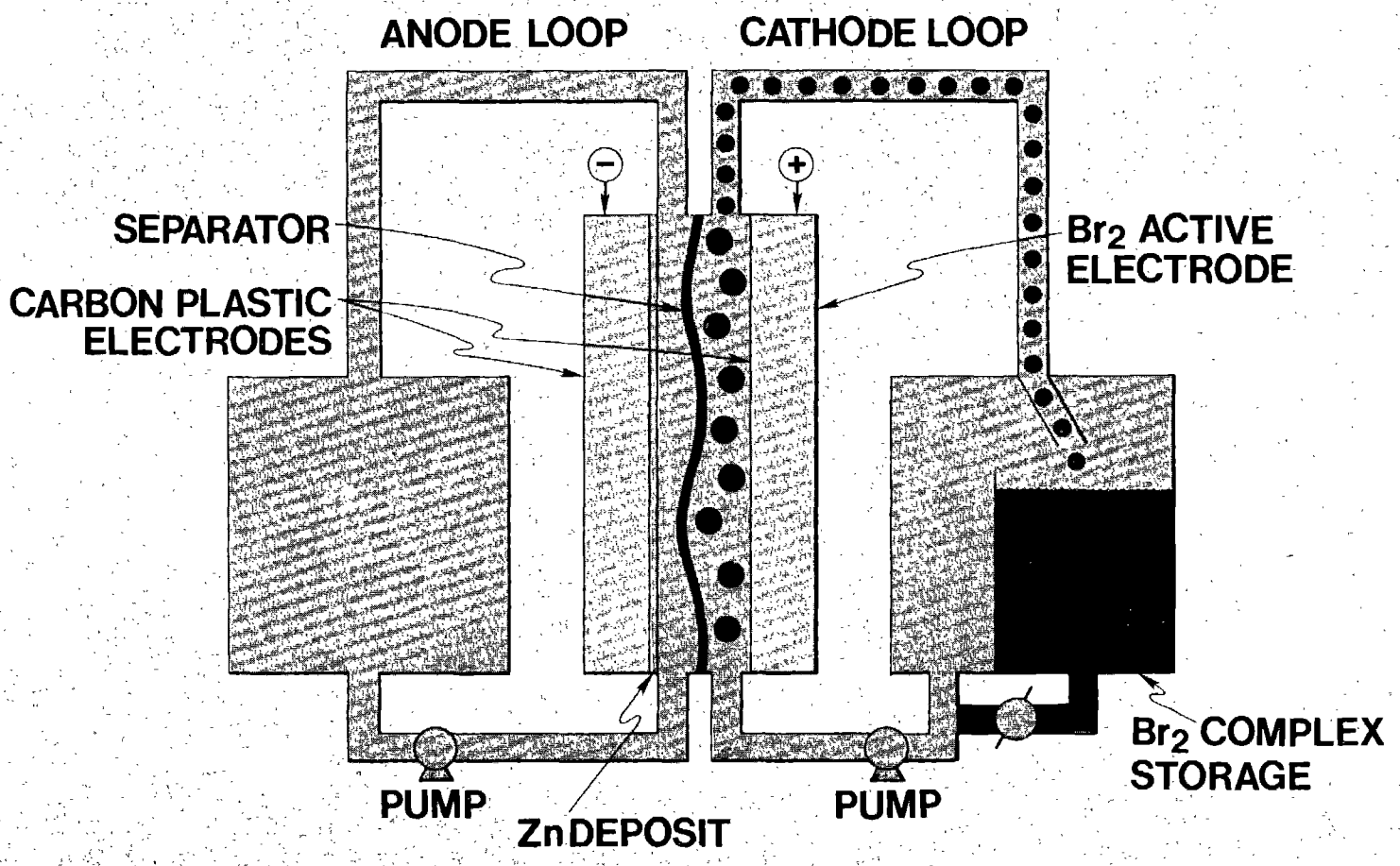

Electrochemical Reactions: $Zn^{\circ} \rightleftharpoons Zn^{++} + 2e^{-}$

$Br_2 + 2e^{-} \rightleftharpoons 2Br^{-}$

Self discharge: $Zn^{\circ} + Br_2 \rightarrow ZnBr_2$

0.3 Component Descriptions

Battery Module - The battery module is nearly all plastic construction, so that the final product can be easily and economically mass-produced. Figure 0-2 shows an expanded view of the present 600 cm^2 battery components, an alternating series of electrodes, plastic screens and separators.

a) Electrodes - Previous zinc-bromine batteries have been plagued by bromine corrosion of metallic electrodes. Even titanium-based electrodes show corrosion pitting, resulting from bipolar shunt currents and/or from cell reversal. The Exxon zinc-bromine battery has avoided this problem by the use of a conductive carbon-plastic composite. The carbon-plastic is used for both the zinc and bromine electrodes. An extra layer of high surface area carbon is added at the Br_2 electrode to increase the reactive surface area. The conductive carbon-plastic is framed with a filled, non-conductive plastic which matches the thermal properties of the carbon-plastic. Flow channels, molded into the non-conductive plastic, uniformly distribute the two flowing electrolytes to each cell. The conductivity of the carbon-plastic (about 1 $(ohm \cdot cm)^{-1}$) is sufficiently high that there is virtually no ohmic loss in the case of bipolar electrodes. The carbon-plastic conductivity is not sufficiently high, however, for efficient monopolar electrodes. Metallic current collectors can be molded into the carbon-plastic to increase lateral conductivity. There is no observable contact resistance between the metal screens and carbon-plastic because of the high contact area and high compressive stresses generated during molding operations. Such composite electrodes have been used in monopolar configurations, and are presently used as end plates on bipolar stacks. The area of the present electrodes is 600 cm^2 but the materials and techniques can be easily scaled to larger dimensions. During Phase II, most bipolar electrodes were fabricated by using injection molding to mold the non-conductive flow frame around "inserts" of the conductive carbon-plastic. End electrodes were compression molded to sandwich metallic current collectors into the carbon-plastic.

b) Screens - Screens of polypropylene or polyethylene separate the electrodes from the membrane. Vexar screens, made by DuPont, are being used presently. The screens keep the electrodes uniformly spaced and provide extra volume for zinc deposition. They promote uniform flow distribution over the electrode face. Recent designs (see Section II) have integrated this component with the separator.

c) Separator - Earlier efforts considered both ion-selective separators and non-selective microporous separators. Ion-selective membranes have a clear-cut coulombic efficiency advantage over porous separator materials. However, porous separator materials are less costly. Depending on the specific battery application, a coulombic efficiency vs cost trade-off may be undertaken with regard to the choice of separator materials. Our recent work has emphasized the use of microporous membranes (Daramic made by W. R. Grace) along with a low cost electrolyte additive which enhances the membrane's ability to retard bromine diffusion.

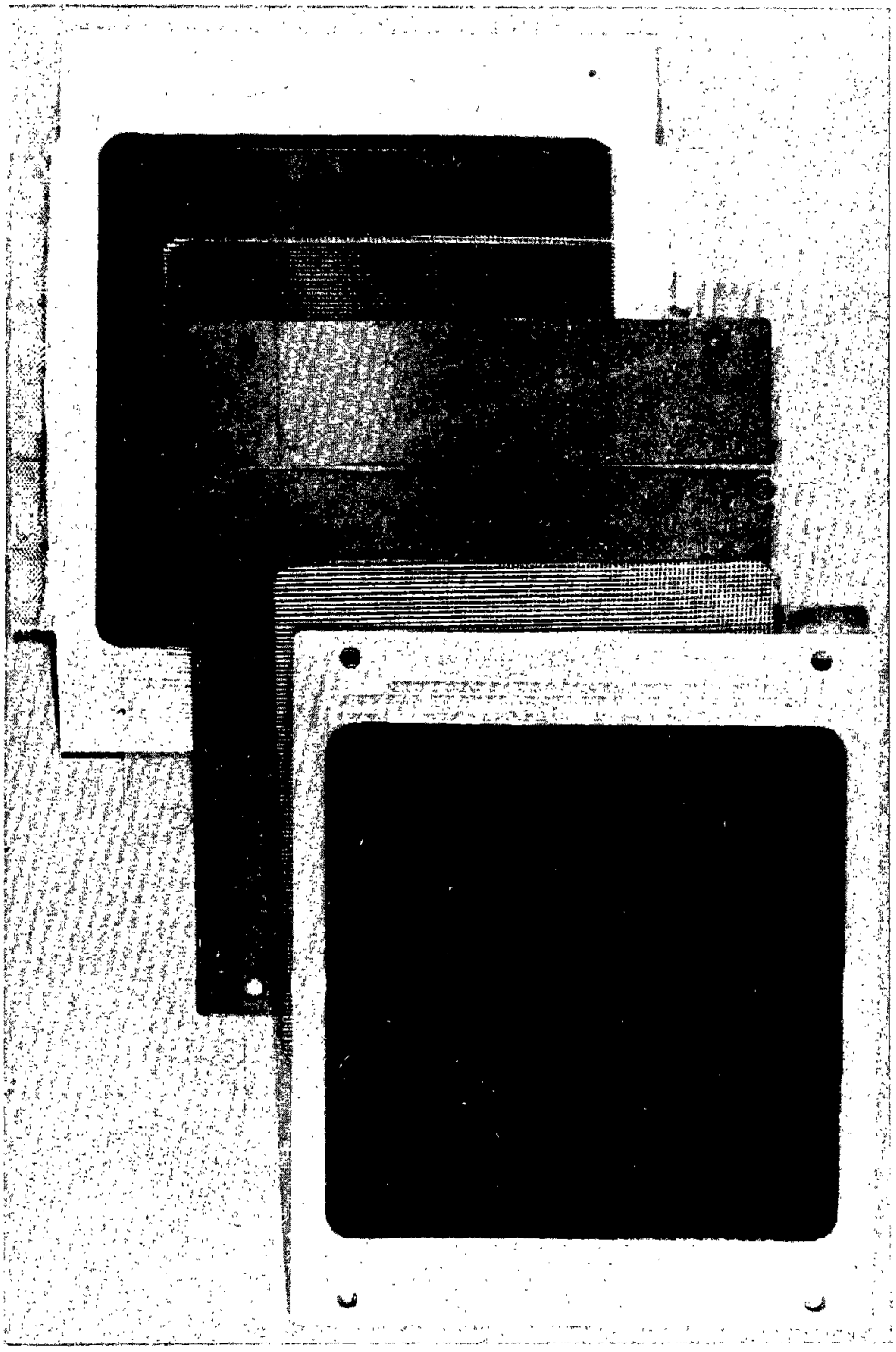

Figure 0-2 500 cm^2 Components

d) End Block - Electrodes, spacers, and membranes can be conveniently assembled into stacks. The ends of each stack are bolted between plastic feed blocks which provide the external manifold connections and hold the electrodes in a uniform compression. Figure 0-3 shows a stack of 52 electrodes manifolded together between end blocks. Protective electrode assemblies are built inside the feed blocks in the vicinity of the feed manifolds.[2,3]

Electrolyte - The zinc-bromine battery system uses an aqueous electrolyte having two active components, zinc bromide salt and a bromine complexing agent. These components are low cost, i.e., they are readily prepared from commercial items. The typical concentration of the electrolyte in the discharged state is: 3 M $ZnBr_2$, and 1 M bromine complexing agent. In typical operation, 70% of the $ZnBr_2$ is converted to Zn^0 and Br_2 at full charge. Efforts during Phase II have shown that supporting electrolytes, such as KCl, reduce resistive polarization.

a) Zinc Bromide is the active ingredient of the electrolyte. It is the participant in the electrode reactions, and it is the major ionic current carrier. Zinc bromide provides a cell voltage of about 1.75 volts. Except for internal electrolyte resistance, there is virtually no cell polarization.

b) The Bromine Complexing Agent[4] is based on quaternary ammonium chemistry. This complexing agent was selected after a screening program which considered several classes of Br_2 complexing agents. The present agent was chosen because of its highly reversible complexing of bromine, superior chemical stability, lack of toxicity, miscibility with zinc bromide solutions, and its potential low cost. The use of a complexing agent reduces the aqueous Br_2 concentration in the aqueous electrolyte by 10 to 60-fold. This retards Br_2 diffusion across the microporous membrane and also reduces Br_2 attack of the plastic components. The complexing agent also reduces H_2 evolution and improves plating at the anode.

Circulation Equipment - The pumps and reservoirs for circulating the zinc-bromine battery system's electrolyte are a distinct departure from standard lead-acid battery technology. The ability to flow and to store the electrolyte external to the cell has many advantages. Flow mixes the electrolyte and reduces the growth of zinc dendrites on the electrodes. Most batteries "gas". A flowing electrolyte removes the gaseous by-products and simplifies cell maintenance. Heat removal is also simpler with a circulating system. Since most of the electrolyte is located external to the cell, the electrode spacing can be reduced, and the cell, therefore, has a lower internal resistance. Power consumption by the circulating system can be designed to be a small fraction of the battery output. Finally, the external storage of Br_2 avoids the basic problem of self-discharge to a large degree.

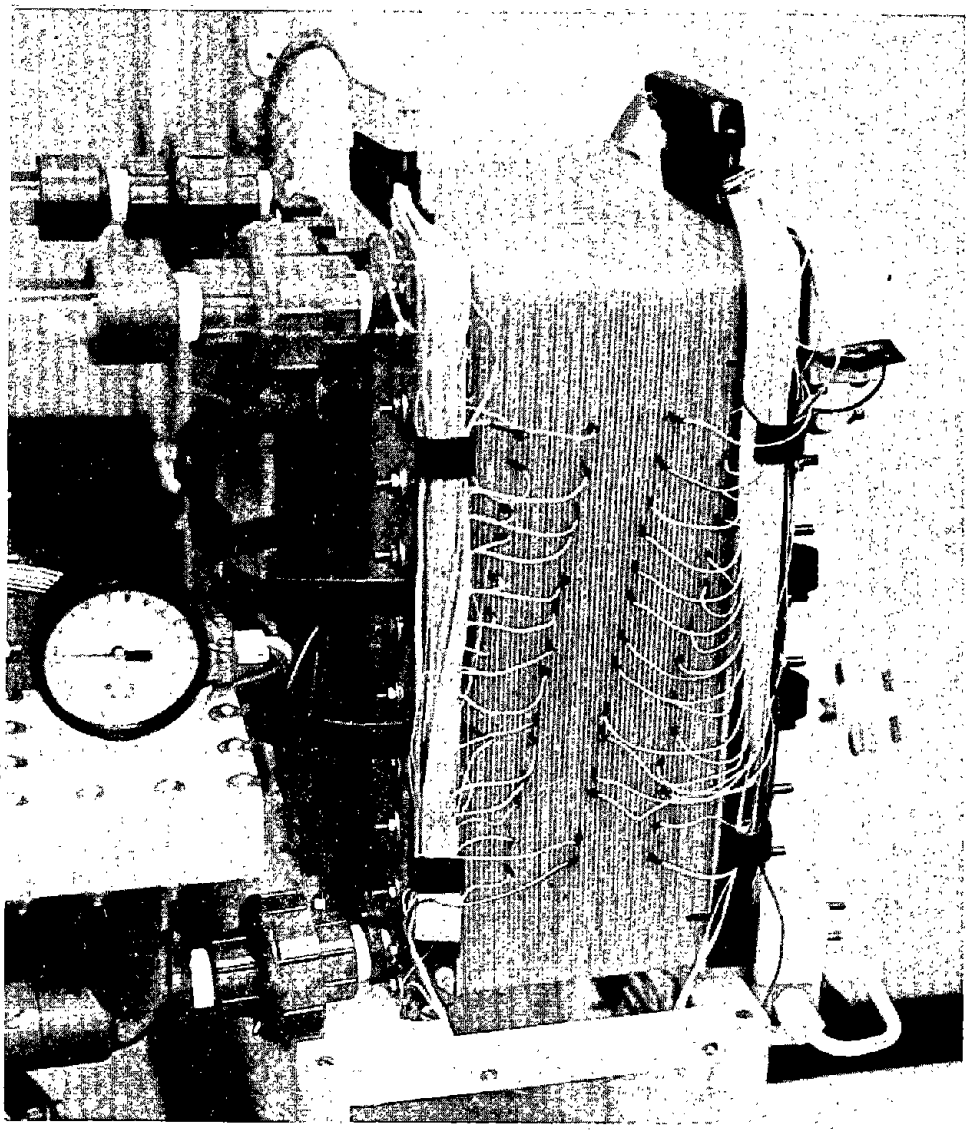

Figure 0-3 52-Cell Stack

a) Pumps - Early small-scale laboratory testing utilized both peristaltic and centrifugal pumps. Practical larger designs favor centrifugal pumps which are magnetically coupled to either ac or dc motors, depending on use. Present small commercial centrifugal pumps can deliver close to 20% overall pumping efficiencies. Larger pumps can be even more efficient.

b) Reservoirs - The present reservoirs are simple polypropylene or polyethylene tanks. The cathode reservoir has separate withdrawals for the aqueous phase and for the dense bromine oil. However, a portion of the bromine oil is recirculated during charge to promote mixing of the two phases and to prevent stratification which decreases the effectiveness of the complexing agent.

In developing this technology, Exxon views the zinc-bromine battery as an advanced candidate for various energy storage and motive power applications. System components are basically in-hand, so that system development does not depend on inventing some as-yet-to-be-developed component. Rather, the progress from this point must be measured in terms of continued performance improvement (duty cycles, life, and cost consideration) and adaptability of the base technology to specific applications.

SECTION I

Design and Cost Analyses

Initial work[1] on Exxon's zinc-bromine battery indicated that it was an attractive advanced battery technology with potentially high performance, long cycle life, and low manufacturing costs. This section describes recent studies concerned with the conceptual design of the system as it evolved during Phase II. Various subsections describe system prototypes such as design of the prototype 20-kWh battery (X-20), design considerations in scaling the electrodes and components up from 600 to 1200 cm^2 area, the development of a computerized simulation of battery performance, and recent updates on system cost projections. The purpose of this section is to document Exxon's current design thinking on the zinc-bromine battery.

I.1 20-kWh (X-20) Prototype Battery Design

Initial consideration of photovoltaic battery applications has focused on domestic grid-connected storage systems with total capacity between 15 and 30 kWh. A desirable system must combine long life, low initial cost, high turn-around efficiencies, high terminal voltage, low maintenance, and various other features. Similar features are also desired in other advanced battery applications such as bulk energy storage and vehicle traction. Therefore, initial Phase I and II efforts were to develop a basic zinc-bromine battery design that can be adapted to various advanced applications with a minor amount of customization. This approach is attractive because it encourages the development of a common core battery technology which minimizes early development costs, and yet can be adapted to various applications. Thus, a larger possible market is created which allows a more rapid entry into volume production.

The 20-kWh (X-20) design approach, shown in Figure I-1, was based on existing bipolar electrodes having an active area of 600 cm^2 (as shown in Figure 0-2). The system building block was a stack of 52 bipolar cells giving a nominal discharge voltage of 80V. Operating at present efficiencies and loadings (90 mAh/cm^2), each stack had a discharge capacity of 3.5 kWh. Running six stacks in parallel produces a net 20 kWh battery. Reservoirs and pumps were located below the stack for a compact design.

This original design approach will be superseded in Phase III by an advanced 20 kWh design (Section I.2) which uses larger electrodes (1200 cm^2), larger stacks (78 cells), and, therefore, fewer modules (2). Cost reductions provide the principal driving force for these recent modifications in the ultimate system design.

I.2 Electrode and Component Scale-Up

The objectives of the electrode and component scale-up studies were:

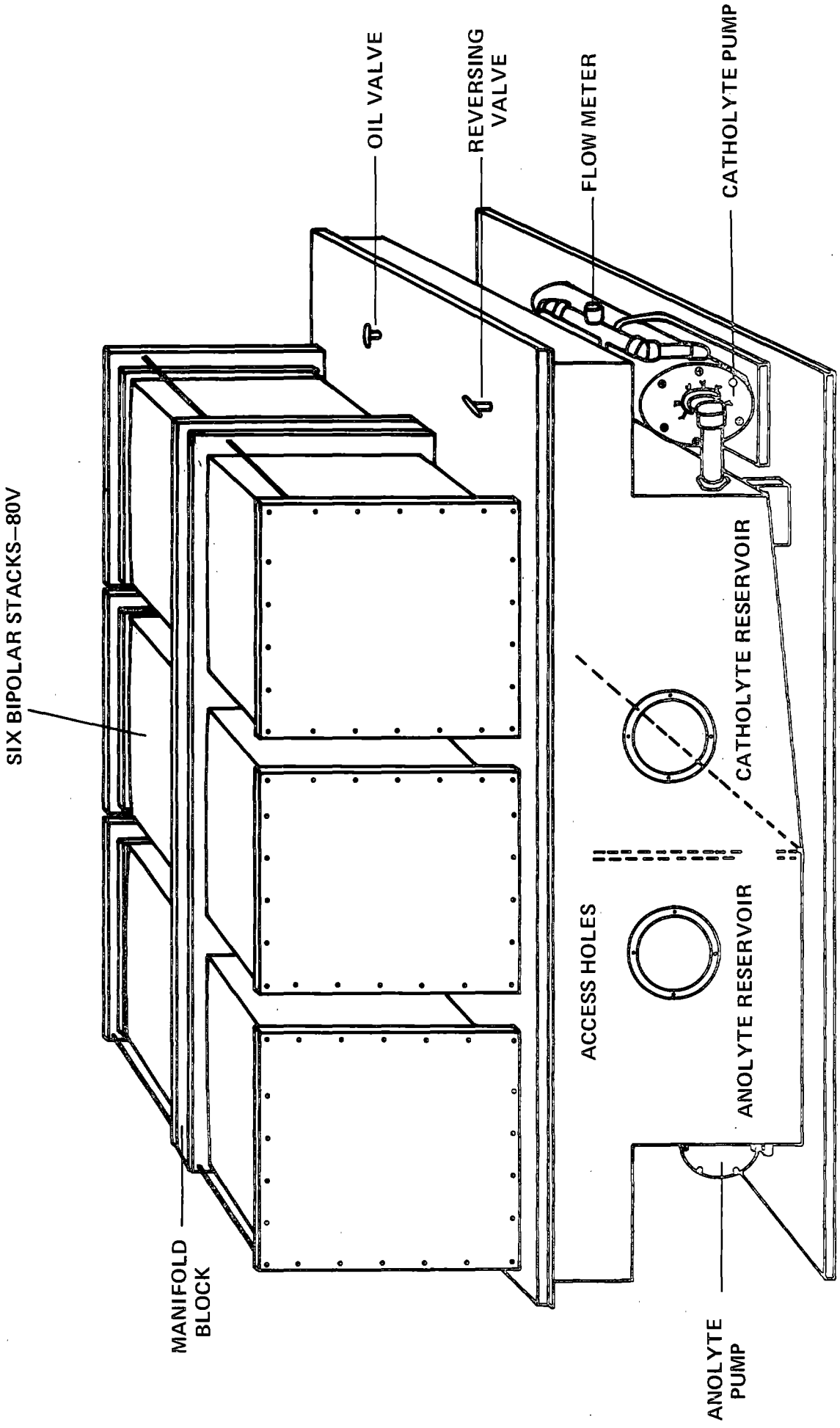

Figure I-1 20-kWh Zinc-Bromine Battery - X-20

- Increased electrode area
- Increased system voltage
- Improved system efficiency
- Reduction of the number of shunt current protection electrodes
- Reduction of the number of battery parts and components
- Reduction of design constraints from hydraulic and electrolytic circuit coupling

In addition, there were several design constraints which had to be considered in the study. These are discussed in the following sections.

I.2.1 Two-Piece Cell Design Factors

Previously, the zinc-bromine battery electrode design had successfully evolved from a 100 cm^2 to a nominal 600 cm^2 active electrode area. A further increase of the nominal area from 600 cm^2 to 1200 cm^2 appeared to be a reasonable and conservative goal.

Previous unit cells such as used in the X-20 design had a six piece construction. A two-piece unit cell construction[1] was desired to reduce the system part count, assembly time and costs. A co-extruded electrode and an injection molded flow frame (around a "posted" separator) represented one direction for a two-piece unit cell construction. Section II.1 further describes the two-piece unit cell and recent progress in developing components based on this design.

A specially constructed die had previously been fabricated to make the co-extruded electrode material. This die produced a ribbon with a 9.5 inch wide carbon-plastic central portion and two non-conductive plastic side bands, each 3 inches wide (Section II.1.1). Continued use of material produced by this die would save development time and costs. Microporous separator material with "posts" of microporous material projecting from the separator face had previously been produced in ribbon form (Section II.1.2). This material was produced on a pilot plant development line which permitted only a limited extension width. The need for wider separators would have required the use of full production lines and would have been prohibitively expensive at this stage. Insert injection molding of flow frames over larger separator material requires a stepwise increase in molding machine capability as the size of the molded part increases. A special machine would be needed for larger sizes. The ability to inject the plastic through thin sections of a mold must also be considered, particularly when the movement of relatively large amounts of plastic material is required.

Therefore, wherever possible, it was desirable to adapt these existing components (co-extruded electrodes and extruded separators) in the scaled-up two piece cell design.

I.2.2 Tunnel Shunt Current Protection Design Factors

Designs for battery scale-up must incorporate lower power shunt current protection methods. The "tunnel" shunt current protection method requires less power than the manifold shunt current protection method. The tunnel protection power requirements are primarily dependent on the resistance and, thus, the geometry of the electrolyte channels connecting the electrolyte manifolds and the cells. Designs which have longer, thinner channels (when consistent with other design factors) are better. The scale-up designs also must consider the hydraulic pathways for the flow electrolyte to minimize the pressure drops through the battery system while allowing uniform flow of electrolyte to the cells.

The methods of elimination of shunt current effects in electrochemical cells with common electrolyte were analyzed and discussed in the Phase I report and in U.S. Patents 4,197,169[2] and 4,312,735[3]. The "manifold" method uses a passage of an appropriate current through the common electrolyte manifold, such that the voltage drop through a manifold segment between two cells is equal to the voltage of a cell, V_c. The protective current, k_o, required for this condition, is:

$$k_o = \frac{V_c}{R_m} = \frac{V_o + IR_e}{R_m} \qquad (I\text{-}1)$$

where:

R_m = resistance of manifold segment
ρ = specific resistance of electrolyte
ℓ = length of manifold segment
A = cross sectional area of manifold
$V_c = V_o + IR_e$ = voltage of a single cell
V_o = open circuit voltage of a single cell
I = cell stack current; plus on charge, minus on discharge
R_e = summation of cell resistances and polarizations

When this condition is met, there is no voltage gradient between the cells and the manifold. The k_o current is independent of the number of cells in series.

The tunnel method incorporates connections (tunnels) between the channels which connect the manifolds and the cells. An appropriate current, t_o, is passed through the common electrolyte network from the first channel/tunnel node to the last channel/tunnel node. Each tunnel dimension and, thus, resistance, is graduated. The graduations are such that the voltage drop through each tunnel, connecting the channels of two adjacent cells, is equal to the voltage of a cell, $V_c = V_o + IR_e$.

The tunnel protective current, t_o, for this condition is:

$$t_o = \frac{V_o + IR_e}{R_m}\left[\frac{(\lambda'^{N/2}-1)^2}{\lambda'^N + 1}\right] + t_{N/2} \qquad (I\text{-}2)$$

where:

$$\lambda' = c/2 + \sqrt{(c/2)^2 - 1} \qquad (I\text{-}3)$$

and

$$c = 2 + R_m/R_c \qquad (I\text{-}4)$$

N = number of cells in series
R_c = resistance of the channel between the tunnel and the manifold
$t_{N/2}$ = current in the mid-tunnel

When these conditions are met, there is no voltage gradient between the cells and the channel/tunnel points and, thus, no current flows from the cells through the common electrolyte.

The difference between the magnitude of protective currents, k_o and t_o, (equations (I-1) and (I-2)) when the central tunnel has large resistance, is mainly the expression in brackets $[(\lambda'^{N/2}-1)^2/(\lambda'^N+1)]$. This expression has a value of less than one.

The t_o current is less when the value of the bracket term is less. For a given number of cells in series, N, the bracket term is smaller when λ' has a lower value. For a given R_m, λ' becomes smaller with a smaller R_m, i.e. larger cross sectional area of manifold (equations (I-3) and (I-4)).

With a given or fixed R_c, the change in the values of t_o, with a decrease in the value of R_m, becomes less and t_o becomes essentially a constant. The relationship of tunnel and manifold protective currents as a function of manifold diameter are shown graphically in Figure I-2 for a particular case of 78 cells and one electrolyte stream (input or output). The value of $t_{N/2}$ was taken as zero in this case.

In the electrolyte network of N cells, there are N-1 manifold segments and N-1 tunnels. The voltage to pass the protective current is thus $(N-1)(V_o + IR_e)$. The protective power, PP, requirements per manifold are thus:

$$PP_m = (N-1)(V_o + IR_e)\, k_o \qquad (I\text{-}5)$$

for the manifold protection, and

$$PP_T = (N-1)(V_o + IR_e)\, t_o \qquad (I\text{-}6)$$

for the tunnel protection. The total protective powers are these values multiplied by the number of manifolds.

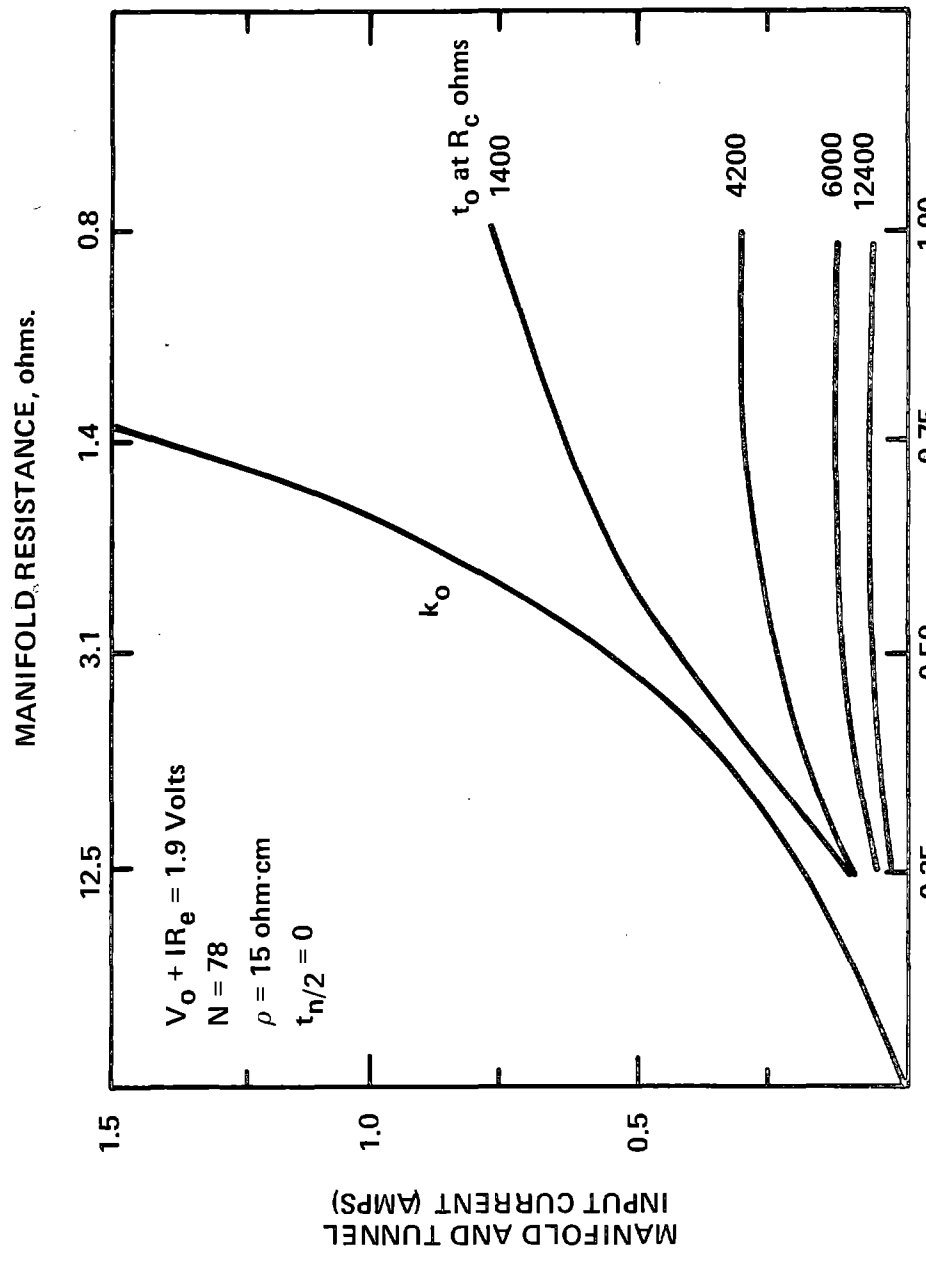

Figure I-2 Protective Current vs Manifold Diameter

I.2.3 Decoupling of Hydraulic and Electrolytic Design Factors

The value of t_o is controlled by the value of R_c at low R_m. If R_c is large, then the manifold cross sectional area (diameter) can have a large value without significantly affecting the tunnel protective current.

Uniform electrolyte supply to and removal from the series of cells requires that the pressure drop in the stack of cells be mainly in the cells. The pressure drop in the manifolds must not be the controlling pressure drop. This requires that the manifold cross sectional area be relatively large for a given number of cells in series, and increases as the number of cells increases.

If manifold protection is used, there is a coupled and direct relationship between the protective current, k_o, and the manifold area. (The current increases with the square of the diameter of the manifold.)

With tunnel protection there is no direct relationship between manifold area and protective current when the channel resistance is relatively large. The protective current value, in this case, becomes essentially independent of manifold area. The hydraulic circuitry and the protective current electrolytic circuitry are decoupled from a design consideration viewpoint.

Systems incorporating tunnel protection require designs with a small R_m/R_c ratio and a relatively large R_c for low auxiliary energy inputs. In the zinc-bromine battery design, this means channels which are long and which have a small cross sectional area. This design must be compatible also with an injection molding tool design which moves plastic through thin cross sections of mold.

I.2.4 Flow Frame Design Factors

Building on past scale-ups, several flow frame designs were considered. Some approaches are illustrated in Figure I-3. The 600 cm^2 size electrode has a square shaped electrode area. Type A design has a square electrode, stretching the present electrode horizontally and vertically to give sides of 35 cm (13.6 inches). Type B design would stretch the electrode horizontally, and Type C would stretch the electrode vertically. The various factors with the three designs are listed in Figure I-3.

Design B was picked based upon the foregoing discussion. It has many favorable attributes. It allows good electrolytic/hydraulic decoupling with presently used flow rates. It also allows the use of existing or pilot machinery for component fabrication, and lowers the development time and costs. Given other design constraints, the other design options might have been selected.

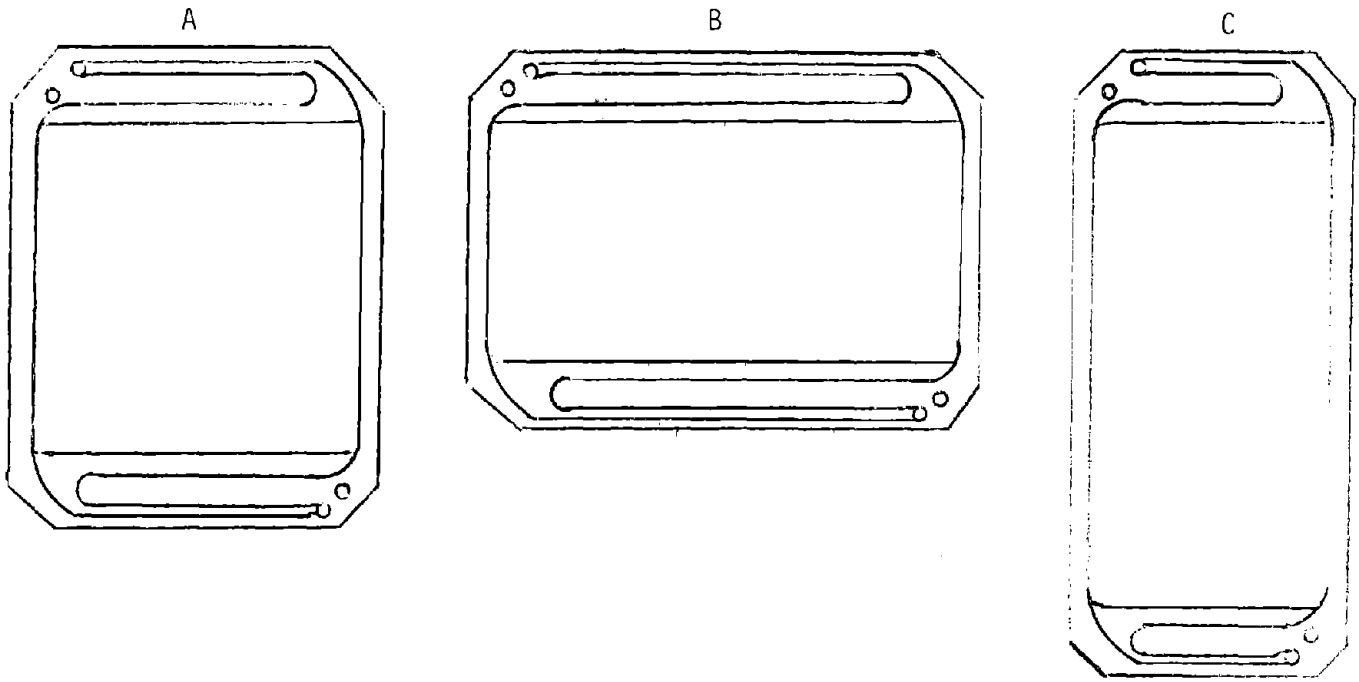

PROFILE STACK	MEDIUM	LOW	HIGH
FLOW DISTRIBUTION TEST REQUIREMENT	NEW TEST	NEW TEST	EXTENSION OF PRESENT
CHANNEL LENGTH/ RESISTANCE	MEDIUM	HIGH	LOW
DECOUPLING HYDRAULIC/ ELECTROLYTIC	BETTER	BEST	GOOD
CO-EXTRUDED ELECTRODES DIE	NEW DIE	EXISTING DIE	NEW DIE
INJECTION MOLDING MACHINE	STANDARD MACHINE	STANDARD MACHINE	LARGE MACHINE
ELECTRODE/FRAME AREA RATIO	BEST	GOOD	BETTER
POSTED DARAMIC SEPARATOR PRODUCTION	COMMERCIAL SIZE RUN NEEDED	PILOT PLANT MACHINE RUN	PILOT PLANT MACHINE RUN
AREA	1200 cm^2	1200 cm^2	1200 cm^2
PROTECTIVE ELECTRODE PER STACK	4	4	4

Figure I-3 Flow Frame Designs

The electrode size selected was approximately 9-1/2 x 19-1/2 inches (24.1 cm x 49.5 cm). The frame edge size is 14-5/8 x 20-1/2 inches (37.2 cm x 52.1 cm). This allows channel lengths of 17-1/4 (43.8 cm) and 16-1/16 inches (40.8 cm) between manifold and tunnel points. The selected channel depth was 0.062 inches (0.16 cm). Widths in the range of 0.06 to 0.13 inches (0.15 to 0.33 cm) are possible. Manifold diameters in the range of 0.5 to 0.7 inches (1.3 to 1.8 cm) can be considered. Deep channels with square or low rectangularity are needed for low pressure drop. However, this requires some thin cross-sections in the mold design and may present difficulties in the injection of plastic past these sections.

A relatively wide, flat section was provided between the electrolyte distribution regions and the channels and the manifold holes to minimize the formation of an electrolyte film which could provide an unintended bypass for current to flow directly from the cell to the manifold. Low tolerances and good sealing will be necessary to control this bypass in the final stack.

The inlet and outlet manifold holes were provided in opposite corners of the spacer flow frame. The tunnels were provided in the two remaining opposite corners. Each of the two protective electrodes in each stack end block provides protective current to two tunnels in this design. Thus, a total of four protective electrodes are required rather than eight needed in previous designs.

I.2.5 Battery Stack Assembly

In battery stack assembly, the co-extruded electrode material would be die cut to shape with holes provided for manifold and tunnels. The electrodes and separator flow frames would be alternately stacked between terminal electrodes and end blocks in the stack assembly. An exploded view of a battery stack, as seen from the top, is shown in Figure I-4.

I.3 Cost Analyses

During Phase I we reported on the production costs at high annual production levels, of a 20-kWh zinc-bromine battery system. These studies were based on an assembly plant approach where factory cost included purchasing of components from vendors and battery system assembly. We have expanded these studies to the case where the battery assembly facility has plastic fabrication equipment (extruders, etc.) and produces components rather than purchasing them. We have also analyzed the manufacturing cost of large bulk energy storage systems (500 MWh of storage capacity/year). In addition, we have applied the Arthur D. Little (ADL) guidelines to arrive at an estimated OEM selling price for the 20-kWh zinc-bromine battery system.[5] Finally, the zinc bromide cost and availability have been considered in terms of present and future market conditions.

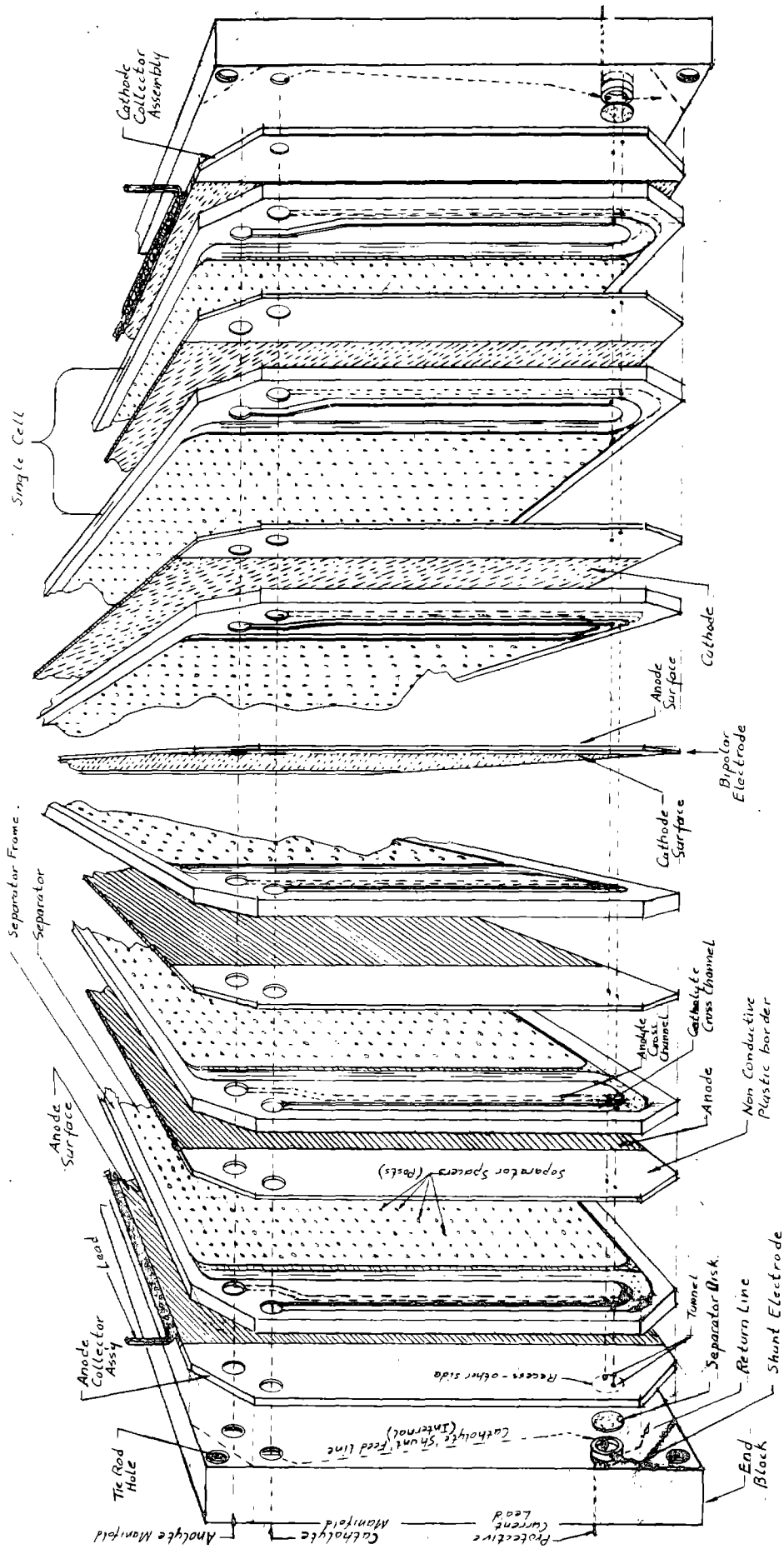

Figure I-4 Exploded View of Battery Stack

I.3.1 Revised 20-kWh System Cost Analysis

During the Phase I work, a company funded effort analyzed the cost of a 20-kWh zinc-bromine battery at several annual production levels. The details of this analysis were given in the Phase I report. Figure I-5 and Table I-1, taken from this report, show a summary of the analysis. This study was based on a system with unsupported electrolyte utilized to 70% of the zinc content. An assembly plant approach was used to arrive at the factory cost. Components were purchased from vendors and assembled in a plant to make the batteries.

In the first quarter of 1981, Reed Process Company (RPC), Millington, New Jersey, was given a company funded contract to analyze the manufacturing costs of 20-kWh zinc-bromine battery systems, using a "make-rather-than-buy" approach. For example, the battery operation would own the extrusion and injection molding machines and produce electrodes, flow frames, etc., rather than purchase these items from vendors. The concentrated zinc bromide solution for the electrolyte would be made at the plant from purchased zinc and hydrobromic acid rather than purchased as a chemical solution. Pump motors, on the other hand, would be purchased from motor manufacturers. The make-rather-than-buy approach requires a larger investment and is more risky than the purchase and assembly approach. The manufacturing costs, however, are lower. RPC arrived at a manufacturing or factory cost of $29.60 and $27.40/kWh for a 20-kWh zinc-bromine battery system at 25,000 and 100,000 units/year production (1981$). This independent cost evaluation compares favorably with the costs discussed in the Phase I report.

I.3.2 Bulk Energy Storage System Cost Analysis

In the second quarter of 1981, the Reed Process Company was given another company funded contract to analyze the manufacturing costs of bulk energy storage zinc-bromine battery systems.

Estimates were made of the costs of our modifications of the battery previously studied (Section I.2.1) to bulk storage use. For this use, the protective covers are omitted and the individual electrolyte reservoirs, pumps, and some of the controls are replaced by larger ones serving all the batteries of a storage unit. The storage units investigated are made up of ten or twenty 20-kWh batteries of the same dimensions as the 20-kWh batteries, or ten or twenty 40-kWh batteries with the same number of cells as the previously studied battery, but twice the electrode area. (2400 cm^2 active area)

The following four steps were used in estimating costs for all cases. Costs for the 20-kWh battery previously estimated by RPC were used as a starting point in these estimates.

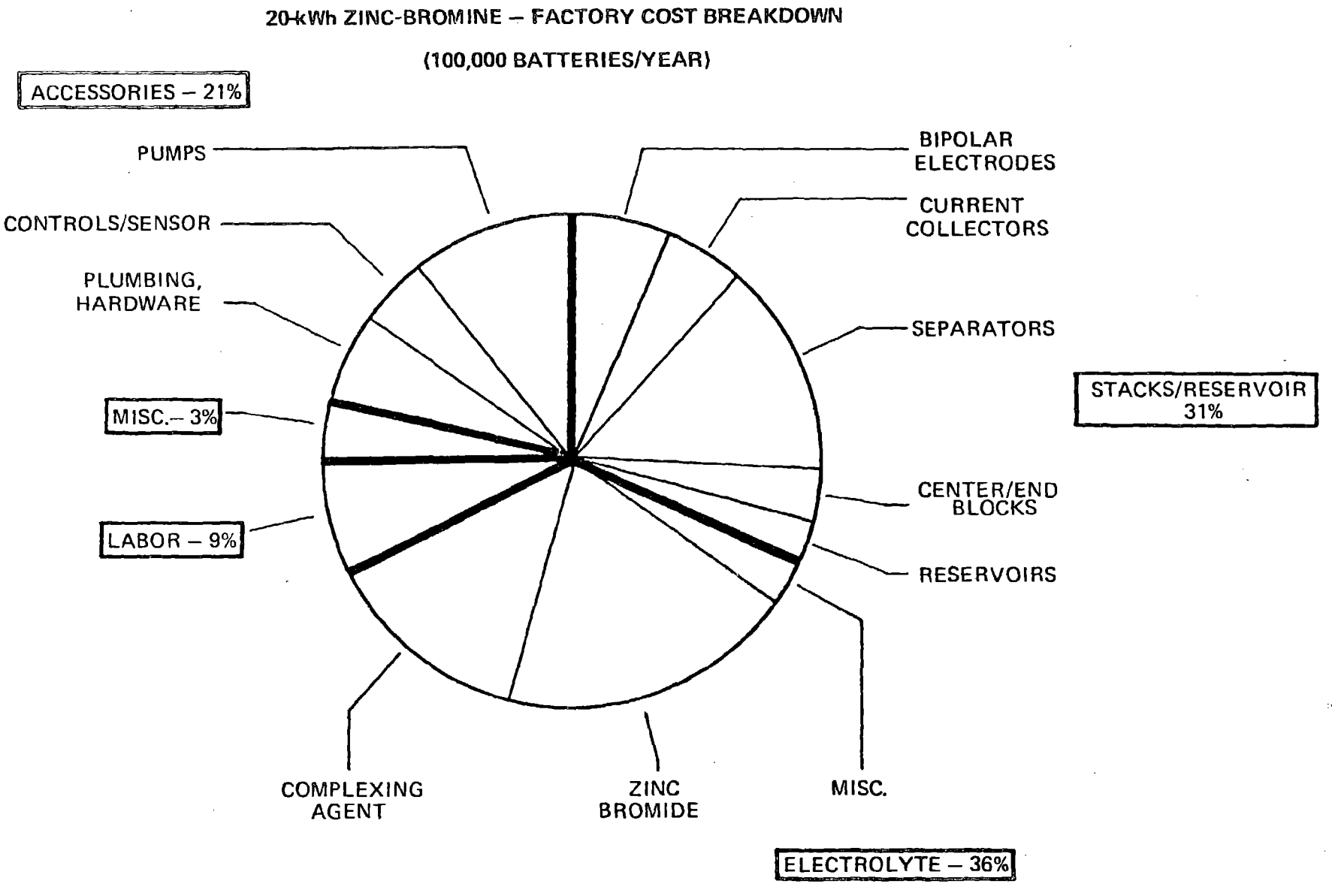

Figure 1-5 Factory Cost Analysis

Table I-1

TOTAL FACTORY COST -
20-kWh ZINC-BROMINE BATTERY

Bipolar Electrodes	38.30
Current Collectors	28.20
Separator Assembly (Inc. outside labor)	77.44
End Support Block Assembly	10.52
Center Support Blocks (Inc. outside labor)	10.36
Reservoir	8.59
Reservoir Tray	2.95
Battery Stacks - Total	176.36
Electrolyte Pump	24.00
Electrolyte Pump Motor	16.00
Isolating Drive System	10.00
Protective Electrode System	10.00
Pump Pressure Sensor	4.00
Electronic Control Board	12.00
Electrolyte Level Sensor	2.00
State-of-Charge Sensor	4.00
Voltage Cut-Out	1.50
Temperature Probes (3)	3.00
Hydrogen Recombination	2.00
Plumbing & Fittings	10.00
Bus Bars - Tie Rods & Hardware	20.00
Batt. Access., Controls, Etc. - Total	118.50
Electrolyte	200.00
Packaging & External Case	18.49
Materials - Total	513.35
In-House Labor	47.75
Factory Cost Total, $/Unit	561.10
Factory Cost Total, $/kWh	28.05

- Delete the cost of the filled polypropylene which is not required for reservoirs and covers of a bulk storage battery.
- Add the cost of common battery support structure, electrolyte tanks, pumps and controls.
- Reduce the estimate of labor, maintenance, and overheads for the components eliminated from the manufacturing plan.
- Estimate the reduction in accessories cost resulting from use of items common to a group of batteries to replace individual pumps, controls, etc. for each battery.

The estimates were based upon production of 500 MWh of storage capacity/year.

Manufacturing costs for the cases estimated are summarized below in Table I-2. Cost of a 20-kWh battery is included for comparison.

Table I-2 Bulk Energy Storage System Cost Comparison

Case	Description	Manufacturing Cost, $/kWh
1A	200-kWh Unit, Ten 20-kWh batteries	28.69
1B	400-kWh Unit, Twenty 20-kWh batteries	27.49
2A	400-kWh Unit, Ten 40-kWh batteries	27.21
2B	800-kWh Unit, Twenty 40-kWh batteries	26.63
0	20-kWh Vehicle battery	29.66

The relatively small differences in cost of these batteries suggests that:

- The cost savings potentially possible with larger electrodes provides little incentive to undertake the technical problems of producing the larger separator frames and electrodes.
- Use of large common electrolyte tanks and fewer but larger accessories probably will not reduce costs substantially. This needs to be looked at again when both vehicle battery accessories and the larger ones for bulk storage batteries are better defined.
- The scale of operations at 500 MWh/year is near the minimum at which continuous manufacture is economical. Cost improvements could result from combination of bulk storage and vehicle battery production.

I.3.3 ADL Costing Method

In 1979, Arthur D. Little, Inc., developed a set of guidelines for estimating the capital costs of advanced battery systems.[5] The intent of these guidelines was to provide a consistent method for pricing of the many advanced battery systems under development at that time. It would provide a basis for cost comparison.

The ADL method was used to price the zinc-bromine battery system. The ADL guidelines were:

1. Annual production rate - 2500 MWh (125,000 20-kWh modules/year)

2. Product yield - 95% on all required quantities of material and components.

3. Labor rate @ 10.00/hr - Includes material handling, shipping, receiving and quality control.

4. Overhead rates @ 150% on direct labor and 10% on purchased materials and components. This covers fringe benefits, supervision and general administrative expenses.

5. Rent - (plant) @ $5.00/square foot.

6. Equipment cost and depreciation - 25% mark-up added to cover installation. Total amortized linearly over 10 year period.

7. Working capital @ 30% - Value of annual production costs plus rent and depreciation.

8. $5.00 per kWh added to factory cost. $2.00/kWh of this to represent cost of marketing including related engineering effort. $2.00/kWh represents cost of returns, replacements and field service over the life of the warranty. $1.00/kWh represents remaining miscellaneous costs.

9. After-tax return on investment - Constant annual amount equal to 15% of the initial invested capital (equipment investment plus working capital).

10. Taxes - The consolidated total of federal, state and local taxes paid is to equal the after-tax return on investment.

Battery capital costs then include factory cost (items 2, 3, 4, 5 and 6) and investment costs (items 8, 9 and 10), calculated as follows:[5]

"The battery capital cost is computed by first deriving a factory cost for one year's production according to the above procedure and then calculating the total investment by summing the working capital requirement (30% of factory cost) and marked-up equipment costs. Return on investment and taxes, together equivalent to 30% per annum of the invested capital, are then added to the factory cost. Finally, $5/kWh are added for marketing, warranty, and miscellaneous costs. The capital cost (selling price) per battery can be obtained by dividing the total by the number of batteries produced annually."

These guidelines may not be applicable to a low cost battery like the zinc-bromine system because, for example, the final $5/kWh is arbitrary. However, using these guidelines and the system components and fabrication techniques, the summary of the factory and capital costs developed are given in Table I-3. The ADL method uses a salvage value to arrive at a net capital cost shown in Table I-4. In ADL terminology, capital cost is equivalent to selling price. The ADL method produces a low, but comparable price for zinc-bromine battery systems. The details of the analyses are given in Appendix I.

ADL guidelines give a capital cost of $40.06/kWh. The salvage value of electrolytes and copper was estimated at $5.76/kWh. This leaves a net capital cost of $34.30/kWh ($1981) based on the ADL guidelines.

Table I-3

Factory and Capital Costs

Material (Includes electrolyte @ $220/Module)	$321.36
Purchased Components (Includes outside molding costs and accessories)	211.71
In-House Labor Costs	68.74
Production Cost/20 kWh Module	601.31
Production Cost/kWh	30.09
1. At 2500 MWh Production Cost Per Year	$75,225,000.00
2. Marked-up Equipment Costs (10% of Est. @ $12,500,000)	1,250,000.00
3. Rent (100,000 sq. ft. Plant @ $5.00/ft^2)	500,000.00
4. Total Factory Cost (Lines 1+2+3)	76,975,000.00
5. Working Capital Requirement (30% of line 1)	23,092,500.00
6. Total Investment ($12,500,000 + line 5)	35,592,500.00
7. Return on Investment & Taxes (30% of line 6)	10,677,750.00
8. Additional @ $5.00/kWh	12,500,000.00
9. Total Capital Cost (lines 4,7 + 8)	100,152,750.00
Capital Cost per 20-kWh Module	801.22
Capital Cost per kWh	40.06

Table I-4

Salvage Value and Net Costs

Electrolyte Salvage Value	
225 lbs $ZnBr_2$ @ .30/lb.	67.50
50 lbs Quaternary @ .70/lb.	35.00
$16.31 Silver @ 50% Recovery ($12.00 troy oz) Value (Includes disassembly Costs)	8.15
Copper - est. $9.00 @ 50% Value	4.50
Total per 20 kWh	115.15
Salvage Value/kWh	5.76
From Previous Page	
Capital Cost per kWh	40.06
Less Salvage Value	- 5.76
Net Capital Cost/kWh	$34.30

I.3.4 Zinc Bromide Costs/Availability

The cost and availability of zinc bromide should not present any problems in the development of a zinc-bromine battery system. The precursors of zinc bromide are elemental zinc and bromine.

The demand for zinc metal is down because of the substitution of plastic for zinc in automobile components and in galvanized pipe. The demand for bromine is down because of the reduced use of the tetraethyl lead in gasoline. (Bromine is used in some TEL synthesis processes). Thus, the price of zinc and bromine have been and are projected to be relatively constant. Considering inflation, the costs have decreased. For example, trade list and market prices and supply/demand for bulk elemental bromine in cents per pound are shown in Table I-5.

Table I-5 Bromine Cost History

YEAR	1960	1970	1977	1978	1979	1980	1981	1982	1985
Trade List	21.5	18.8	25-30	25-30	25-30	25-30			
Market	20	17.5	20.7	19.4	20.4	19-20			
SUPPLY & DEMAND	.....Millions of Pounds....Estimated...Domestic U.S...								
Capacity	200	423	627	657	657	657			
Production	175	350	434	447	502	375			
Demand	164	342	364	353	409	281	280	290	315
Exports	11	8	60	94	93	94			

The U.S. reserves for bromine-rich brines are essentially unlimited. Even if these supplies were exhausted, we could return to extracting bromine from sea water.

Recent zinc pricing history is essentially similar. Zinc bromide solutions are used in oil well completion fluids. Present use is in excess of 100,000,000 pounds of solution per year and is projected to approach the billion pound level in the mid-late 1980's.

Great Lakes Chemical Corporation, West Lafayette, Indiana, has quoted the following prices (1980 dollars) for zinc bromide solution (100% basis):

	Pounds/Year	
	25 Million	100 Million
$ZnBr_2$ (100%)	54.3 cents/lb	51.9 cents/lb

I.4 Computer Simulation

This effort developed a computer simulation of system performance based on single-cell performance parameters, multi-cell interactions, and auxiliary power requirements. In view of the complex interaction of the many variables to be assessed, an overall computer simulation program was required. This program will aid optimization of system design for specific application objectives, in terms of interpreting parametric testing, assessing the effect of possible design modifications on system performance and providing a mathematical structure against which the continuing development efforts can be compared. This computer model can be updated to integrate new data and new design thinking as they become available.

The computer program is built around a simplified model of single cell electrochemical performance. This model assumes a constant open circuit cell voltage (1.75V). Resistive polarizations are considered, with separate contributions from the electrolyte, the separator and the bipolar electrode. Battery polarization data[3] suggests that electrode overvoltage polarization approaches zero. Coulombic inefficiency in the single cell is related to self discharge, i.e., the diffusion of bromine across the battery separator. Diffusional resistance is attributed to the thickness and tortuosity of the separator as well as diffusional boundary layers at the surface of the zinc electrode and the separator. The diffusivity (2×10^{-5} cm^2/sec) of Br_2 in the electrolyte was measured prior to Phase I. The solubility of bromine in the aqueous catholyte, the driving force for diffusion, was assumed constant. Future improvements of this model will allow the bromine in the aqueous catholyte to vary (Sections IV.3 and IV.6). The second phase (bromine complex) is not known to directly affect self-discharge except for its ability to reduce the bromine concentration in the aqueous catholyte.

Multicell interactions in a single stack assume that of current passes uniformly from cell-to-cell and that the stack voltage is a direct addition of single cell voltage.

Auxiliary power requirements include the pumping power required to circulate the electrolytes and the power consumed by the tunnel shunt current protection. A full discussion of these auxiliaries appears in the Phase I Final Report. The pumping power is primarily a function of flow rate, the manifold diameter and the geometry of an individual cell flow frame. The tunnel protection is primarily a function of electrolyte conductivity, the number of cells in series and the geometry of individual cell flow frames.

Appendix II includes a complete description of the equations used in the simulation, with plots assuming typical dimensions and physical constants of the model. This program will be used during Phase III to model the results of the parametric testing program and to guide efforts in the design of the core technology to meet the requirements of specific battery technologies.

SECTION II

Component Development

The purpose of this task was to develop the required components for battery module assembly and battery system developments. The Phase II program focused on two areas: 1) development of the two-piece cell design concept, and 2) design of a microprocessor-based controller.

II.1 Two-Piece Unit Cell

The electrochemical cell used in the 20-kWh battery is made up of six individual components - an insert injection-molded bipolar electrode, a Daramic separator, two polypropylene screens to maintain half cell spacings, and two plastic spacers to match the side-wall spacing to the polypropylene screens. One of the major simplifications of the zinc-bromine battery under this contract was to reduce this part count to two components per cell. One component is the conductive carbon-plastic electrode which is framed on two sides with a non-conductive polyolefin material as shown in Figure II-1. The second component is the Daramic separator with the flow frame injection molded about it as shown in Figure II-2. These two components form the unit cell as shown in Figure II-3.

II.1.1 Co-extruded Electrodes

During this contract, one of the significant manufacturing simplifications was the successful development of extruded carbon-plastic electrodes which had a non-conductive plastic frame extruded simultaneously along both edges. The extrusion die used for this work was fabricated prior to the start of this contract. The die, Figure II-4, originally utilized two extruders. One extruder fed the carbon-plastic material to the central position of the die. The other metered the non-conductive framing plastic to the die where it was split into two paths for extrusion on either side of the conductive plastic. The initial testing of the die was conducted primarily to check material flow and shrinkage characteristics, i.e., the ability of the die to heat the plastic properly and to maintain proper dimensions. These tests were successful in selecting a non-conductive plastic to properly match with our conductive material.

The second co-extrusion run was conducted at an outside vendor's facility where all of the necessary take-off rolls were available to not only extrude the plastics, but to control the dimensions and properly cool the thermoplastics. This run produced over 500 linear meters of electrode material. This material, after application of the cathode catalytic layer, was successfully tested in small battery modules discussed in Section IV. There were, however, two areas which needed improvement. First, some sections of this extrusion run had material which contained very small pinholes. These were most likely the result of a poor carbon dispersion during compounding. The second problem was an insufficient amount of material at the joining line between conductive and non-conductive plastics. The inability to separately control the non-conductive material flowing to either side of the extrusion die also presented a control

Figure II-1 Co-Extruded Carbon-Plastic Electrode

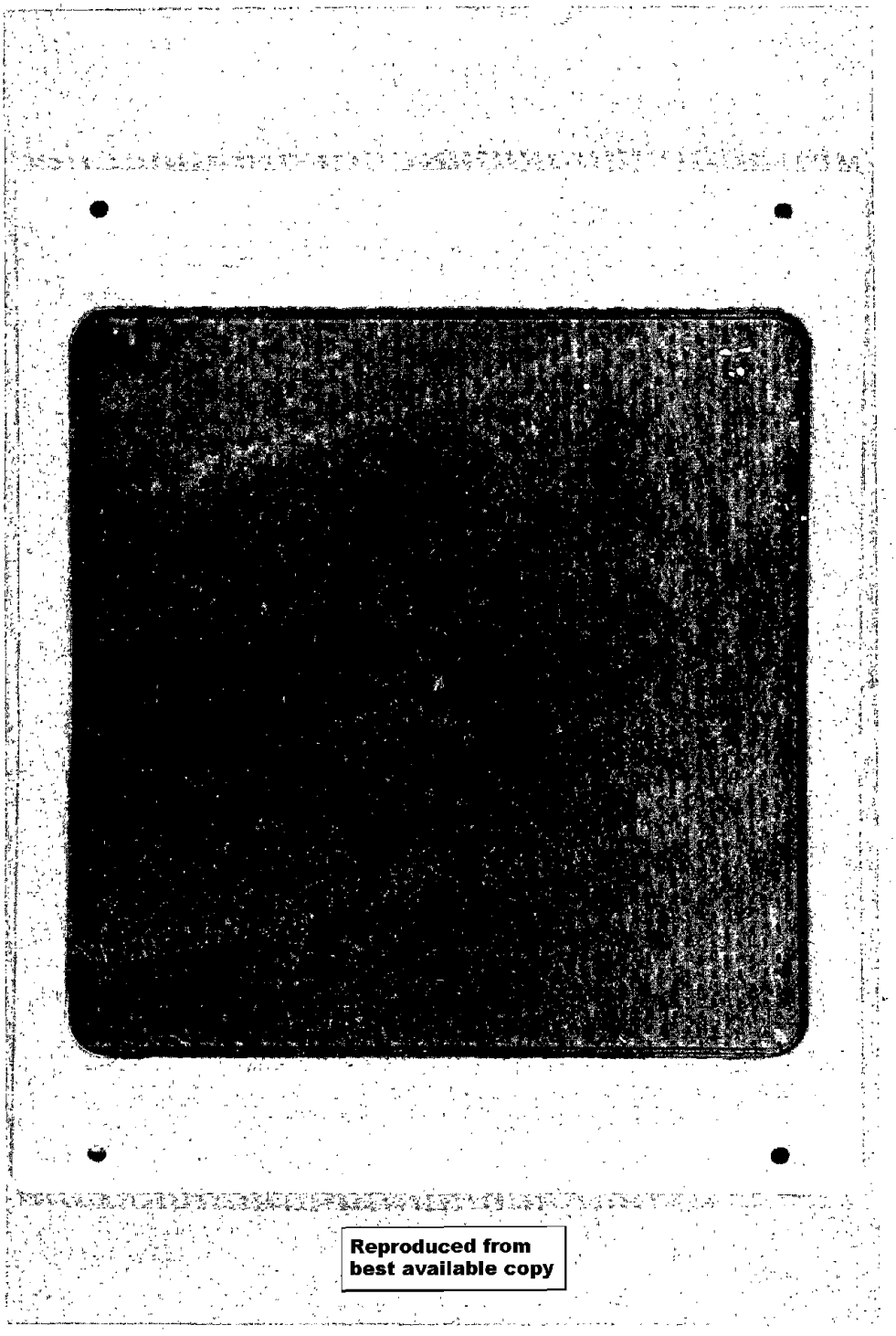

Figure II-2 Separator with Injection-Molded Flow Frame

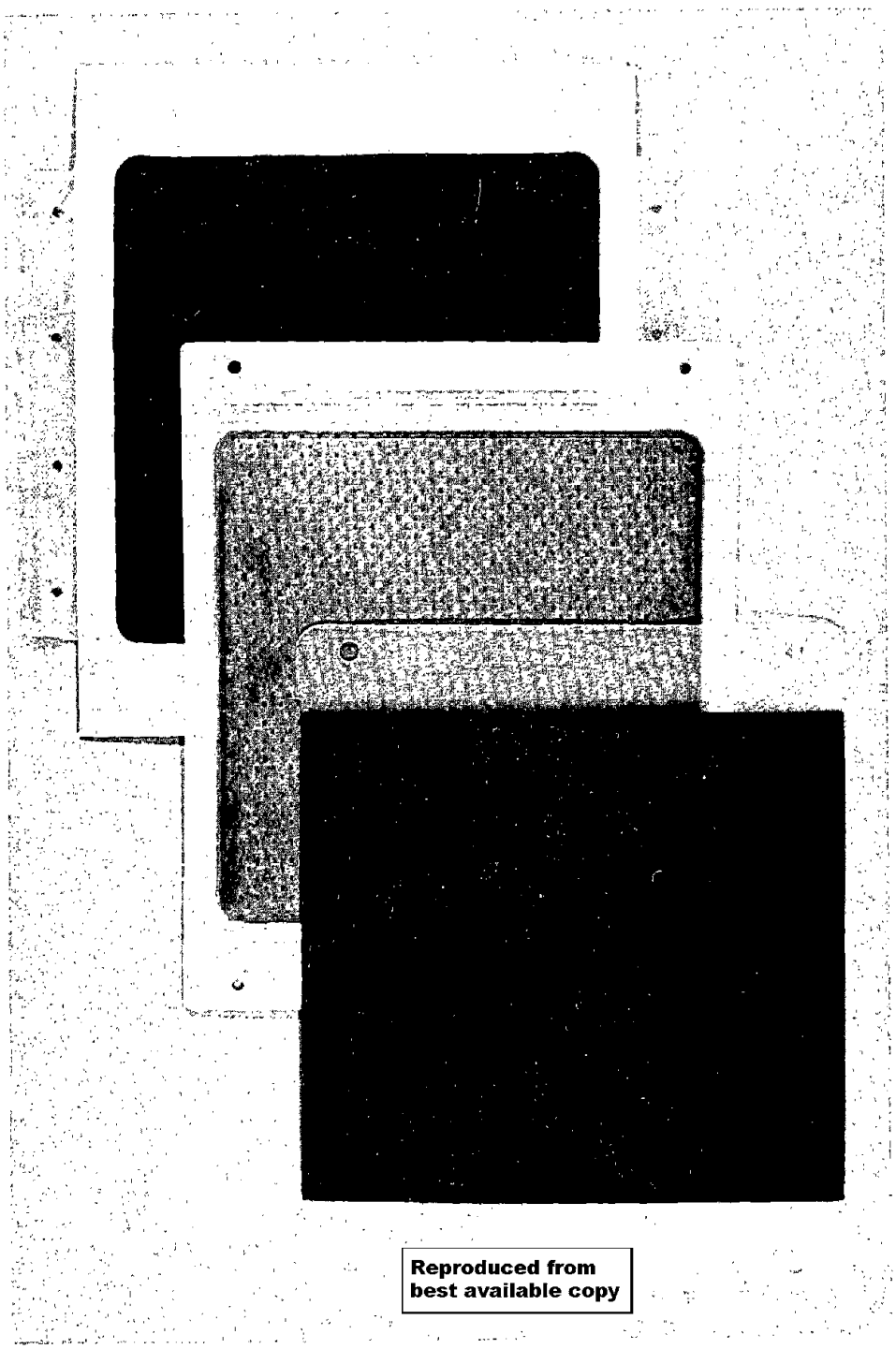

Figure II-3. Two-Piece Unit Cell

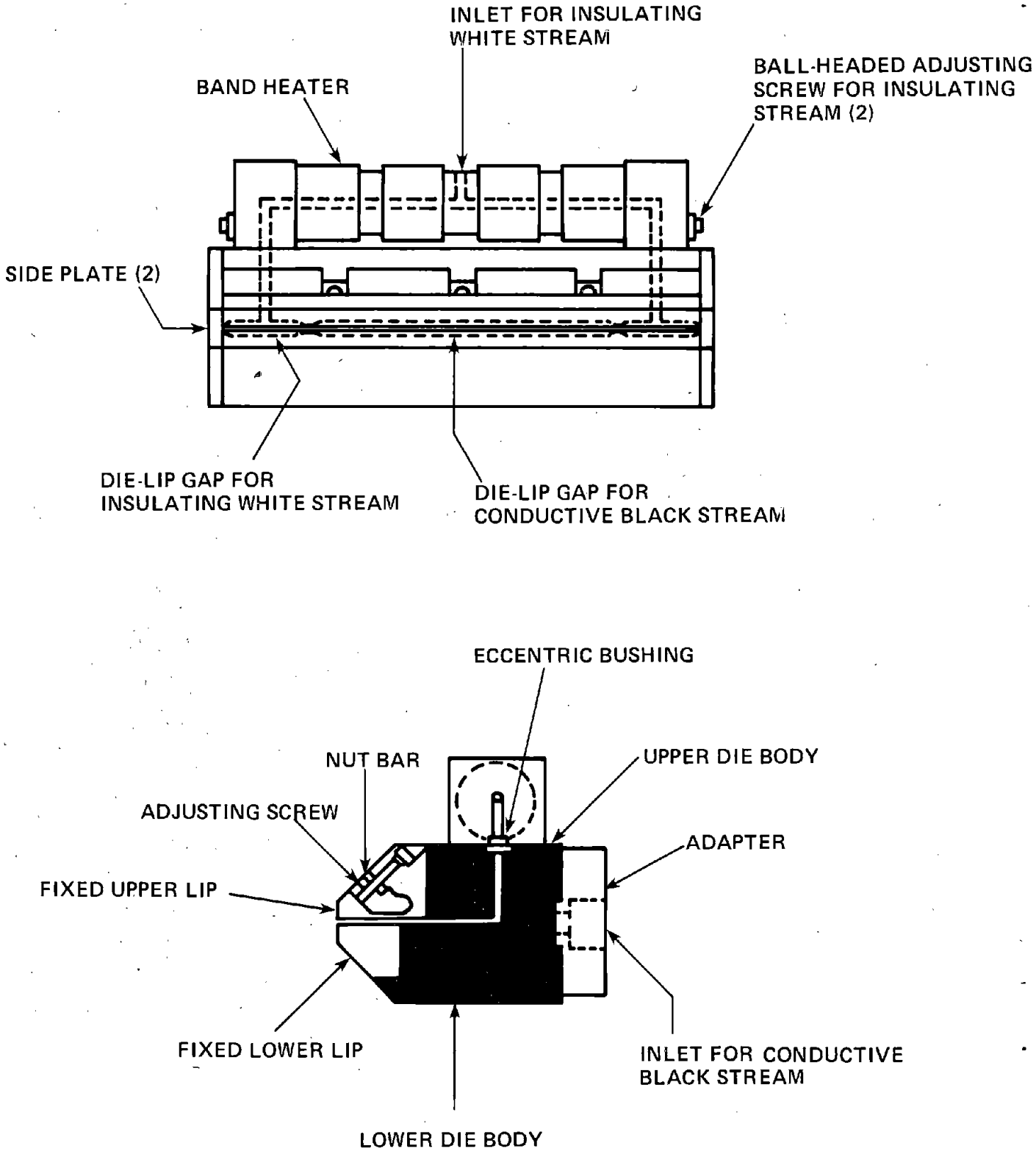

Figure II-4 Co-Extrusion Die

problem. These difficulties resulted in a thin "black-white" bond and some thickness variations from side-to-side as illustrated in Figure II-5.

Prior to the third extrusion run, two modifications were made to the die. The first involved a minor change in the exact distance from the die lips where the two plastics first come into contact. The second involved changing the die to permit the utilization of three extruders - one to feed each segment of the extrudate. These two modifications were designed to remove the thin section where the non-conductive and conductive plastics were joined and to allow sufficient control over feed rates so that the proper volume of material was delivered to each part of the die at all times. The success of these modifications was apparent during the third extrusion run where several hundred linear meters of co-extruded electrodes were extruded. This material is now being tested in several batteries without, as yet, any difficulties.

II.1.2 Insert Injection-Molded Separator

In the two-piece unit cell design, the separator is an insert around which the flow frame is overmolded. The separator material of choice is Daramic, a microporous filled polyolefin manufactured by W.R. Grace Co. By using chill rolls designed and supplied by Exxon, 0.6 mm high posts can be continuously patterned onto the Daramic surface as it is being extruded. These posts take the place of the two polypropylene support screens within the six-piece unit cell.

The flow frame, which is injection molded around the Daramic separator, has built into it the means for a uniform flow distribution of both anolyte and catholyte across the electrode surface. Also, the frame thickness is sized to just match the 0.6 mm height of the posts, thereby alleviating the need for separate spacers as was previously the case with the Vexar polypropylene screens pictured in Figure 0-2.

The first and only attempt thus far to mold the Daramic as an insert was extremely successful. Over 400 parts were fabricated at a very low reject rate. These parts were very forgiving of small alignment errors in locating the insert within the mold. Also, in molding this component, it was found that a very strong plastic bond was formed between the Daramic and the frame material due to the high latent heat content in the injected plastic. This is unlike the tongue-in-groove bond formed when carbon-plastic electrodes are used as inserts. It is anticipated that the strengthening of this bond will result in fewer rejected battery stacks. Also, since the Daramic no longer goes to the edge of the stack, it will not be necessary to worry about "weepage" of electrolyte from the battery through the Daramic's microporous pores. All batteries using co-extruded electrodes have also been tested with these separators.

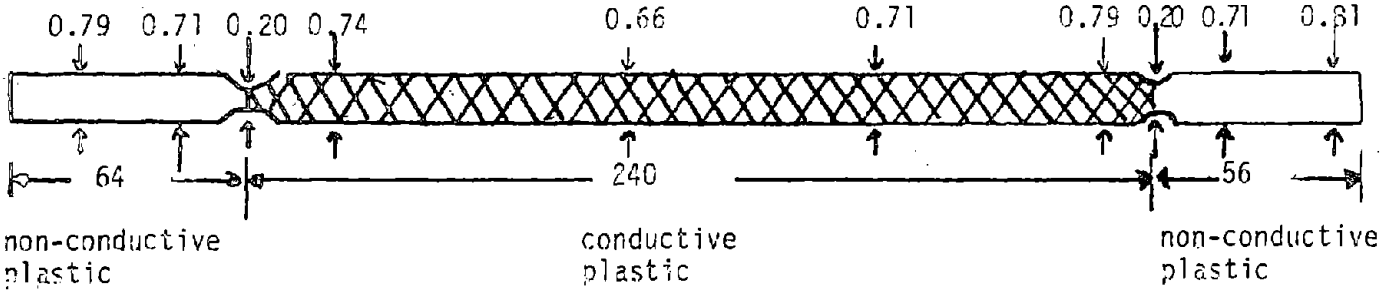

*units in millimeters

Figure II-5 Cross-Section View of Second Co-Extrusion Run

II.2 Microprocessor Controller Development

Design and specifications of a controller is a key item in zinc-bromine battery system development. The function of the controller is to automate certain aspects of battery operation by regulating battery auxiliaries, such as pumps and valves, according to demands placed on the battery or in response to external commands. The controller is also mandatory in maintaining safe battery operation. The purpose of this Task has been to develop the necessary system logic and operating state diagrams so that system specifications can be formalized and used to design a bread board zinc-bromine battery system controller.

II.2.1 Controller Functions

The schematic shown in Figure II-6 depicts a zinc-bromine battery system with its necessary auxiliaries and sensors. The devices to be controlled are: (1) the electrolyte pumps; (2) the four-way valve which controls the direction of catholyte flow (up or down); (3) the "oil" carburetor valve which controls the amount of complexed bromine fed to the battery stack; and (4) the valve which controls cooling water flow to a heat exchanger in the anolyte tank. Also shown in Figure II-6 are three relays which determine connection of the battery stack to a shorting resistor or an external circuit which can be either a charger or a load.

Included in Figure II-6 are a number of sensors. Wherever possible, low cost switches have been utilized to minimize the need for A/D conversion. Four pressure switches are used to sense high and low pressure situations in anolyte and catholyte. Similarly, two temperature switches are contemplated, one set for a temperature (~40°C) at which the cooling water valve would open and the other set at a higher temperature point (~50°C) for system safety shut-down purposes. Included in the catholyte tank is a state-of-charge (SOC) sensor which is a proprietary development and provides an analog signal proportional to battery SOC. Battery voltage and current are also sensed with three battery voltage levels being used for control purposes as will be discussed later. Current measurements are not used for control purposes, but only for data acquisition or display.

The system just described does not require a microprocessor based controller with a large calculating or arithmetic capability. A/D conversion is limited to battery voltage and SOC analog signals. A limited amount of input/output capability is required in the microprocessor with the system shown in Figure II-6 since essentially only 8 output ports and 11 input ports would be necessary. This is well within the capabilities of a state-of-the-art single chip microcomputer such as, for example, the Intel 8051.

In order to develop the necessary control system hardware and software, two items are required: (1) a system logic table which indicates the status of each control element during each anticipated state of the system, and (2) a system state diagram which indicates what transitions are allowed between the states of the system and how the transition from state-to-state is initiated. For the zinc-bromine battery system, we anticipate seven system states: (1) SHUT-DOWN; (2) START-UP; (3) STAND-BY; (4) CHARGE; (5) DISCHARGE; (6) CLEAN-OUT; and (7) STRIP.

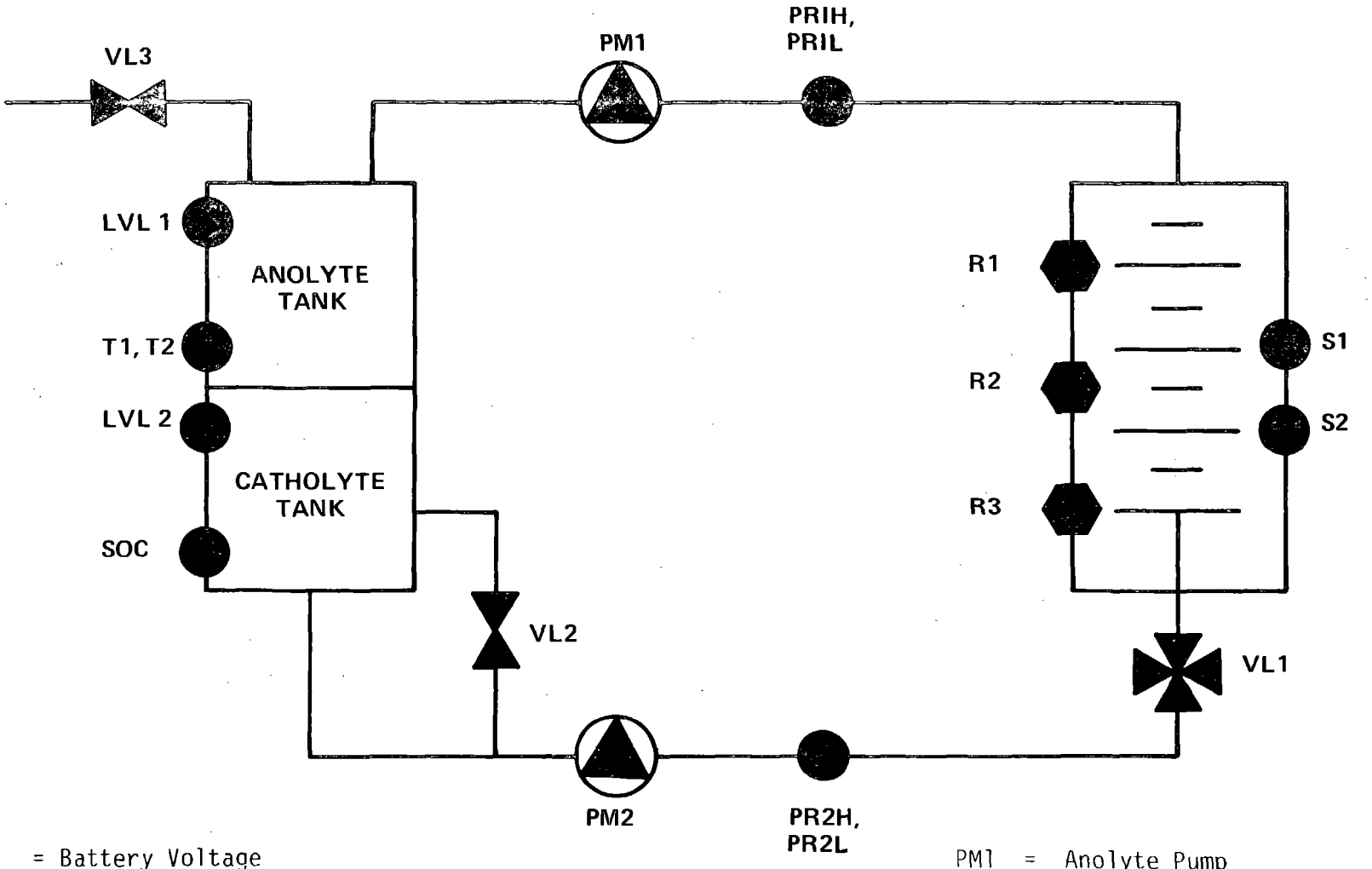

S1

SI	= Battery Voltage	
S2	= Battery Current	
1H,PR1L	= Anolyte Hi/Lo Pressure Switches	
2H,PR2L	= Catholyte Hi/Lo Pressure Switches	
LVL 1	= Anolyte Level Switch	
T1, T2	= Electrolyte Temperature Switches	
LVL 2	= Catholyte Level Switch	
SOC	= State of Charge Sensor	
PM1	= Anolyte Pump	
PM2	= Catholyte Pump	
VL1	= 4-Way Reversing Valve	
VL2	= Oil Carburetor Valve	
VL3	= Cooling Water Valve	
R1	= Shorting Relay	
R2	= Open Circuit Relay	
R3	= Charge/Discharge Relay	

Figure II-6 Schematic of Zinc-Bromine Battery System with Auxiliaries and Sensors

II.2.2 System Logic

The system logic is described in Table II-1. During SHUTDOWN, all control elements with the exception of the cell shorting relay are in an "off" state. The battery is in the START-UP state, the pumps are turned on at a "high" pump speed (to remove any entrapped gas in the battery stack), the shorting relay is opened, the catholyte flow direction valve is in its "up" position, and the oil carburetor valve is "open". After a predetermined period, the system goes to a STAND-BY mode, with the pumps operating at their "normal" speed, catholyte flowing in the "down" direction, and the oil carburetor valve is closed. The main distinction between the CHARGE and the DISCHARGE state is the status of the oil carburetor valve - "closed" during charge and "open" during discharge. States 6 and 7, CLEAN-OUT and STRIP, refer to two modes of operation prior to battery SHUT-DOWN. In the CLEAN-OUT mode, which is used prior to battery SHUT-DOWN with the battery in the "charged" state, the battery stack is shorted out with the pumps running and the oil carburetor valve "closed". During this state, any residual bromine complex is removed from the battery stack to minimize self-discharge during SHUT-DOWN. On the STRIP state, the battery is again shorted out with the pumps on but with the oil carburetor valve "open". The purpose of this state is to periodically remove all zinc from the battery stack. The cooling water valve may be "open" or "closed" in any state, depending on the electrolyte temperature.

The state diagram for the controller is shown in Figure II-7. The arrows indicate allowed transitions between system states, with the STAND-BY state being central to most transitions from state-to-state. As indicated, a transition directly from SHUT-DOWN to STAND-BY would not be allowed. The state diagram recognizes three methods for initiating a transition from one state to another: (1) a timed transition; (2) a sensor determined transition; and (3) a transition based on an external command signal. For example, the transition from the START-UP state to the STAND-BY state is initiated after a predetermined time period in the START-UP mode. Transition from the CHARGE state to the STAND-BY state can occur via a sensor, e.g. state-of-charge or stack voltage level, or on command.

II.2.3 Functional Specification

Based on these control requirements, we have developed a functional specification for a zinc-bromine battery controller. Key to these functional specifications are the following operational requirements:

(1) Allow the user to enter commands for the selection of a particular state

(2) Determine and execute valid command sequences

(3) Monitor the battery system status via its sensors

(4) Provide visible indication of system status and sensor outputs

(5) Take the necessary steps on sensor activation

Table II-1

Zinc-Bromine Battery Controller System Logic

	Device / Phase	High Pump Speed	Normal Pump Speed	Shorting Relay	Open Circuit Relay	Discharge Relay	Catholyte 4-Way Valve Flow	Oil Valve	Cooling Valve
1	SHUT-DOWN	OFF	OFF	ON	OFF	OFF	DOWN	CLOSED	CLOSED
2	START-UP	ON	OFF	OFF	ON	OFF	UP	OPEN	CLOSED
3	STAND-BY	OFF	ON	OFF	ON	OFF	DOWN	CLOSED	CLOSED
4	CHARGE	OFF	ON	OFF	OFF	OFF	DOWN	CLOSED	OPEN
5	DISCHARGE	OFF	ON	OFF	OFF	ON	DOWN	OPEN	OPEN
6	CLEAN-OUT	OFF	ON	ON	OFF	OFF	DOWN	CLOSED	CLOSED
7	STRIP	OFF	ON	ON	OFF	OFF	DOWN	OPEN	CLOSED

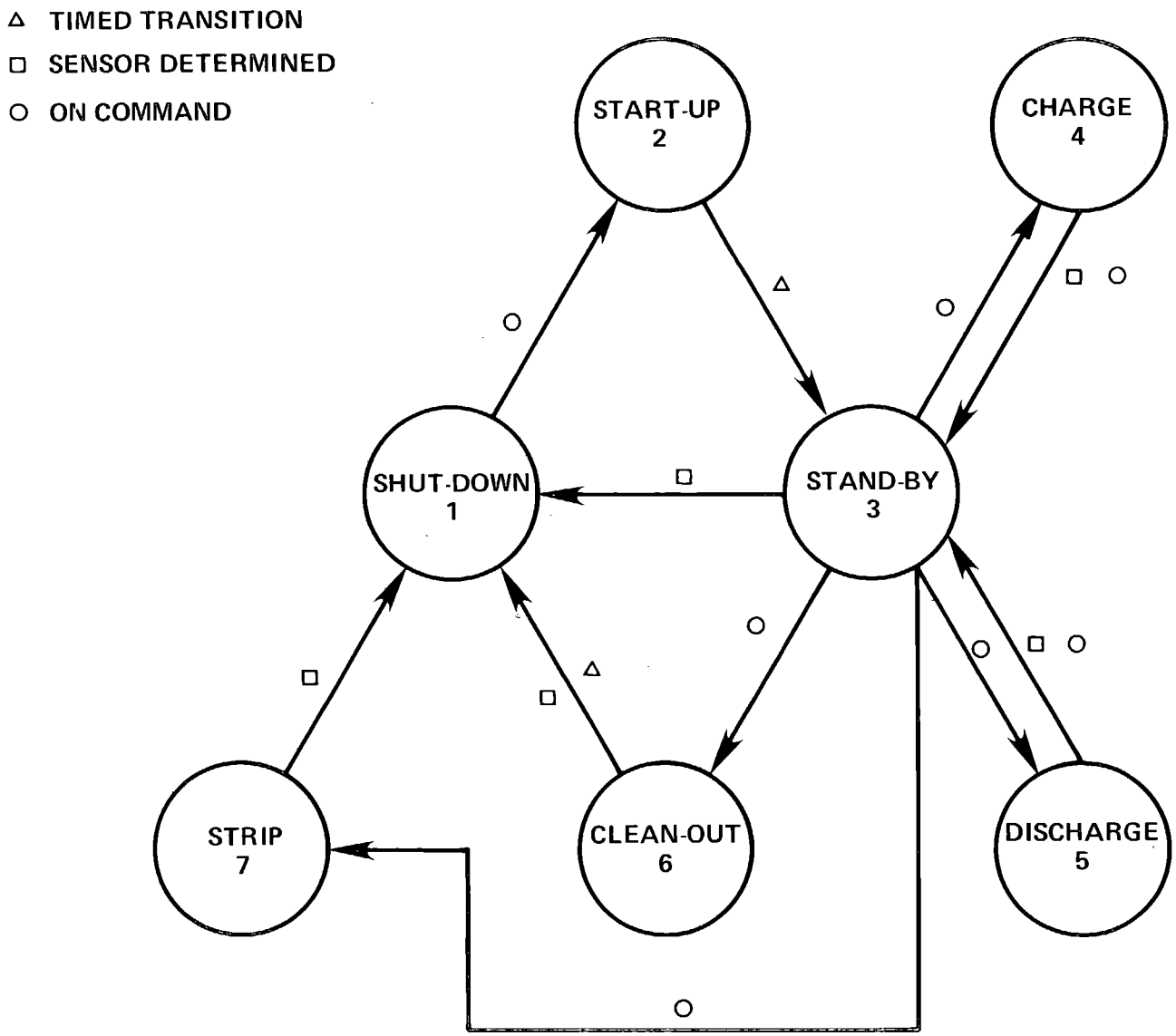

Figure II-7 Zinc-Bromine Microprocessor Controller State Diagram

(6) Allow the user to simulate the activation of any sensor within any state of the system

(7) Allow the user to activate or deactivate any control element

(8) Monitor and display the state of control elements

(9) Allow the user to enter commands locally and remotely

The block diagram of the prototype microcomputer-based controller is shown in Figure II-8. The microcomputer chosen for this prototype is the Intel iSBC 80/20-4 Single Board Computer. The central processor of this microcomputer is the widely used Intel 8080A CPU. The major reasons for the choice of iSBC 120-4 are: (1) the significant input/output (I/O) capability of 48 programmable parallel I/O lines; (2) the eight level programmable interrupt controls: and (3) the two programmable 16-bit BCD and binary timers. While a single component 8-bit microcomputer such as the Intel 8043 or 8051 (commonly used in automotive applications) are projected for use in future systems, the operational requirements for this prototype zinc-bromine battery listed above make the versatile single board computer the appropriate choice.

The proposed layout of the front panel of the controller is shown in Figure II-9. A set of command keys is provided to enable the user to initiate state-to-state transitions. The particular command key will be illuminated when engaged. Readout of battery voltage and current is provided via digital panel displays. Battery state-of-charge is indicated in percentage on a ten position bar graph display. A SHUT-DOWN indicator and a local/remote switch is located between the command keys and digital panel meters. In the remote mode, the controller will accept commands from an external device via an RS 232 serial interface.

A combination battery status indicator and simulator is given in a labeled keypad form on the left of the front panel. Each key is LED annunciated (except RESET) to show the state of the associated sensor or control. When an LED is on, the condition of that system component is indicated by the label above the key. The keys can simulate system state or manually activate sensors. The LED to the immediate right of the keypad will be illuminated when the keypad is in the simulation mode. The "reset" key will cancel any request made of control elements via the keypad.

A set of infrequently used controls will reside on the rear of the controller as shown in Figure II-10. The three keypad is an extension of the main keypad and can be used to control the three stack control relays. The six DIP switches provide the means by which the appropriate timing intervals and voltage sensor levels can be varied.

This prototype controller is presently under construction. It will be tested with a 20-cell battery stack (a nominal 1-kWh battery system) early in the next phase (III) of this contract.

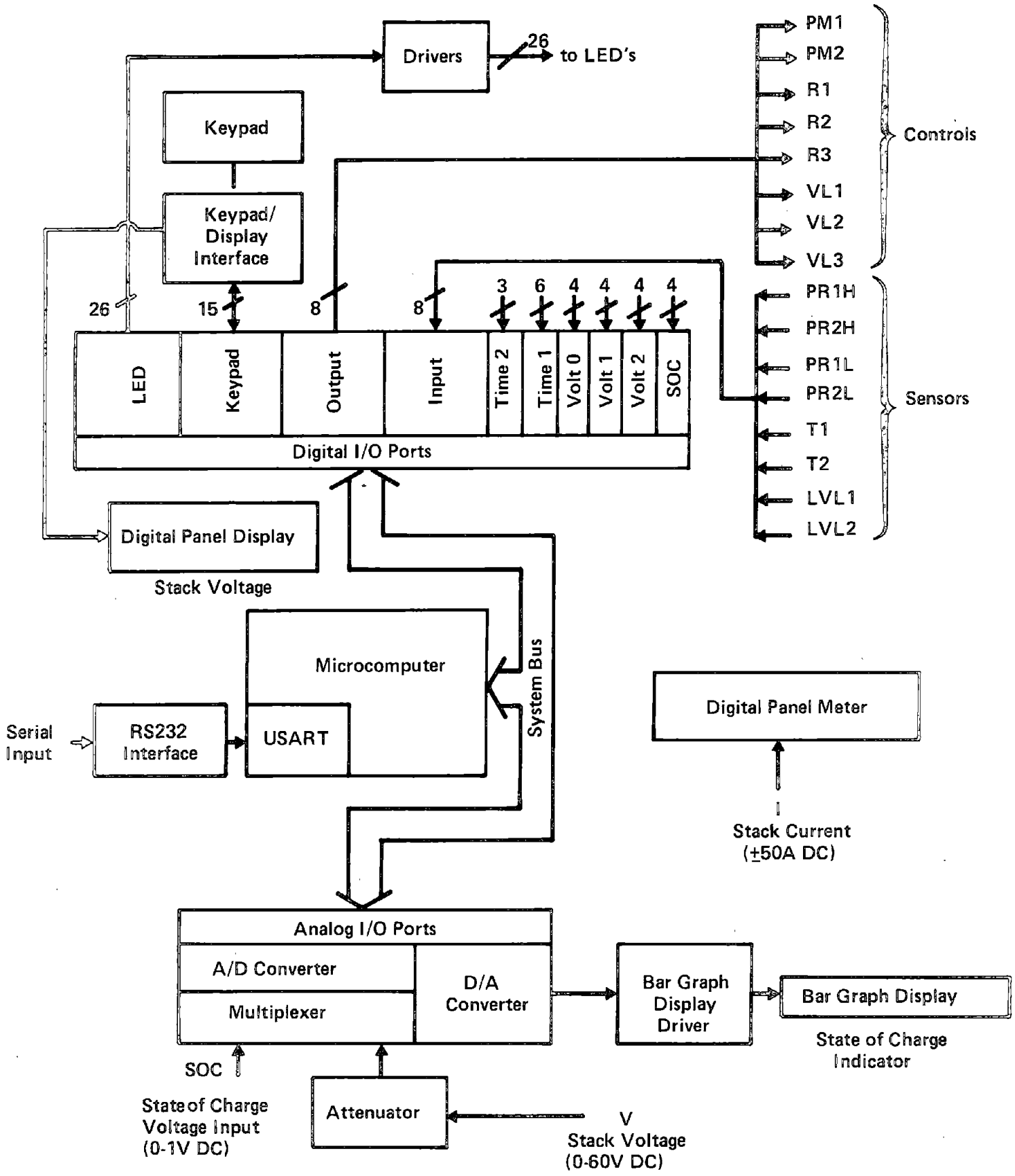

Figure II-8 Block Diagram of Zinc-Bromine Battery Controller

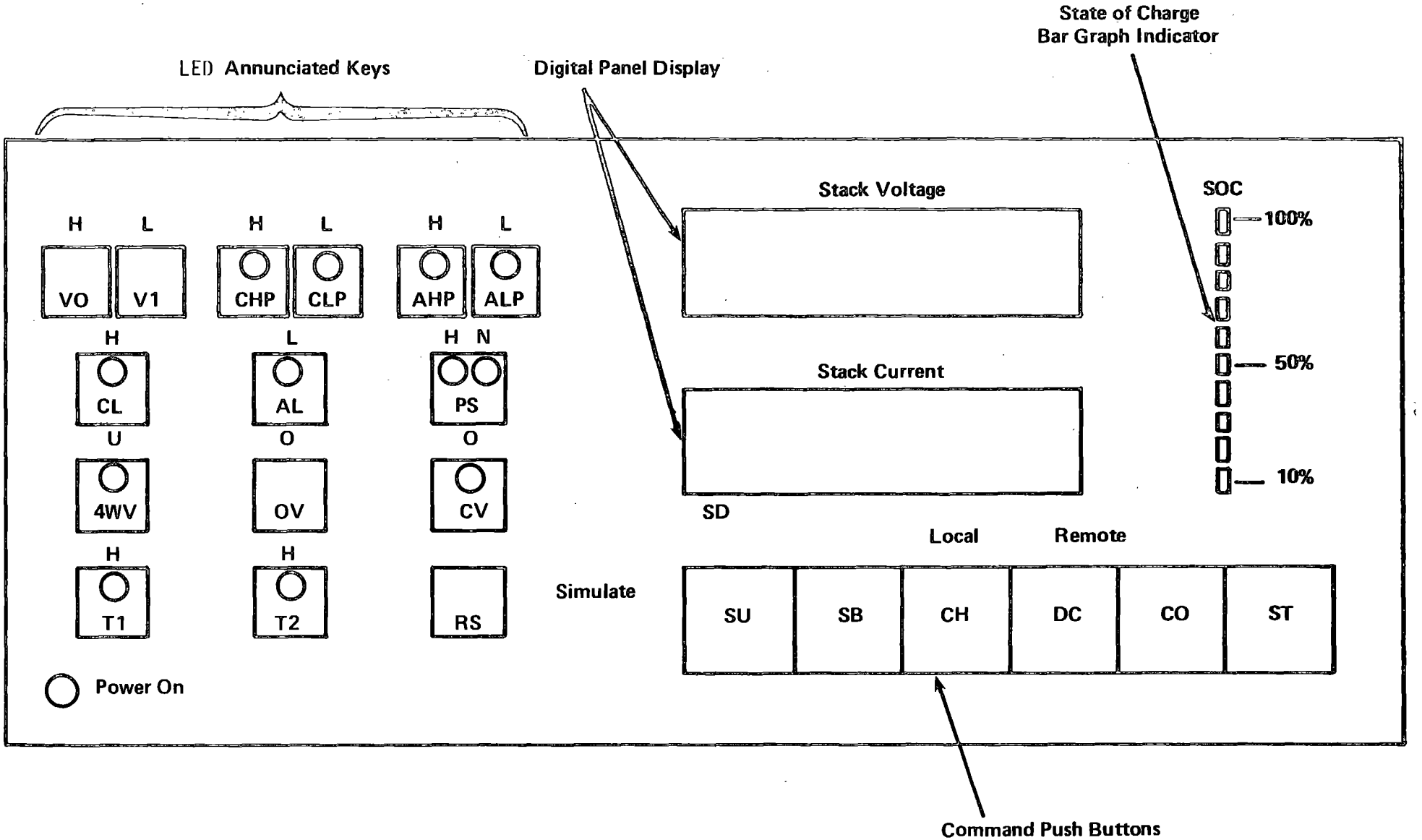

Figure II-9 Zinc-Bromine Battery Controller Front Panel

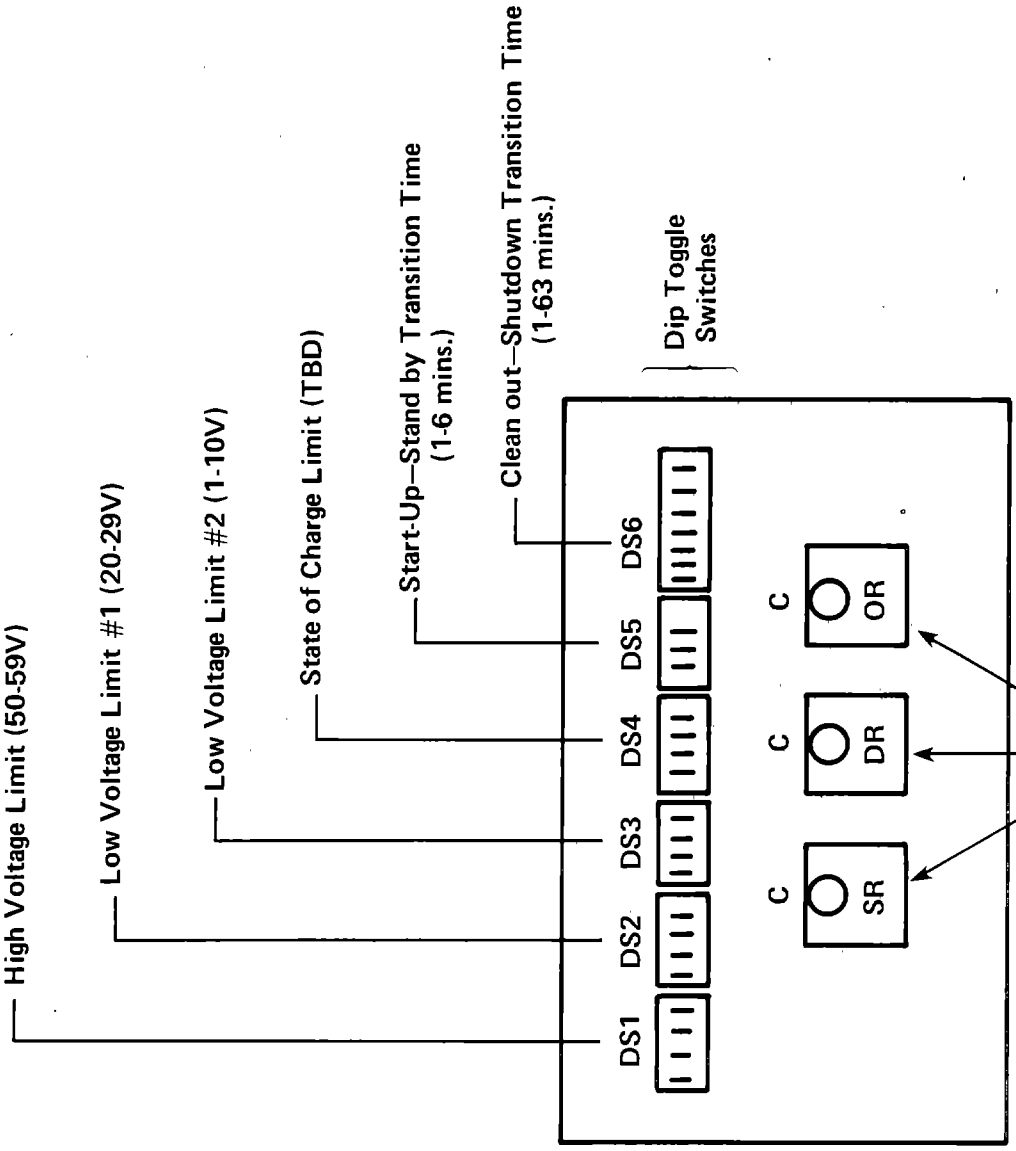

Figure II-10 Zinc-Bromine Battery Controller Rear Panel

SECTION III

III Large Battery System Testing

This section describes the design, construction and testing of the X-20 battery which was the major focus of the Phase II program. Details of the X-20 design are briefly discussed in terms of objectives and constraints which influenced the final design. The test station and its capabilities are described. Test results through cycle 100 are presented and compared with similar results in similarly constructed 500-Wh and 3-kWh battery systems. The second half of this section describes the refurbishment and autopsy of the 10-kWh (X-10) battery built during the Phase I program.

III.1 20-kWh (X-20) Battery Testing

III.1.1 Design Concepts and Objectives

A major portion of the Phase II development effort was devoted to assembling and testing X-20, a 20-kWh bipolar battery system. The objective was to scale up the zinc-bromine battery system to 20 kWh capacity, and to demonstrate a minimum of 50 deep charge-discharge cycles at that capacity level. Another objective was to look for scale sensitive performance characteristics by comparing its electrical behavior to earlier, smaller test units. While it might have been preferable to assemble X-20 with larger electrodes than the 580 cm^2 size used in batteries heretofore, the long lead time required for tooling and pretesting larger electrodes made this approach impractical. Consequently, the decision was made to use existing components to assemble 52-cell stacks, which were then used as building blocks for X-20. Six such stacks were paralleled, electrically and hydraulically, into a single battery to achieve the desired capacity rating. An added feature of this design approach was that it allowed us to test a large battery made up of paralleled modules. The six stacks were bolted to the central feed block to form a single battery which rested atop the electrolyte reservoir, as shown in Figure III-1. Electrolyte flow was directed from the reservoir into the main feed block where machined flow channels effected distribution to the individual stacks. Likewise, the electrolyte flow streams emerging from the individual stacks were directed into flow channels in the main feed block where they were returned to the appropriate reservoir. This design eliminated external electrolyte flow lines. Pretesting of the main feed block showed its design to provide uniform flow distribution among the individual stacks.

The need to provide shunt current protection in a 52-cell battery (nominally 80V on discharge) with a common electrolyte manifold has been discussed in detail before.[1] This was done by applying a nulling voltage to each individual manifold, as had been done on the 10-kWh (X-10) battery and other previous 3-kWh (X-3) modules. However, six modules in parallel presented a potentially more complex system,

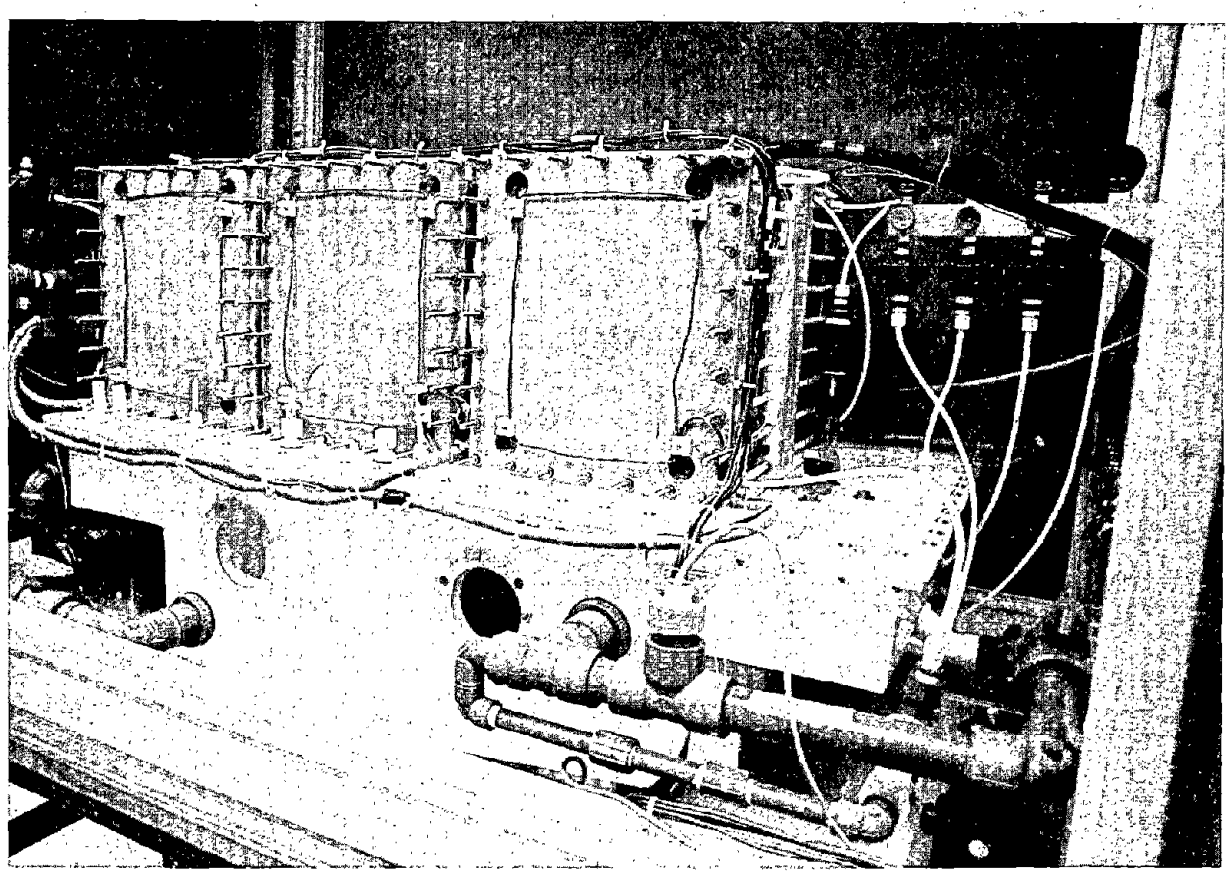

Figure III-1 20-kWh (X-20) Battery

and, therefore, some simplifying design modifications were made. The protective graphite electrode was modified to reduce the effective current density, and to replace the threaded contact with one made by compression. This change provided a better liquid seal around the protective electrodes, and also accelerated stack assembly by eliminating the need to align mating threads. In addition, the separate "oil" pump used to supply catholyte emulsion (polybromide complex) to the bromine-reducing protective electrodes was eliminated by diverting a portion of the catholyte stream into a direct feed line. An in-line throttling valve was used to regulate the required flow rate. Another simplifying modification was to apply the same protective voltage to each battery module rather than to each individual manifold as had been the practice hitherto. This was simply accomplished by separately connecting the anodic and the cathodic protective electrodes (in parallel). This reduced the shunt current protection control requirements fourfold. Subsequent test results showed that this simpler approach to shunt current protection was feasible.

The need to provide some active form of cooling when operating a large battery had become apparent during the testing of the X-10 battery. Inefficiencies resulting from polarization losses, pumping inefficiency, shunt current protection, and self-discharge cause waste heat generation. All or a part of this waste heat should be removed to avoid excessive battery temperatures. Our design philosophy was to remove just enough waste heat to maintain battery temperature at 40°C or below (an arbitrary choice) at the end of a 7-8 hour operating cycle. Accordingly, 15 m of 1.25 cm FEP tubing was installed in the anolyte reservoir for cooling water circulation. This was part of a closed loop (a water conservation measure) wherein water was circulated at approximately 4 l/min. This proved quite adequate because the ΔT of the cooling water between inlet and outlet was 1-2°C and the temperature rise in the system, as determined from anolyte and catholyte temperature measurement, measured 12-14°C at the end of a 7 hour charge/discharge cycle. Future efforts in this area will examine air cooling to remove waste heat.

III.1.2 Battery Construction

As stated above, existing components were used to assemble six 52-cell modules for the X-20 battery. The unit cell consisted of a bipolar electrode, a Daramic microporous separator, and a 0.1 cm Vexar polypropylene mesh used as a spacer between the separator and electrode to maintain uniform flow. In addition, a 0.04 cm polypropylene spacer was used along the outer edges between the separator and electrode to adjust the gap so as to achieve line contact. The electrodes were made by injection molding; a glass filled polypropylene frame was overmolded on the carbon-plastic electrode. Active electrode area was 580 cm^2, and intercell spacing (unit cell thickness) was 0.34 cm. A cutaway view of the unit cell is shown in Figure III-2. The 20 kWh capacity rating was based on a 90 mAh/cm^2 zinc loading, 80% coulombic efficiency, and an 80V nominal discharge voltage.

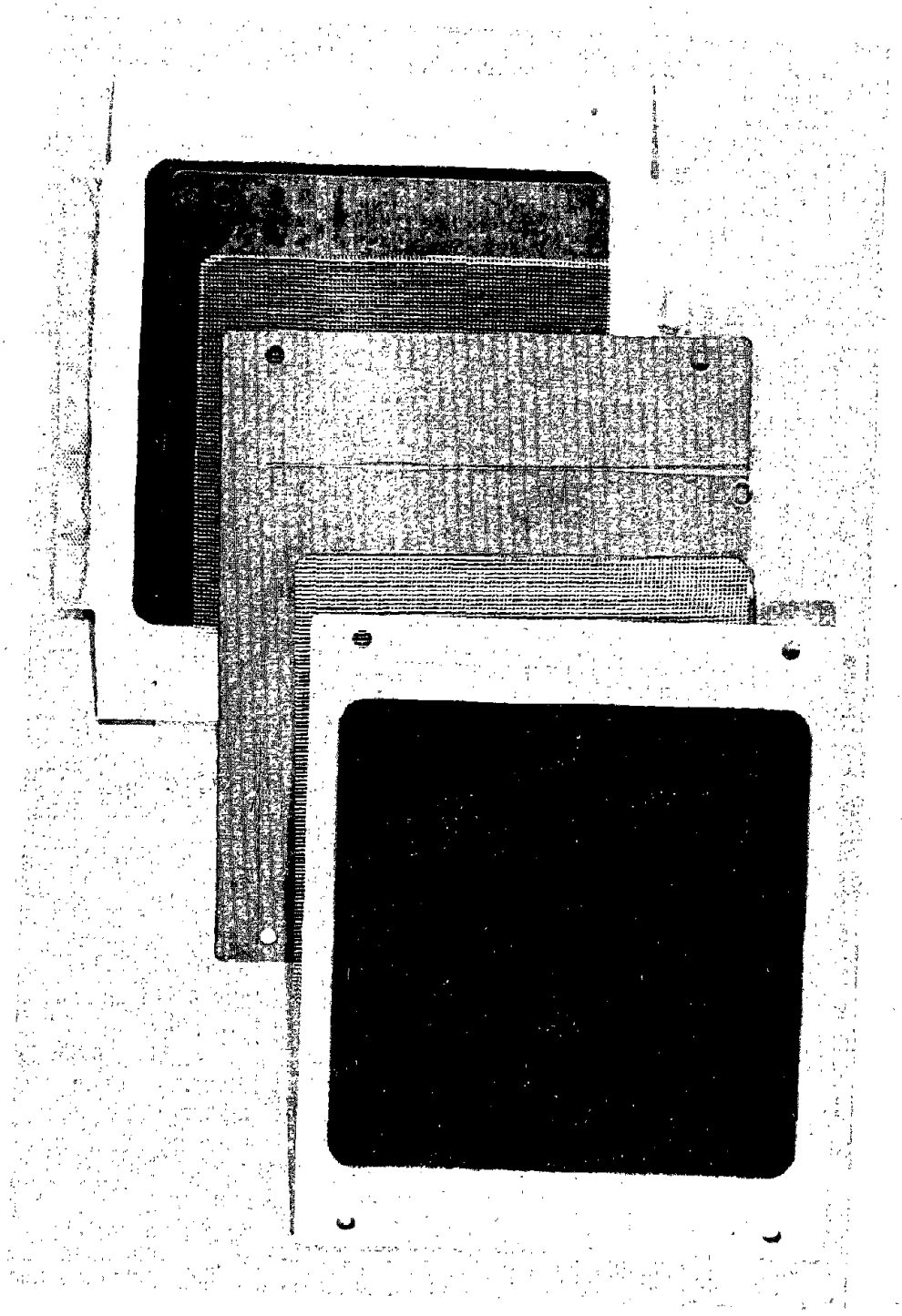

Figure III-2 Exploded Unit Cell of 20-kWh Battery (X-20)

The electrolyte reservoir was a custom designed tank, constructed of 0.95 cm polypropylene with a gasketed cover made of 1.95 cm polypropylene to support the weight of the battery. The tank was sized to contain 156 l of electrolyte, and an internal partition separated the anolyte and catholyte compartments. The partition did not extend to the top of the tank; it was designed to form a weir to avoid an overspill in the event of a severe cross-flow problem. The electrolyte was 3 M Zn/Br_2, 1 M Br_2 complexing agent and 0.1% polyelectrolyte additive. The pumps were 24V DC motor driven magnetically coupled centrifugal pumps, and the electrolyte circulation rate was 45 l/min. The battery system was set in a tray sized to contain a maximum spill, and the tray was set in a hood constructed specifically for this test purpose. This arrangement complied with in-house safety requirements.

The cycler was a regulated 24-kW dc power supply adjustable to 0-160V dc and 0-300 A. It was operable either manually or automatically, with adjustable high voltage and low voltage cutoffs. The cycler included an inverter to return the battery discharge capacity into the ac line. This feature served as an energy conservation measure, and avoided the problem of dissipating 5-10 kW when discharging the battery. Shunt current protection was supplied by an external dc power supply which, typically, operated at 2-4V above battery voltage and supplied approximately 3-3.5 A to the total battery. This represented 4-5% of the average charge-discharge current. A voltage follower circuit automatically adjusted the protective voltage in accordance with changes in battery voltage. The battery was heavily instrumented to record manifold voltages, and positive and negative boost voltages. In addition, battery voltage, total battery current and current distribution among the individual battery modules, anolyte and catholyte temperatures, and cooling water inlet and outlet temperatures were monitored. These data points were computerized to provide a printed record at preselected time intervals.

The battery system was also equipped with safety features designed to shut the system down in the event of an out-of-tolerance operating condition. Included were electrolyte levels, electrolyte flow rates and pressures, battery temperature and cooling water flow. The safety system was designed so that in the event of an unscheduled shutdown, the battery was connected across a 1.6Ω, 7-kW load bank by a latching relay. The reasoning behind this approach was to discharge and short the battery in the event of an unscheduled shutdown rather than to allow it to sit on open circuit without shunt current protection. Tests indicated that the stacks would discharge totally within one hour under these conditions.

III.1.3 Test Station Description

Site preparation and test station construction were major tasks in this program. The sub-tasks required in preparation for battery testing included the following:

A. Installation of Hood and Utilities

A 183 cm x 91 cm hood was designed and constructed to house the battery during its testing phase. The hood was installed in one of our laboratories where work benches and a sink were cleared to make room for the hood and test instrumentation. The required utilities included a vacuum line, water and electrical power, 440 V ac for the cycler and 120 V ac for the power supplies (pumps and shunt current protection) and monitoring instruments. The hood was interlocked with the safeties to turn the battery off and to turn an audible alarm on in the event air circulation was lost.

B. Installation and Testing of Sensing Wires

As stated above, the battery system was heavily instrumented to monitor operating conditions and performance. This required installing and testing the diagnostic sensing leads. Testing was done by applying a simulated voltage signal and looking for isolation and proper response.

C. Installation of Reservoir/Battery

The electrolyte reservoir, sized to contain 156 l of solution, was set inside a tray in the hood. The pumps, as may be seen in Figure III-1, were located in the tray beside the reservoir. The anolyte pump inlet was a 3.2 cm I.D. PVC pipe. The pump outlet was a similar pipe which was fed through the reservoir wall, terminating at the anolyte inlet port of the central feed block. The catholyte feed line was of a similar arrangement, except that the pump inlet was a dual line for mixing aqueous and "oil" phases. A separate "oil" line from the pump outlet to the shunt current protective electrodes on the zinc side of the battery supplied the required polybromide complex. Paddle type flow meters in the anolyte and catholyte flow lines were used to monitor the 45 l/min. electrolyte flow rates. Pressure gauges in the inlet side of the battery were also installed to serve primarily as a visual check on "normal" electrolyte flow. Under "normal" operation, the pressure readings on the anolyte and catholyte lines were ~35 kPa.

The battery, which had been assembled earlier, was placed atop the reservoir cover so as to align the electrolyte inlet ports in the central feed block with the appropriate pump outlet flow pipes. The "oil" emulsion supply line to the shunt current protective electrodes was installed and the entire system was water tested. This entailed filling the reservoir with 150 l of de-ionized water and circulating it

over a period of several days to ascertain that the system was leak tight. The system was then drained and the electrical hookup was completed, which included the power lines and the sensing leads. This was followed by filling the system with 156 l of electrolyte (3 M $ZnBr_2$ and 1 M quaternary ammonium bromide) and retesting it for leak tightness.

The final step was to set and test the operating safety limits. Setting the limits was done by simulating an out-of-tolerance condition of a preselected level, adjusting the appropriate limit switch to that level and then retesting it for a response. The safeties included high pressure (obstructed flow), low pressure (reduced or no flow), battery overtemperature (50°C), cooling water flow (go, no-go), electrolyte levels (anolyte and catholyte), high/low pressure in the "oil" line to the protective electrodes, and air circulation in the hood. The cycler had its own built-in safety wherein the test cycle was aborted in the event ac power was lost for 30 seconds or longer.

III.1.4 Test Results

Testing of X-20 started with low rate (10-15 mA/cm^2), shallow cycling aimed primarily at ascertaining that all parts of the battery system functioned in the anticipated manner. Thus, cycle #1 was a 35A charge for 60 minutes (10 mAh/cm^2 zinc loading), followed by a discharge at the same rate to a 50V cutoff (1V/cell). Charging current and time were gradually increased. The charging current used routinely was 70A and the charge time was adjusted in accordance with the desired input. The discharge rate most frequently used was also 70A with all efficiency calculations based on the capacity obtained to a 50V cutoff. During the first 25 cycles, the charge input was varied between 60-100 mAh/cm^2 zinc loading (capacity rating is based on 90 mAh/cm^2), and, thereafter, a more routine C/D cycle was used. The routine cycle consisted of a 70A charge for 225 minutes (75 mAh/cm^2 zinc loading), and a 70A discharge to 50V. This input represented 83% of the rated capacity.

As stated earlier, one of our objectives was to compare the behavior of X-20 to those of earlier, smaller units to demonstrate that scale-up did not result in diminished system performance. Figure III-3 compares polarization data of three bipolar batteries of different capacity ratings, ranging between 500 Wh and 20 kWh. The slopes of the lines vary between 0.52 ohm and 0.67 ohm. The variation in resistance values does not show a trend with battery size, and is believed to be due primarily to variation in separator resistance.

A voltage vs time plot of X-20 during a complete charge-discharge cycle is shown in Figure III-4. Here the battery was charged at 70A (20 mA/cm^2) for 180 minutes and discharged at the same rate (for 147 min) to a 50V cutoff. Voltaic efficiency on this cycle was 80%, and energy efficiency was 65%. Similar data taken earlier under comparable test conditions on a 500-Wh battery are also plotted on the same graph for comparison. As may be seen, the charge curves superimpose, and the discharge curves are quite similar. The major difference is in the sharpness of the knee at the end of discharge which is related to a bad cell in stack E (see below).

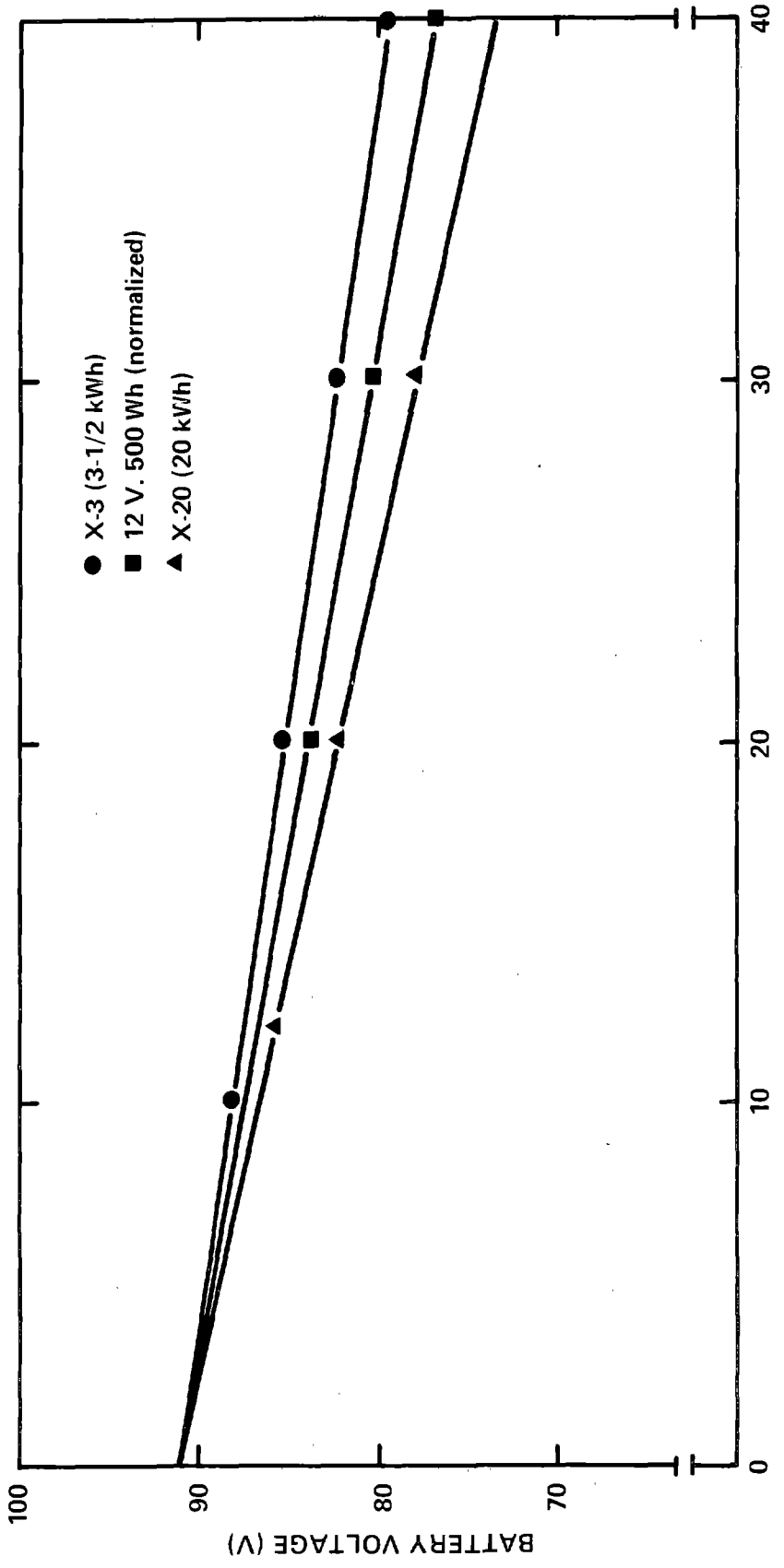

Figure III-3 Polarization Data for 600 cm^2 Batteries

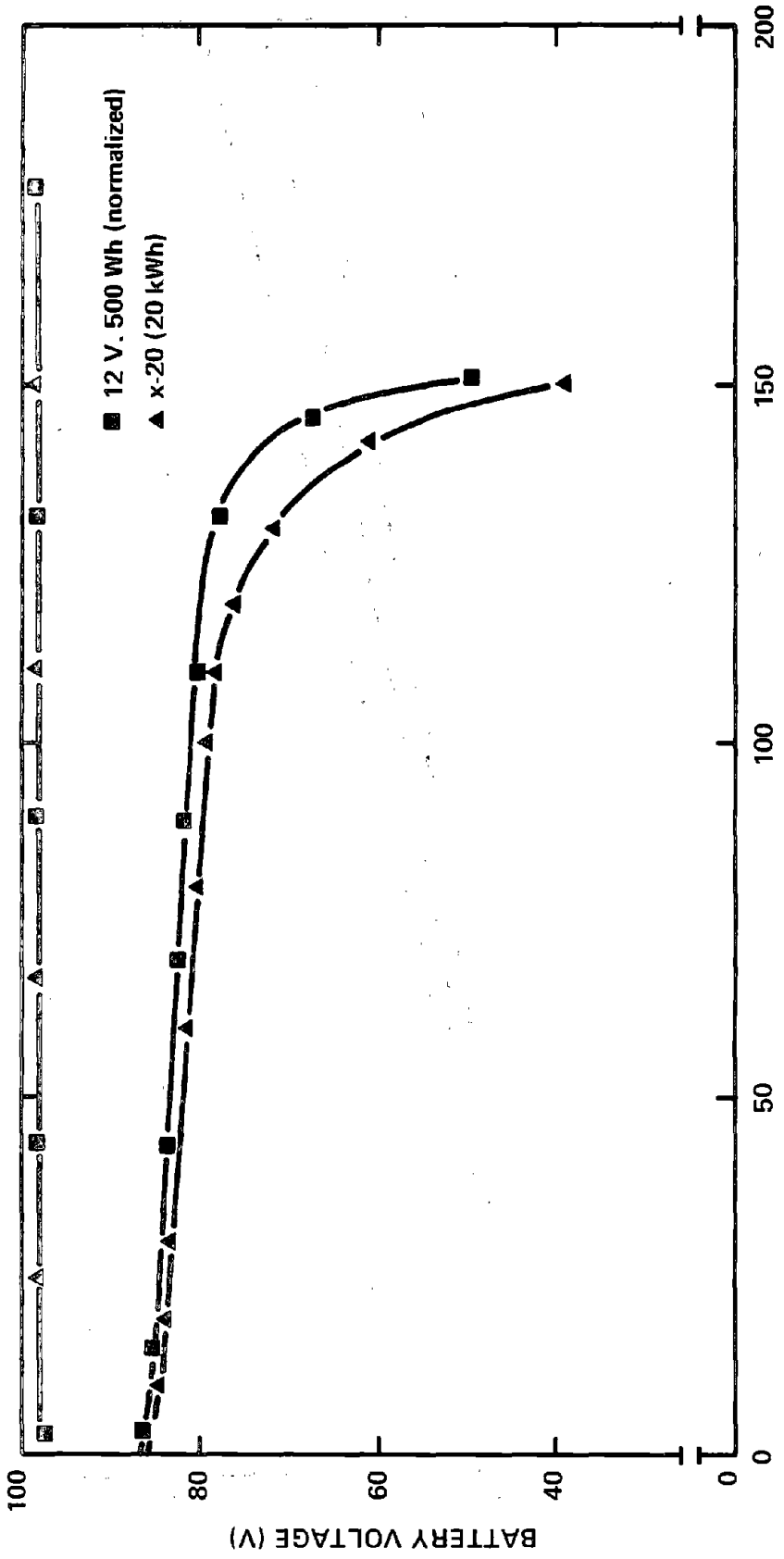

Figure III-4 X-20 Charge/Discharge Cycle Plot

Figure III-5 shows efficiencies vs cycle life for 100 charge-discharge cycles. Although the Phase II program goal was to demonstrate 50 deep cycles, cycling was continued, and at this writing the battery had passed the 100 cycle mark with stable performance. Cycle testing is continuing.

The plot shows coulombic, voltaic and energy efficiencies of all even numbered cycles. The pertinent data, charging times and current, discharging times and current, energy imput and output, zinc loading, and the various efficiency figures are tabulated for each cycle and are included as Appendix III.

During the first 25 cycles, charge times were varied to vary the zinc loading. Charging and discharging currents were, for the most part, kept at 70A (20 mA/cm^2). Zinc loadings up to 100 mAh/cm^2 were used in these tests, which account for the scatter in efficiency values during the initial portion of cycling. After cycle #25, 0.1% of polyelectrolyte additive was added to the electrolyte and a more routine test was adapted. Here, charging was done for 225 minutes followed by a 5 minute open circuit rest, and a discharge. Current was 70A for both charging and discharging (75 mAh/cm^2 zinc loading) and that cycle was the predominant test routine. The frequency was one cycle per day. With the repetitive test routine, cycling performance was more reproducible. While performance was quite stable and reproducible over the span of 100 cycles, the levels (efficiency) were somewhat lower than anticipated. At the rates and zinc loadings used, the anticipated coulombic efficiency was 80%, and with an 82-84% voltaic efficiency, the expected energy efficiency was 65-68%. Actual performance levels were lower, and in pursuing the possible cause, we have found that one stack (E) had a somewhat lower open circuit voltage than the other stacks. However, whatever may be the cause of this misbehavior, battery performance did not appear to deteriorate. The suspected problem is a "broken" cell component in one of the cells allowing some catholyte to get across a bipolar electrode into the anolyte. By monitoring the current into each stack, on charging Stack E drew somewhat more current than the other stacks, while on discharging it delivered somewhat less current than the others. This pattern was observed throughout the test program, and did not worsen or improve. This behavior attests to the "forgiving" nature of the system.

Some observations made in the course of testing X-20 may be added. According to our information, this battery is the largest bipolar unit which has successfully completed 100 deep charge-discharge cycles and is continuing to perform in stable fashion. Its voltage behavior, under similar test conditions, has been quite reproducible. The shunt current protective electrodes have also shown stable performance. Boost voltages have remained constant through the test period, suggesting that the design changes made here were effective and beneficial.

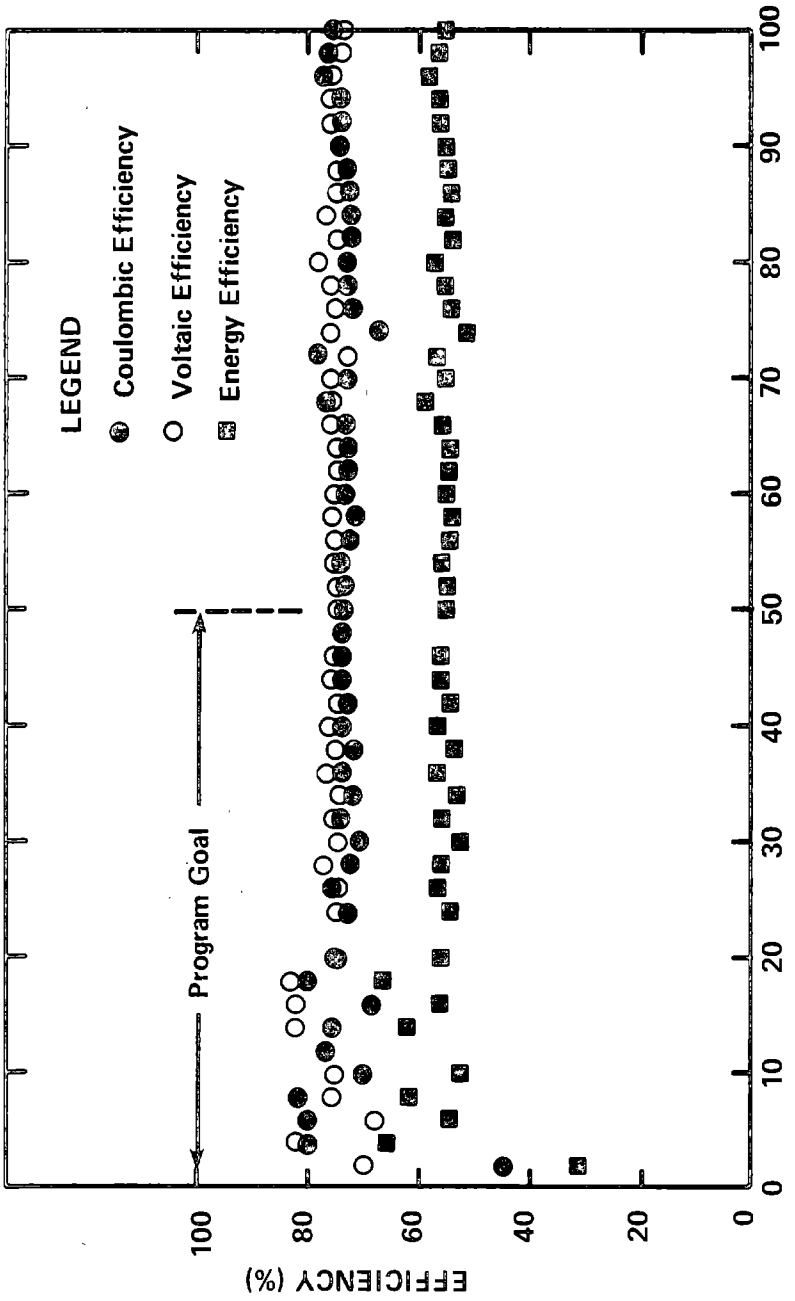

Figure III-5 X-20 Cycle Performance

The cooling system has been trouble-free and effective, and has performed as anticipated. Battery temperature rose less than 15°C at the end of an 8-hour C/D cycle, and this kept battery temperature below the 40°C design limit at all times.

In general, the difficulties encountered in testing the 10-kWh (X-10) battery, such as Pt contamination, electrolyte cross-flow, and heat exchanger problems, were instructive in that they helped to focus attention onto a potentially problematical area, and the lessons learned in the assembly and testing of X-10 have contributed to the successful results achieved with X-20.

III.2 10-kWh Battery Refurbishment/Autopsy

The previous Phase I contract entailed the construction and 50 cycle testing of a 10-kWh zinc-bromine battery. At the end of the contract, those goals had been attained. However, as was reported, there was a significant gassing problem which became progressively more severe after cycle 30. Its cause has been traced to the corrosion of the Pt voltage sensors placed on each cathode in order to provide individual cell voltage readouts. Also, the battery, by the end of the 50th cycle, evidenced declining coulombic efficiency and discharge rate capability. There had also been a few temperature excursions (to near 60°C) due to cooling line difficulties.

It was, therefore, decided to disassemble the battery in order to: 1) replace the electrolyte with Pt free electrolyte and to remove the Pt tabs; 2) repair the cooling lines; and 3) repair a cross-flow problem within the main electrolyte flow distribution manifold. This latter problem had been present since the original assembly and was the most likely cause of the initial coulombic efficiencies, being in the 70+% instead of 80+% range.

III.2.1 10-kWh (X-10) Battery Refurbishment

In order to accomplish the modifications outlined above, the battery was discharged and all of the Pt contaminated electrolyte was transferred into 5 gallon plastic containers. In these containers, the excess Br_2 was reduced with sodium thiosulfate prior to disposal. (Two gallons were retained for future studies.) The battery was then flushed four times, for three hours each, with a dilute KBr solution which had been acidified with HBr. The purpose of the salts was to aid in the removal of Br_2 from the high surface area cathode layer. After the washings, the three individual 52-cell modules were removed intact and the remaining plumbing was disassembled. During the disassembly, some "residual" solids were found, especially in the anolyte tank.

When the main electrolyte flow distribution manifold was disassembled, it was obvious from the Br_2 stains on the plastic that there had been electrolyte crossflow of catholyte into the anolyte. This finding had been anticipated and was probably responsible for some or all of the lower than expected coulombic efficiencies experienced in X-10 testing. The internal leakage was repaired by inserting a closed cell polyethylene gasket between the two manifold halves. This gasketing eliminated the cross flow problem when the battery was later reassembled. Similar gasketing was used in X-20.

The original cooling system had used a short tantalum heat exchanger which was immersed in the anolyte tank and had flowing water coolant. Upon disassembly, it was found that the plastic fitting at one end of the Ta pipe had loosened and was leaking. Since cycling experience had shown the need for heat removal, the original system was removed and replaced with a fluted polypropylene tube similar to that which was planned for the 20-kWh (X-20) battery. This new system gave improved heat management when the X-10 was reassembled. The new design also provided valuable data for the X-20 cooling design.

The platinum voltage tabs were removed from each of the three modules. As anticipated from the Pt found in the electrolyte analysis[1], several of these tabs showed severe etching. After the battery was reassembled, it was filled with a 0.8 M KBr, 0.1 M Br_2 electrolyte and charged and discharged at low rates in an attempt to form bromoplatinic acid out of any Pt which still remained within the battery. This solution was then removed. The battery was then filled with 76 l of standard electrolyte (3 M $ZnBr_2$, 1 M quaternary ammonium bromide) in order to resume testing.

III.2.2 Testing Characteristics

The X-10 battery, following reassembly, was cycled for an additional 15 cycles. The overall battery performance was similar to that prior to disassembly except that the gas evolution was vastly reduced. The coulombic efficiencies increased to 45-48%. However, the lack of good discharge rate capability, which had been a problem since cycle 30, continued. The gas evolution was reduced to virtually none on the first cycles and increased to a few hundred milliliters by cycle 15. This increase is thought to be the result of residual Pt or, possibly, new Pt from the shunt current voltage sensors which had to remain in place.

On the 13th cycle (63 on the battery), a plastic coupling on the cooling system broke and filled the electrolyte tanks to overflowing with water. [These couplings were placed external to the tanks on X-20.] While two additional short cycles were attempted, the lack of cooling prevented meaningful results and testing of X-10 was terminated.

III.2.3 Autopsy

The final disassembly of X-10 was postponed until after the 20-kWh battery was completed. When the autopsy was begun, it was decided to keep the three battery stacks intact so that they could be tested as individual 3-kWh units. The electrolyte tank and plumbing showed no unusual wear other than Br_2 staining. The closed cell polyethylene gasket also showed no degradation.

Stack B was totally disassembled in a charged state. There was evidence of gas bubbles in the zinc plate as would be expected. Also, there was a slight warpage of the electrodes, but it appeared not to affect the electrolyte flow. The most significant finding, however, was that when the zinc deposit was etched off with HCl, a "waxy" polymeric substance was left on the anode surface. Efforts are currently underway to identify the nature and source of this "waxy" deposit.

SECTION IV

Parametric and Life Testing Studies

The purpose of this task is to broaden the experimental data base of the zinc-bromine battery system. During Phase II, these efforts were focused on: 1) cycle life testing; 2) performance testing of components; 3) mass balance studies of electrolyte components during battery cycling; 4) evaluation of electrolyte additives for high rate battery performance and lower operating temperature capability; and 5) properties of quaternary ammonium polybromides relevant to system safety considerations.

IV.1 Cycle Life Testing

During Phase I of this program, life-cycle testing was begun on shunt current protected 500 Wh (8 cell) zinc-bromine battery systems on an around-the-clock basis. These continuous life-cycle studies have been extended to a second automatic life cycle test station and, in addition, two new test stations which allow automatic cycling of two non-shunt current protected 500 Wh (8 cell) systems on a three cycle per day regime were added. Since these units are not shunt current protected, they are automatically shorted out after the third discharge to remove any zinc deposits in the manifolds. These "automatic daily cycling" units are based on the Texas Instruments 5TI programmable control system used in the "continuous automatic cycling" units described in the Phase I Final Report.

IV.1.1 Continuous Automatic Cycling Results

At the end of the Phase I contract, life-test stack #3, which will be referred to as stack PAM-4, had accumulated more than 100 continuous cycles of operation at various depths of discharge corresponding to zinc electrode loadings of 10-75 mAh/cm^2. This particular stack was constructed using insert injection-molded carbon-plastic bipolar electrode/flow frame components and 0.076 cm flat Daramic separators with Vexar secreens (0.100 cm) as the flow spacers. Platinum cell voltage sensors and shunt current system sensors were used in this stack. Testing was carried out with 4 l of 3 M Zn/Br_2 - 1 M quaternary ammonium bromide electrolyte to which 80 g of Br_2 (0.125 M) had been added.

The cycling of this battery stack was carried out using a cycle regime which consisted of a number of continuous shallow depth cycles at zinc electrode loadings of 15-30 mAh/cm^2. This "accelerated" cycling regime was designed to subject the battery components to the stress of many charge/discharge cycles with the deeper depth cycles (to 75 mAh/cm^2) used to determine any degradation in battery performance as a result of this repeated cycling.

Figure IV-1 shows the performance of battery stack PAM-4 in terms of its coulombic efficiency at the 15-30 mAh/cm^2 depth cycles and at the 75 mAh/cm^2 performance measurement cycles. During the initial

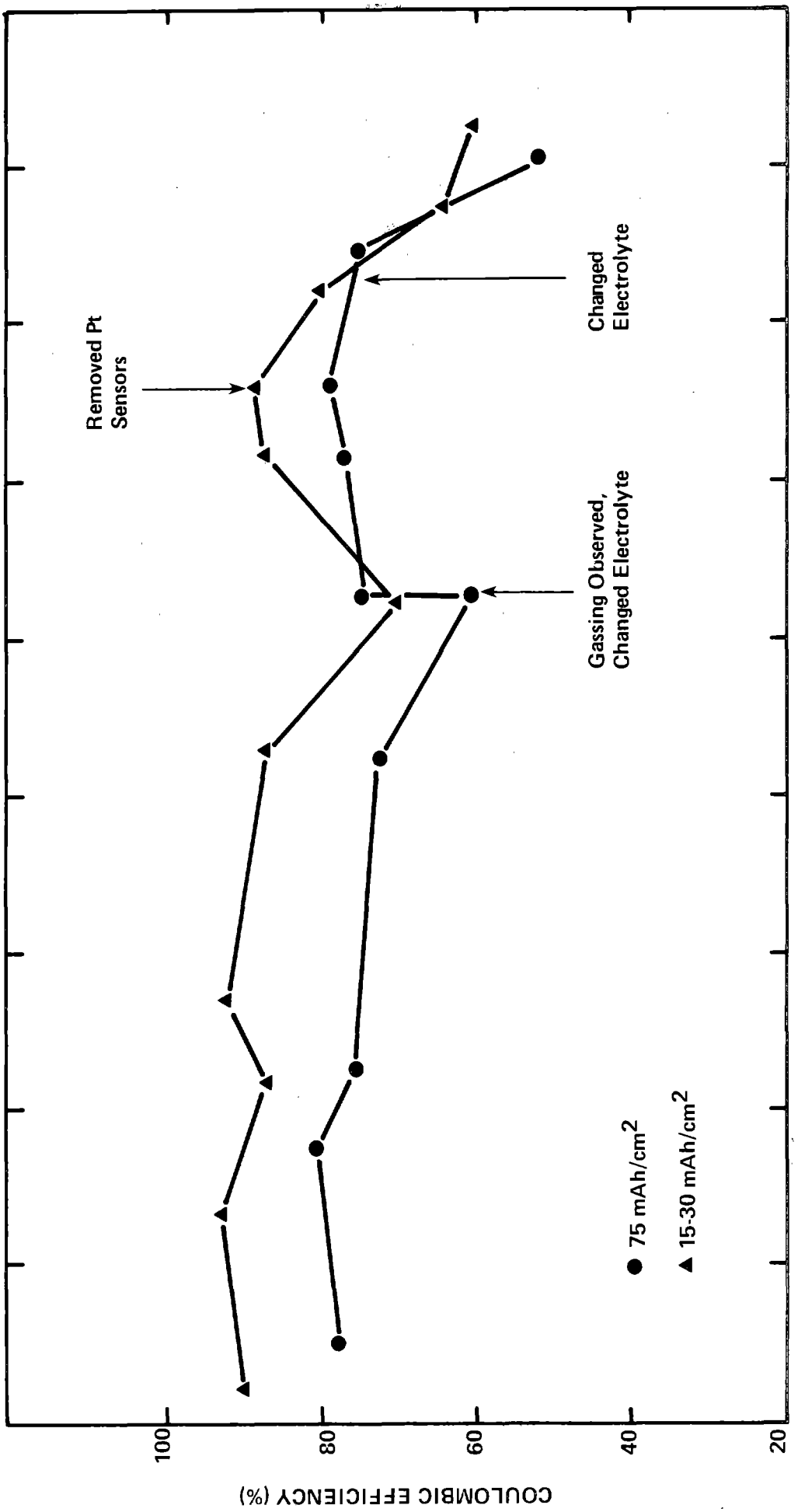

Figure IV-1 Continuous Life Cycle Testing - Stack PAM-4

200 cycles, coulombic efficiency remained constant at both levels of zinc electrode capacity. Slight gassing was observed in the anolyte stream during cycle 213 (at 75 mAh/cm^2) and the coulombic efficiency showed a decline to 73% from an average of 78 $\pm$3% for the previous 75 mAh/cm^2 cycles. By cycle 263, the gassing in the anolyte stream became significant during battery discharge and the coulombic efficiency dropped to 61%.

At this point in the cycling, an electrolyte pH of 3.4 was measured. This increased pH level was felt to be a result of the severe H_2 evolution observed, and rather than attempting to lower the pH by HBr addition, the electrolyte was drained from the system and new electrolyte added.

As cycling resumed, coulombic efficiency increased to 76% during cycle 264 (75 mA/cm^2). However, as Figure IV-2 shows, the shape of the discharge curve has changed in the cycling. The average voltage during discharge has dropped from 12.5V (cycle 112) to 10.5V (cycle 263). Continued cycling, while maintaining a coulombic efficiency of 75-79%, still showed poor voltage behavior during discharge and gassing again became evident. At cycle 332, the Pt cell voltage sensors were removed with no effect on the gassing. A second electrolyte change was carried out at cycle 359 with little effect, and performance continued to decline. Cycling was terminated after cycle 411 and the stack autopsied in the discharged state.

Autopsy of this stack revealed no evidence of component warping or zinc dendrites. Examination of the Daramic separator revealed the presence of a grayish layer on the anode (zinc electrode) side of the separator. A comparison of the resistivity of used (411 cycles) and new Daramic separator material showed no measurable difference due to this layer. Therefore, the poor performance observed in the life test stack does not appear to be separator related. We have also compared the surface area of cycled and new cathodes by measuring their double layer capacities. These measurements show, at most, a 20% decrease in the apparent area of PV-1 coated carbon-plastic after 411 cycles. Attempts to measure the surface area of new and cycled uncoated carbon-plastic electrodes by their double layer capacity were unsuccessful and more reproducible data were obtained by comparing polarization curves for Br_2 evolution under identical conditions. At current densities between 1-10 mA/cm^2, new carbon-plastic electrodes show 100-155 mV more polarization than cycled carbon-plastic electrodes, indicating that a significant increase in surface area occurs during anode cycling. However, it is not clear just what effect, if any, this surface roughening has on anode behavior.

Based on autopsy results, the failure of this battery stack appears to be due to the excessive gassing which leads to poor flow distribution and increased internal cell impendance. Based on the observations regarding the effects of platinum contamination of zinc corrosion/H_2 evolution which were made in Phase I,[1] the excessive gassing observed can be attributed to corrosion of the Pt cell voltage or shunt current protection system voltage probes.

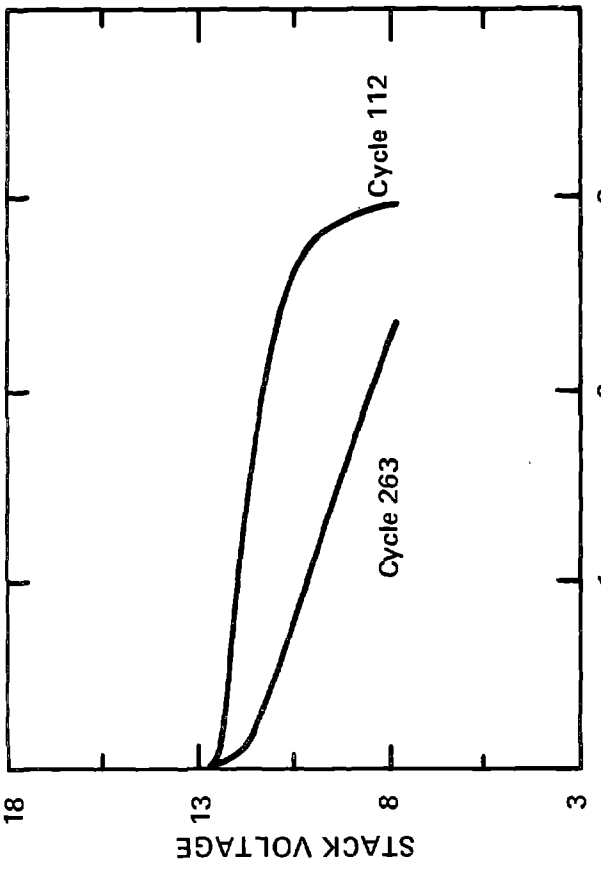

Figure IV-2 E vs t Behavior After
Continuous Life-Cycle Testing - Stack PAM-4

Stack PAM-6 was constructed with the same design as stack PAM-4, but the Pt cell voltage probes were replaced by carbon-plastic cell voltage probes. Pt sensors were used, however, in the shunt current system voltage probes. The cycling regime used in the testing of stack PAM-6 was similar to that used in the testing of stack PAM-4, except that the performance measuring deep discharge cycle was carried out at 90 mAh/cm^2 zinc loading. The behavior of this stack is shown in Figure IV-3 where the coulombic efficiency data are plotted for the shallow depth (30 mAh/cm^2) and deep depth (90 mAh/cm^2) cycles.

As shown in Figure IV-3, coulombic efficiencies were constant for 200 cycles, and then a significant drop occurred. Gassing became very evident in the anolyte at cycle 152. Cycling was continued to cycle 249, at which point the electrolyte was drained and replaced with fresh electrolyte. While the coulombic efficiency did improve from 23% in cycle 247 to 55% in cycle 252, gassing was still evident and cycling was terminated after the charge portion of cycle 253.

On disassembly of Stack PAM-6 in the charged state, the zinc plate looked very uniform, although it was very easy to remove it from the underlying carbon-plastic substrate. Gravimetric analysis of these porous zinc sheets (which could be removed as an intact coating) showed an average weight of 55.4 $\pm$ 0.3 g, indicating very uniform plating. This weight was 87% of the theoretical value and this 13% loss corresponds to a "self-discharge" rate of $\sim$ 2.6 mA/cm^2 during stack charging. Some warpage of the bipolar elements was observed which had not been observed in life-cell stack PAM-4. Prior to disassembly, an I-E curve was run on this stack which showed a cell impedance of 8.5Ω cm^2, which was an increase from the 6.0Ω.cm^2 measured during cycle #63. However, this increase in stack impedance is not sufficient to account for its reduced coulombic efficiency. Since this autopsy had not found any apparent reason for the failure of this life test stack, excessive zinc corrosion due to Pt contamination of the electrolyte again appeared to be the main cause of the loss of coulombic efficiency. Excessive gassing was observed with this stack and the electrolyte showed Pt contamination.

In life-test stack PAM-7, a modification was made to the current collectors which allowed stack construction without the presence of platinum. Carbon-plastic sensors were molded into the manifold region of the collector and served as the voltage sensing electrodes in the shunt current protection system. In addition to this modified current collector, stack PAM-7 used a "posted" Daramic separator which was framed with polypropylene to minimize electrolyte leakage at the edge of the stack.

Stack PAM-7 was put through a total of 1403 cycles. Cycles 1-636 were carried out at a zinc loading of 5 mAh/cm^2 with periodic deep cycles at 90 mAh/cm^2. During cycles 637-1007, the zinc loading was increased to 15 mAh/cm^2. Cycles 1008-1403 were carried out at a zinc loading of 30 mAh/cm^2. The coulombic efficiency and energy efficiency

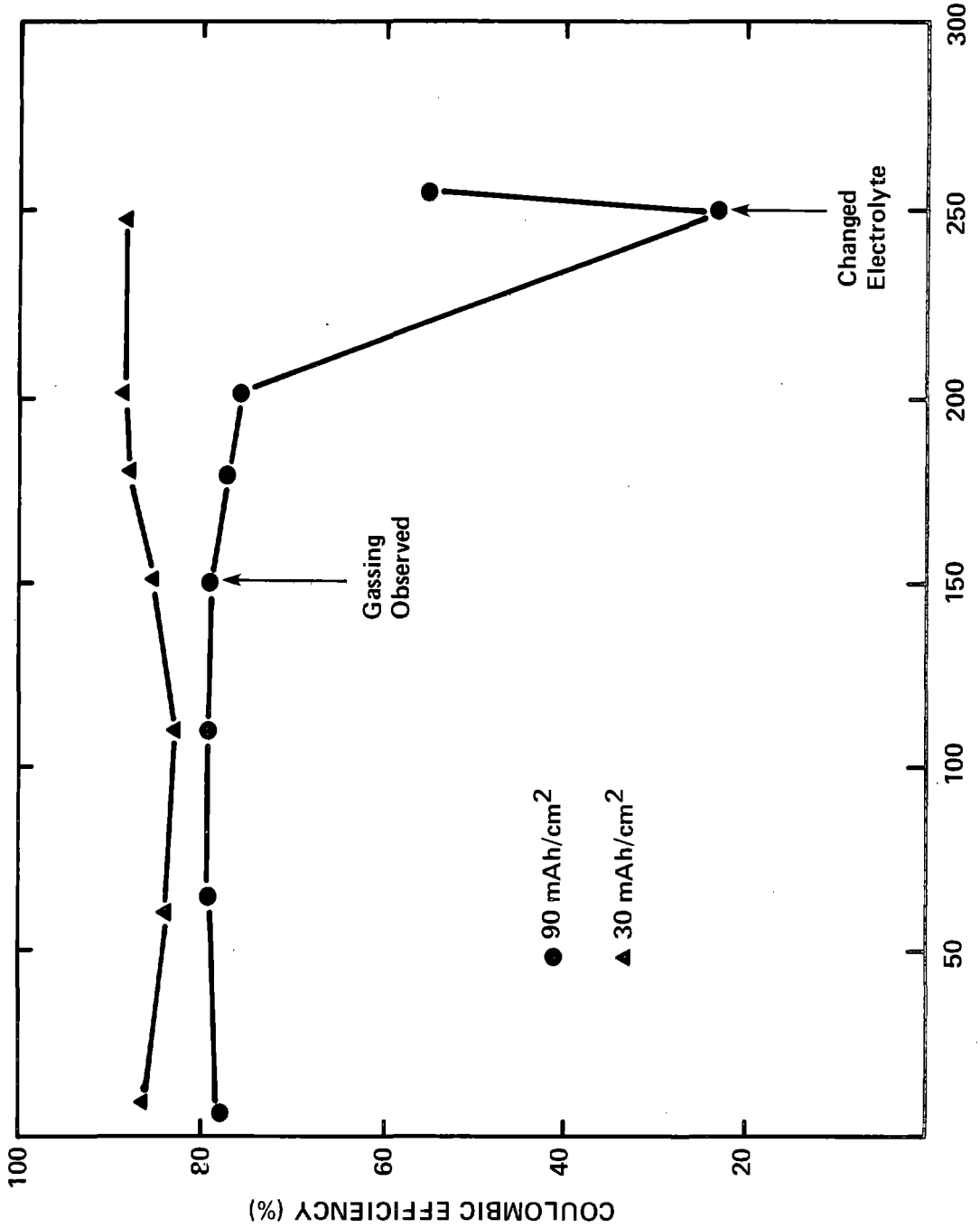

Figure IV-3 Continuous Life-Cycle Testing - Stack PAM-6

values measured during the 90 mAh/cm^2 deep cycles are shown in Figure IV-4. Stable performance was observed throughout the initial 1007 cycles, with coulombic efficiency maintained at 79 ± 3% and energy efficiency at 67 ± 3%. Coulombic efficiency began to decline during cycles 1100-1300, and dropped to 62% during cycle 1302. Cycling was continued to cycle 1404 during which the coulombic efficiency dropped to 50% at which point the testing was terminated.

The cycle behavior of this stack was distinctly different from that observed with stacks PAM-4 and PAM-6. At no point in the testing was gassing observed. At the end of cycling, the electrolyte pH was 2.5. Moreover, as Figure IV-5 shows, there was little change in the shape of the discharge curves aside from the reduced coulombic capacity. Figure IV-6 compares the E-I curves obtained at cycles 1136 and 1404. The polarization curve during cycle 1136 is essentially the same as that of the original stack and has a slope corresponding to an internal cell impedance of 4 ohm·cm^2. The internal impedance increased during cycles 1137-1403 to 5 ohm·cm^2. This increase is not sufficient to account for the decreased coulombic capacity since it would account for only a 240 mV change in battery voltage at the end of discharge.

Autopsy of stack PAM-7 in the discharged state showed carbon-plastic electrode warpage primarily near the edges of the electrode. There also was evidence of shorting via zinc deposits in this area. This area, near the edge of the electrode, corresponded to the edge region of the Daramic separator which did not contain the "posts". Presumably, this lack of support promotes carbon-plastic electrode warpage in these areas. It can be hypothesized that this electrode warpage leads to poor electrolyte flow in these areas and dendritic zinc deposits grow in these areas. Continuous cycling, without complete stripping of the zinc deposit, tends to encourage the growth of these deposits since they would tend to passivate during discharge due to lack of electrolyte flow. Once these growths extend into the separator, intracell shorting can occur readily. This shorting phenomena appears to be the prime reason for the loss in coulombic efficiency in stack PAM-7.

Table IV-1 summarizes the results of the autopsies on these three battery stacks. In this table, a "deep-cycle equivalent" was calculated using 52.2 Ah (90 mAh/cm^2) as the "deep-cycle" charge capacity and then dividing the accumulated charge capacity, e.g. 5530 Ah for stack PAM-4, by 52.2 Ah. Stacks PAM-4 and PAM-6 achieved 100+ deep cycle equivalents before testing was terminated due to increased gassing. Stack PAM-7 reached approximately 250 deep-cycle equivalents before testing was discontinued due to poor coulombic efficiency. Since stack PAM-7 did not contain platinum sensors, it appears that the excessive gassing in stacks PAM-4 and PAM-6 was due to platinum contamination of the zinc anodes causing significant zinc corrosion/hydrogen evolution. The warped carbon-plastic electrodes seen in stacks PAM-6 and PAM-7 were not evident in stack PAM-4. This warpage could be related to stresses from the insert injection molding or due to lack of proper stack compression. Such stresses could, in principle, be minimized by the co-extrusion

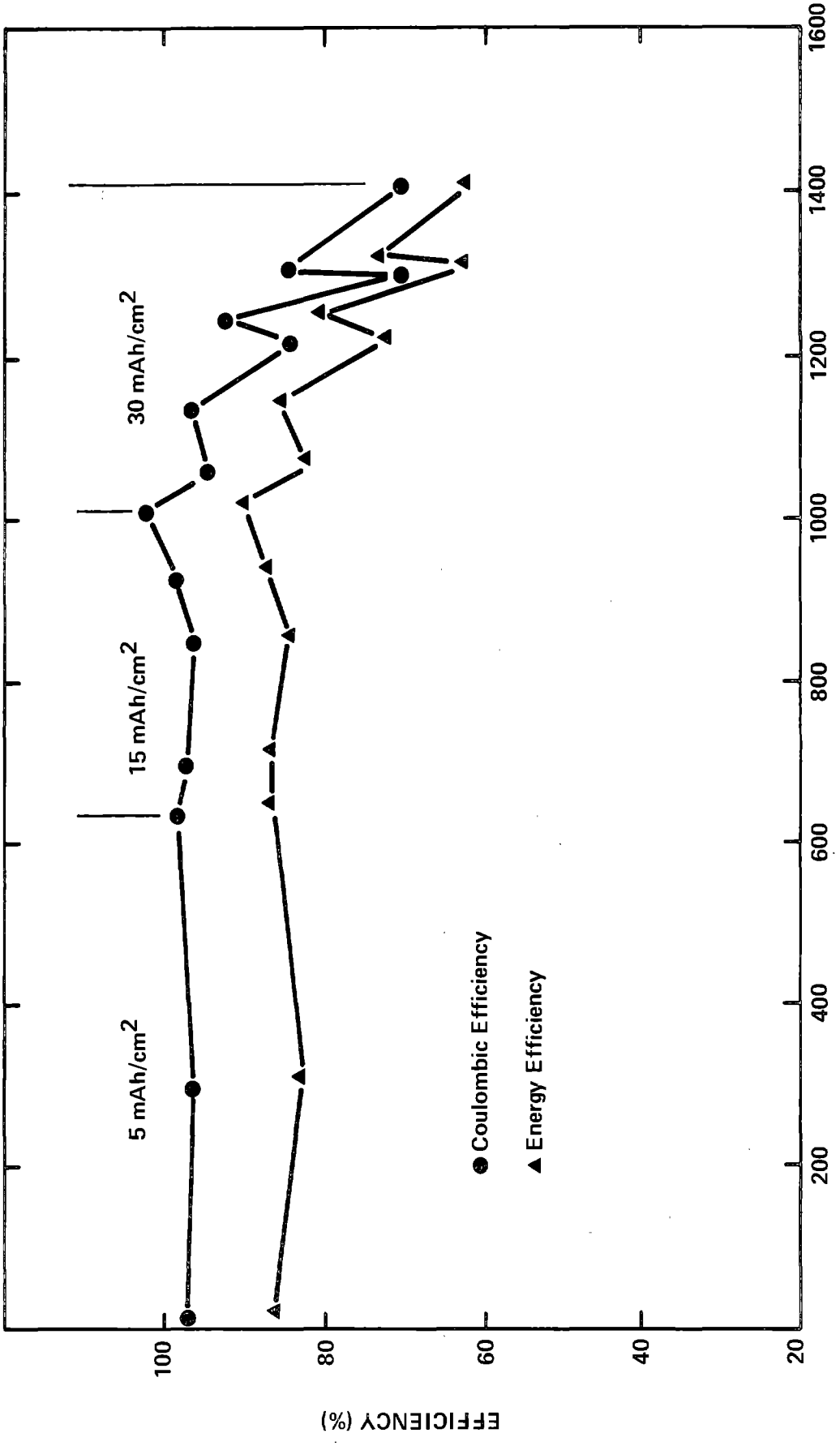

Figure IV-4 Continuous Life-Cycle Testing - Stack PAM-7

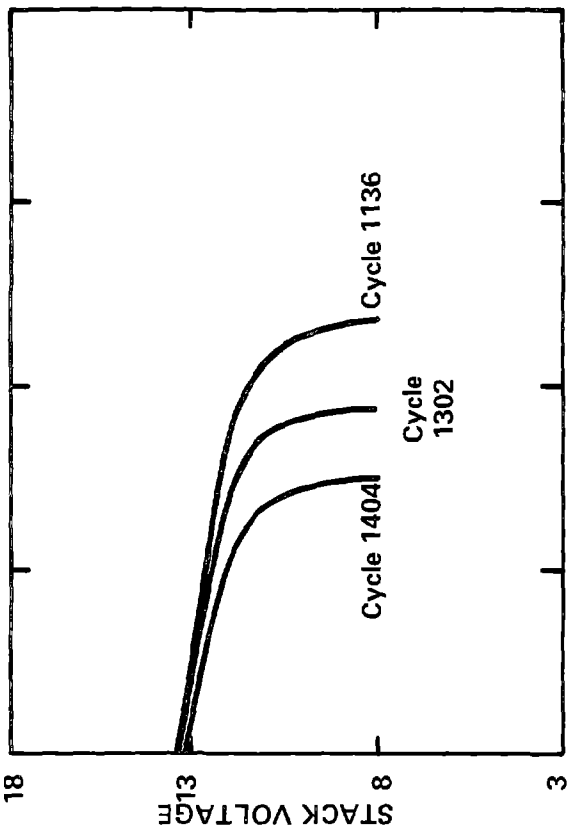

Figure IV-5 E vs t Behavior After Continuous Life-Cycle Testing - Stack PAM-7

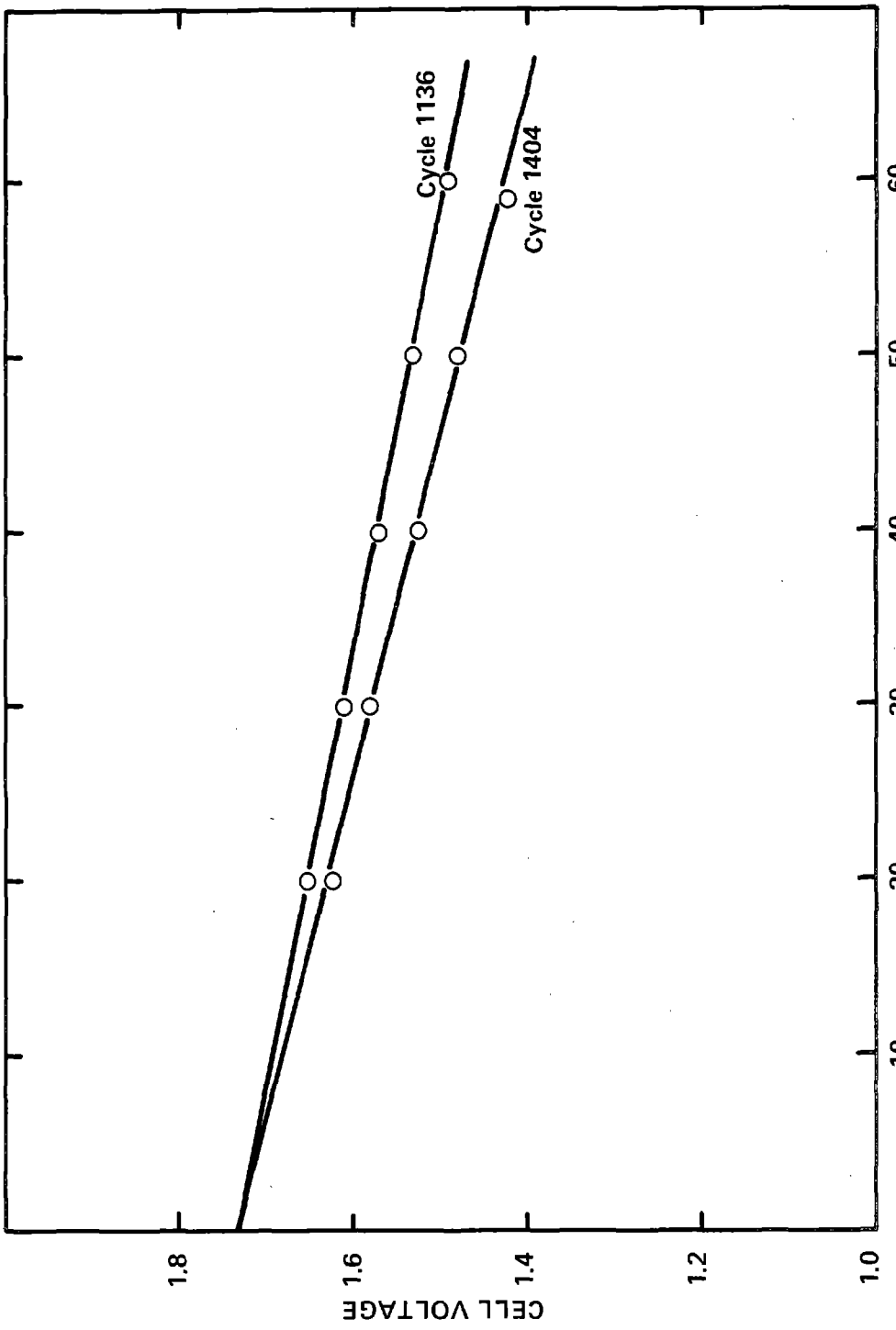

Figure IV-6 E vs I Curves After
Continuous Life-Cycle Testing - Stack PAM-7

Table IV-1

SUMMARY OF CONTINUOUS CYCLE BATTERY AUTOPSIES

Stack I.D.	Total Cycles	Deep-Cycle Equivalents	Observations Gassing	Warped Bipolar	Dendrites
PAM-4	411	106	X	---	---
PAM-6	250	102	X	X	?
PAM-7	1404	247	---	X	X

process now under development for bipolar electrode production. While internal cell shorting appeared to be a problem in stack PAM-7 due to dendrite zinc growths, this does not appear to be an inherent system problem and the formation of such deposits should be eliminated in the system with proper flow conditions. In all of this testing, the shunt current protection system has worked well, with no evidence or shunt current-induced zinc deposits in the stack manifolds.

IV.1.2 Continuous Daily Cycling Results

During Phase II, life testing was expanded using two new testing stations which allowed automatic cycling of non-shunt current protected 500 Wh (8 cell) stacks on a three cycle per day regime. Figure IV-7 shows the details of this daily cycle test regime. Three consecutive charge-discharge cycles were run at a current of 30 mA/cm^2 with a zinc electrode loading of 60 mA/cm^2. After the third discharge, the battery was shorted out for two hours to completely strip the zinc anodes and to remove any shunt current induced zinc deposits in the manifolds. After a 10 hour rest, the system was automatically started up and the three cycle regime repeated.

The two battery stacks tested under this test regime were both constructed with insert injection-molded carbon-plastic electrodes and the conventional Daramic/Vexar screen separator/spacer combination. However, one battery stack (C) contained a new cathode catalytic layer, PV-2, while the other stack (B) contained the standard PV-1 cathode catalytic layer. On start-up of stack C, electrolyte cross flow was evident and, based on individual cell voltage readings, a bad cell was identified. The bipolar electrode component of this bad cell was removed from the battery stack and normal behavior was observed on resumption of testing with stack C (as a 7 cell stack).

Figures IV-8 and IV-9 show the coulombic efficiency data obtained for these two batteries. Stable performance for 320+ cycles with coulombic efficiencies of 85 $\pm$ 2% has been observed with stack B. The coulombic efficiencies obtained with stack C were somewhat lower than stack B, but were generally greater than 80%. After 320 cycles, the coulombic efficiency of stack C does appear to be slowly decreasing. These results are very encouraging and the 320+ cycles obtained on these two battery stacks are the best cycle life to date at this level of zinc electrode loading. Moreover, the performance of the PV-2 layer appears to be quite satisfactory from these cycle life tests. These tests were continuing at the end of Phase II.

IV.2 Component Performance Testing

IV.2.1 High Rate Pulse Discharge Testing

Many battery applications require periods of high power discharge in addition to a continuous base load power drain. Moreover, some applications such as the electric vehicle require that the battery also accept charge

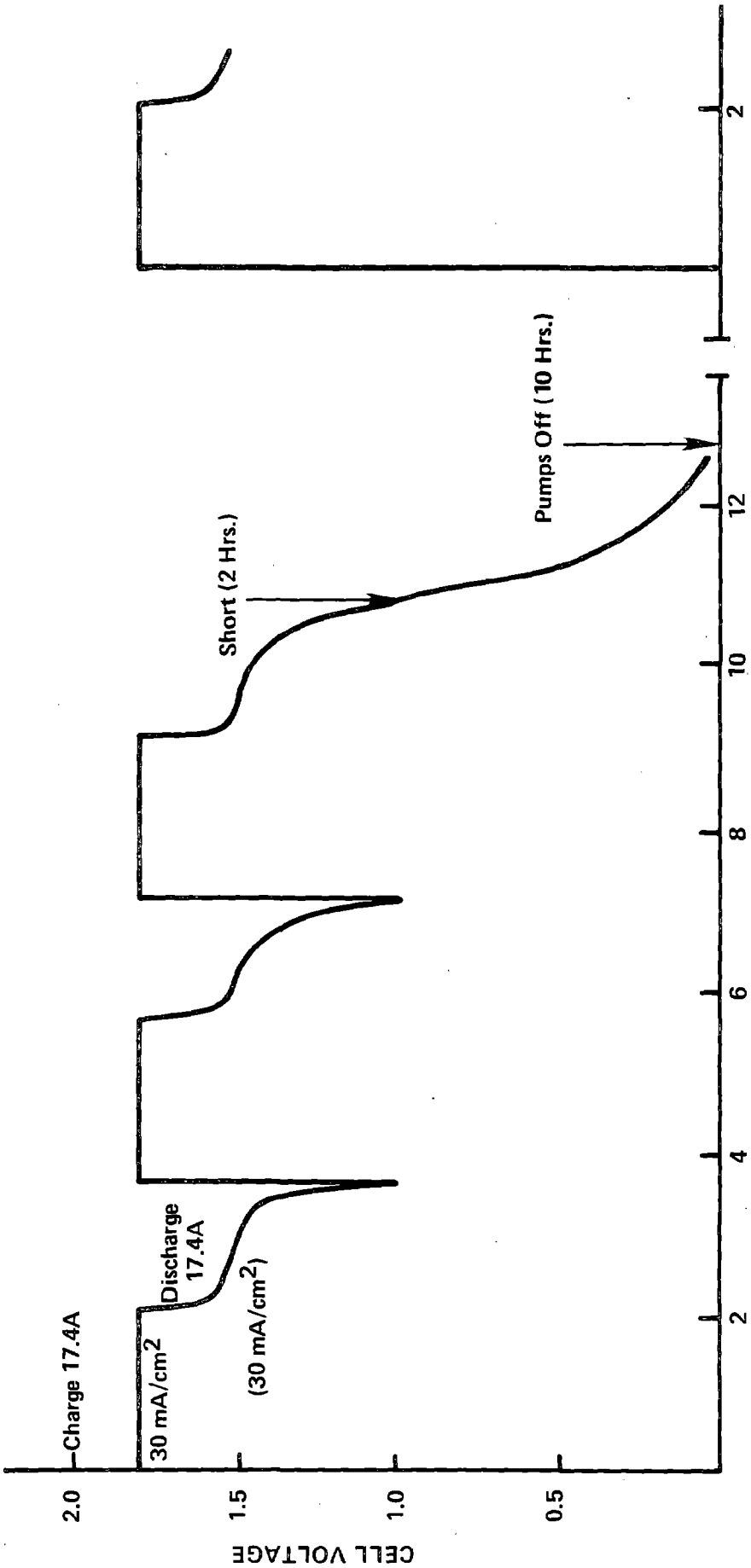

Figure IV-7 Continuous Daily Cycle Testing Regime

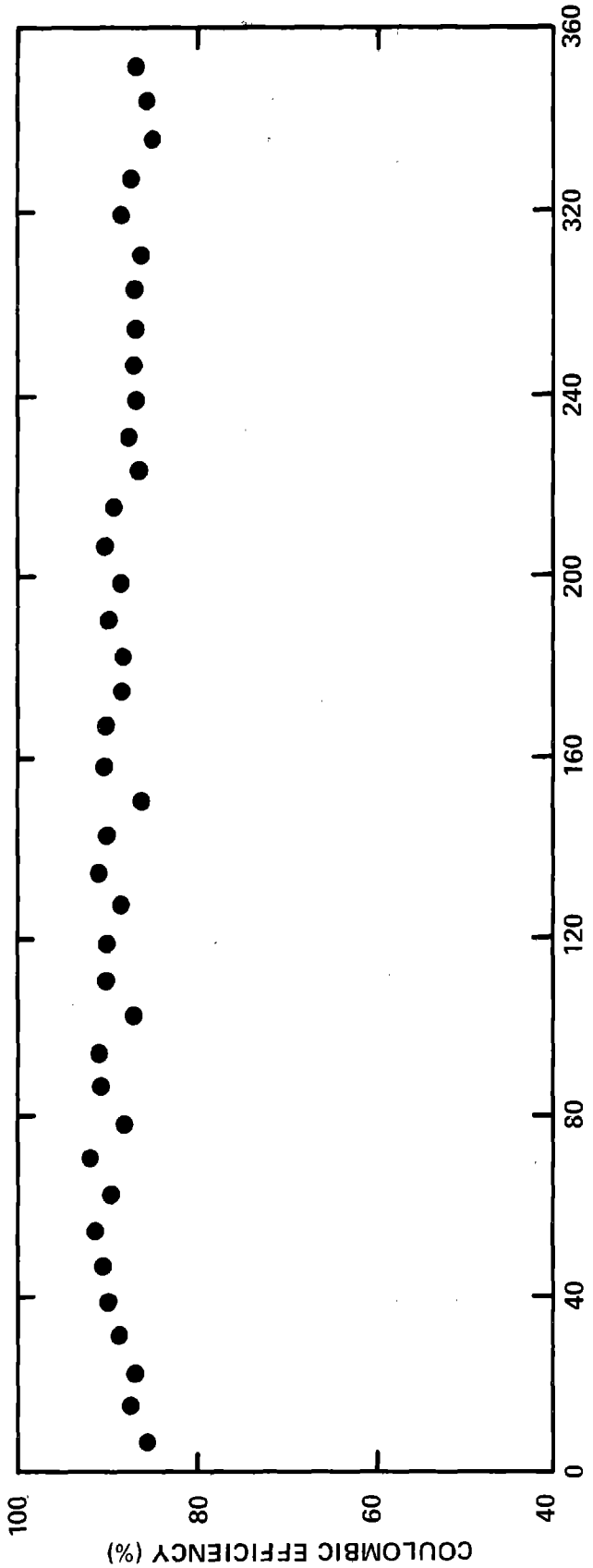

Figure IV-8 Life-Cycle Performance with Control Cathode Layer (PV-I)

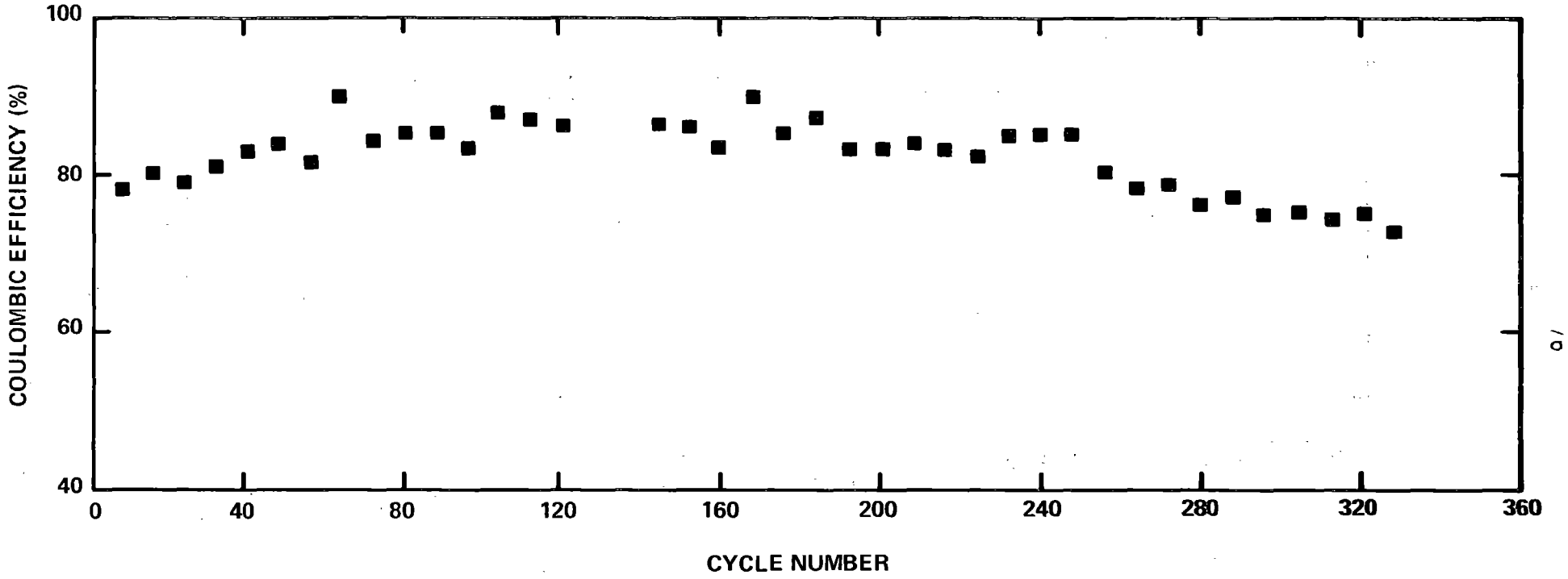

Figure IV-9 Life-Cycle Performance with Modified Cathode Layer (PV-II)

at moderately high rates corresponding to periods of regenerative braking. We have tested a four-cell zinc-bromine stack (~250 Wh) under the SAE J227aD driving cycle which involves both a high rate pulse discharge and a pulse charge period simulating regenerative braking. This particular driving cycle is being extensively used at the National Battery Test Laboratory (NBTL) to evaluate different Near-Term Battery systems for the electric vehicle application.[6]

The simplified approximation to the J227aD profile used at NBTL uses the power levels (see Figure IV-10) corresponding to the DOE/G.E./Chrysler ETV-1 vehicle which weighs 1640 kg. During acceleration from 0-45 mph, a peak power level of 23 kW is required. This peak power level is relatively modest since this vehicle uses a constant power acceleration profile ($a = a_0 e^{t}$) rather than a constant acceleration of 2.36 ft/sec^2 commonly used in J227aD driving cycle testing. (The use of this constant acceleration profile would require a peak power of 44 kW for the ETV-1 vehicle). For a projected 20-kWh zinc-bromine battery which uses two 78-cell stacks with 12 dm^2 electrode areas connected in parallel, the acceleration period of the cycle (24 sec) requires a current density of 100 mA/cm^2 or 58 A on the present 580 cm^2 components. At an average cell voltage of 1.25V or 98V for a 78 cell stack, the peak power of 23 kW (98V x 232 A) can be achieved. During the 52 second cruise portion of the cycle at 45 mph, 7.5 kW are required or a current density of 28 mA/cm^2. Regenerative braking supplies power to the battery for recharge at the 12 kW power level or 48 mA/cm^2. The range capability of the battery is designated as the point at which the 23 kW peak power demand cannot be met, i.e. when the 4 cell stack voltage drops below 5V (1.25V/cell). Each driving cycle corresponds to 0.95 miles.

It should be pointed out that this NBTL simulated driving power profile does exaggerate the effects of regenerative braking. Actual ETV-1 vehicle testing indicates that the actual amount of energy recovered during regenerative braking is closer to 15% rather than the 25% recovery calculated using the simulated profile.[7] In addition, extracting energy during the coast period of the J227aD cycle is not realistic and, therefore, the 15 kW of power may not be available for the full 16 second period.[8] Nevertheless, this standard simulated driving cycle power profile serves as a useful basis for comparison of advanced EV battery systems and may be representative of future electric vehicle designs.

Figure IV-11 shows the actual E-t trace obtained during the discharge of a 4-cell bipolar stack which had been charged to a zinc loading of 120 mAh/cm^2. The electrolyte was a 3 M $ZnBr_2$/1 M quaternary ammonium bromide solution. Since this battery is still in the developmental stage, the conventional battery terminology of "state-of-charge" (SOC) may be misleading. The battery system studied here had sufficient electrolyte (2 l of 3 M $ZnBr_2$) to provide a theoretical zinc electrode loading of 140 mAh/cm^2. While the charge input of 120 mAh/cm^2 corresponds to an electrochemical utilization of 86% of the theoretical zinc capacity of the system, it will not, in all likelihood, correspond to 86% SOC since

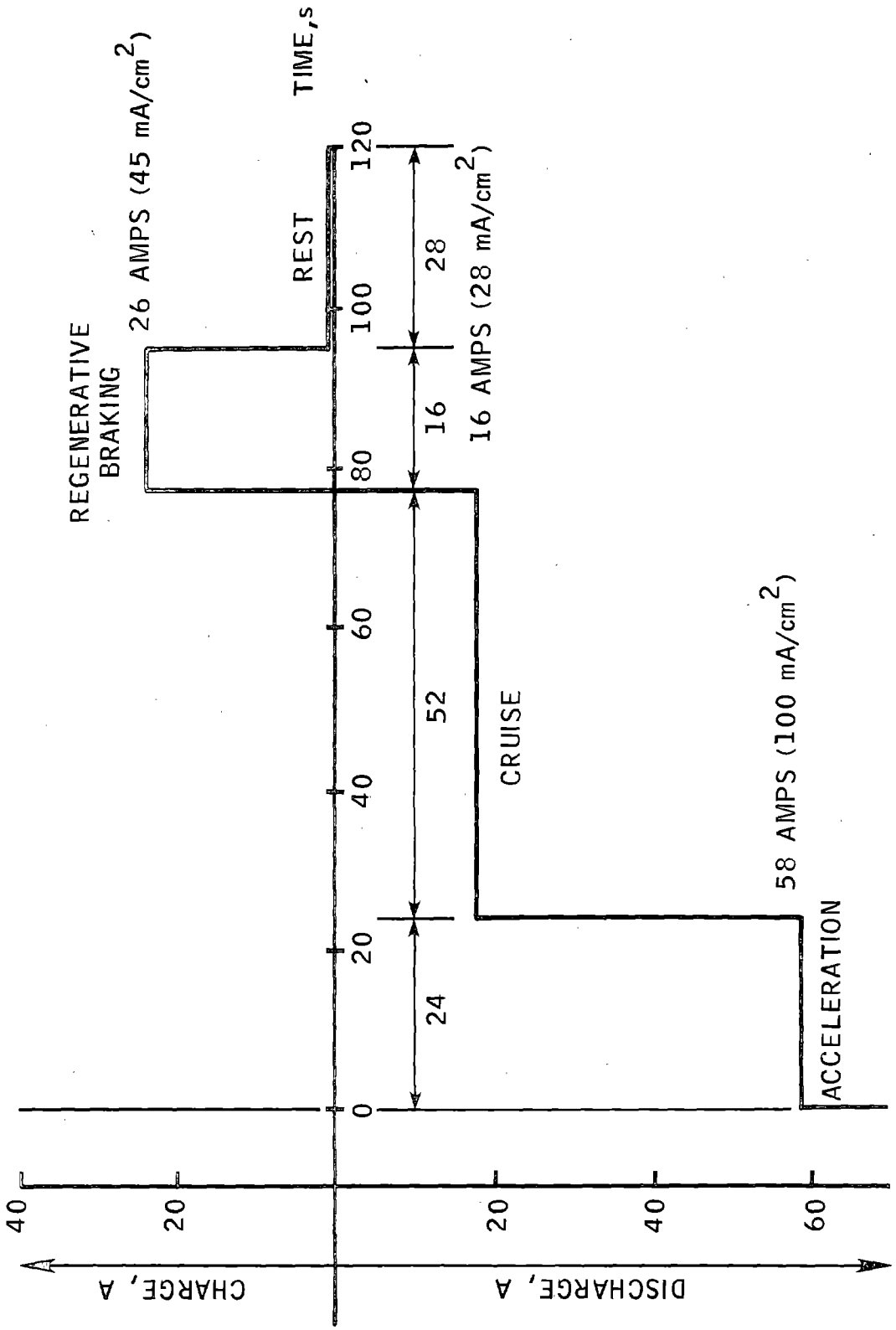

Figure IV-10 SAE J227aD Driving Cycle Approximation

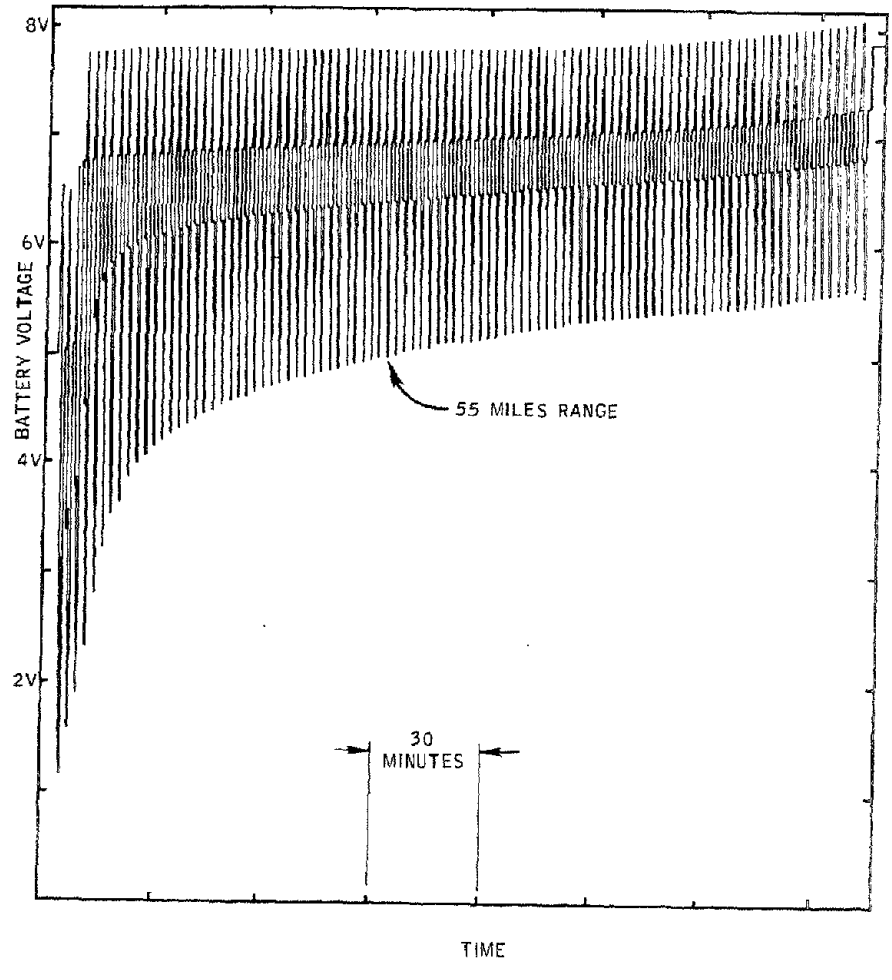

Figure IV-11 J227aD E vs t Curves for Standard Electrolyte

there is an inherent loss of capacity in a complete charge-discharge cycle to self-discharge via the parasitic zinc-bromine corrosion reaction across the microporous separator. An actual zinc-bromine EV battery system will be given a nominal capacity rating which will be based on a specified charge/discharge operating regime, e.g. C/8 charge /C/3 discharge. For example, the projected 20-kWh zinc-bromine battery system, described above, operating at 80% coulombic efficiency with a 120 mAh/cm^2 zinc loading, would be expected to actually deliver close to 27 kWh (at an average cell voltage of 1.5V). This electrochemical energy output would, of course, be reduced further by system auxiliaries.

The E-t behavior shown in Figure IV-11 shows the good response of the zinc-bromine battery stack to the J227aD cycle in the regenerative braking mode of operation. However, the J227aD cycle acceleration requirement of a cell voltage of 1.25V at the 58 A (100 mA/cm^2) discharge rate cannot be met after cycle #58 or a range of 55 miles. As the E-t curve shows, the battery stack can still operate at these discharge rates for 89 cycles or an 85 mile range if the normal 1V/cell or 4V/stack end-of-discharge voltage is used to terminate battery discharge (64% coulombic efficiency). This observation of poor power capability in electrolytes based on binary zinc bromide-quaternary ammonium bromide mixtures led us to the use of halide salts as supporting electrolytes or conductivity additives.

Potassium chloride is a generic example of such conductivity additives. The addition of 4 moles of KCl to a liter of 3 M $ZnBr_2$ 1 M quaternary ammonium bromide reduces the electrolyte resistivity from 16 ohm·cm to 7 ohm·cm. If a battery stack is charged to the 120 mAh/cm^2 level using the 4 mole KCl/l additive, a significantly improved power capability results and a 95 mile range on the J227aD cycle has been measured. Table IV-2 compares the J227aD performance with these two electrolytes at different zinc electrode loadings (90 mAh/cm^2 and 120 mAh/cm^2).

Table IV-2 shows the significant increase in power density that occurs with the more conductive, KCl-containing electrolyte. Using the 5V cut-off, the vehicle range is almost doubled in the KCl-containing electrolyte. If one allows a lower voltage cut-off of 4V (i.e. lower power), the difference is not as marked (10-20%). Coulombic efficiencies were very good for the supported electrolyte indicating a slightly beneficial effect of the additional halide anion on the aqueous phase bromine concentration. These studies indicate the basic feasibility of operating the zinc-bromine system in this pulsed charge-discharge mode and confirm the significant increase in power density afforded by the use of supported electrolytes - with no loss in coulombic efficiency.

As might be expected, a wide variety of conductivity additives exist which can provide zinc bromide electrolytes with lower resistivity than the KCl additive considered above. One of these proprietary additive mixtures had demonstrated the ability to provide electrolyte resistivity values of 4 ohm·cm while, at the same time, lowering the freezing point

TABLE IV-2

J227aD Test Results (KCl)

	STANDARD ELECTROLYTE			STANDARD ELECTROLYTE + KCl		
Qc, Ah	# of Cycles	Miles	Coulombic Efficiencies, %	# cycles	Miles	Coulombic Efficiencies, %
52.2	40 (to 5V)	38	44	76 (to 5V)	72	77
	73 (to 4V)	69	74	81 (to 4V)	77	81
69.6	58 (to 5V)	55	47	100 (to 5V)	95	76
	89 (to 4V)	85	69	105 (to 4V)	100	79
68.2*	-	-	-	68 (to 5V)	65	62
	-	-	-	75 (to 4V)	71	68

*Without Regenerative Braking

of the electrolyte. Figure IV-12 shows the E-t tracing corresponding to the J227aD cycle testing of this proprietary additive at a zinc electrode loading of 120 mA/cm^2. Ninety-four miles range is projected from this data using the J227aD cycle minimum power requirement of 1.25V/cell. When the zinc electrode loading is increased to 130 mAh/cm^2, the projected vehicle range is 100 miles. With these supported electrolytes, very little capacity remains at the end of discharge voltage of 1.25V/cell and the measured coulombic efficiencies are typically 75%, indicating good energy efficiency at these J227aD lower levels.

Table IV-3 summarizes this J227aD driving cycle data for the three electrolytes studied, including runs without regenerative braking. Based on the assumption of 100% coulombic efficiency during regenerative braking, a theoretical range improvement of 25% would be calculated. From Table IV-3, the measured range improvement of 23-24% is in excellent agreement with the theoretically predicted value. The data for the improvement in range due to regenerative braking (46%) in the KCl containing electrolyte appears anomolous and will be reanalyzed.

IV.2.2 Battery Performance with Supported Electrolytes

We have carried out constant current cycling of the four-cell stack described in Section IV.2.1 with the proprietary conductive additive which results in an electrolyte with a resistivity of 3.7 ohm·cm. Figure IV-13 shows the E-I curve for the standard 3 M Zn/Br_2/1 M quaternary ammonium bromide electrolyte and for the standard electrolyte containing the proprietary additive at a zinc loading of 90 mAh/cm^2. The calculated cell resistivity from the slope of the E-I curve is 3.4 ohm·cm for the additive containing stack vs 6.8 ohm·cm for the standard electrolyte stack. The extrapolated peak power (@ 0.9V/cell) for the additive containing stack is 216 mW/cm^2 compared to 144 mW/cm^2 for the standard electrolyte.

At a zinc electrode loading of 90 mAh/cm^2, a coulombic efficiency of 82% was measured during a cycle involving a 30 mAh/cm^2 charge and a 60 mA/cm^2 discharge rate. On increasing the zinc loading to 120 mAh/cm^2 (87% electrolyte utilization), the coulombic efficiency decreased to 74%. The measured energy efficiency was 57% at the 120 mAh/cm^2 loading and 66% at the 90 mAh/cm^2 loading. These energy efficiencies are quite good considering the fact that they were carried out essentially at the C/1.5 rate. During a cycle involving a 30 mA/cm^2 charge to 90 mAh/cm^2 and a 40 mA/cm^2 discharge, an energy efficiency of 67% was measured.

Even higher zinc electrode loadings were reached by using additional electrolyte (3 l = 203 mAh/cm^2 theoretical maximum zinc electrode loading). At 160 mAh/cm^2 (77% utilization) and 180 mAh/cm^2 (87% material utilization), the measured coulombic efficiencies were, respectively, 72% and 69%. These lower coulombic efficiencies reflect the longer total cycle times required to achieve these high zinc loadings.

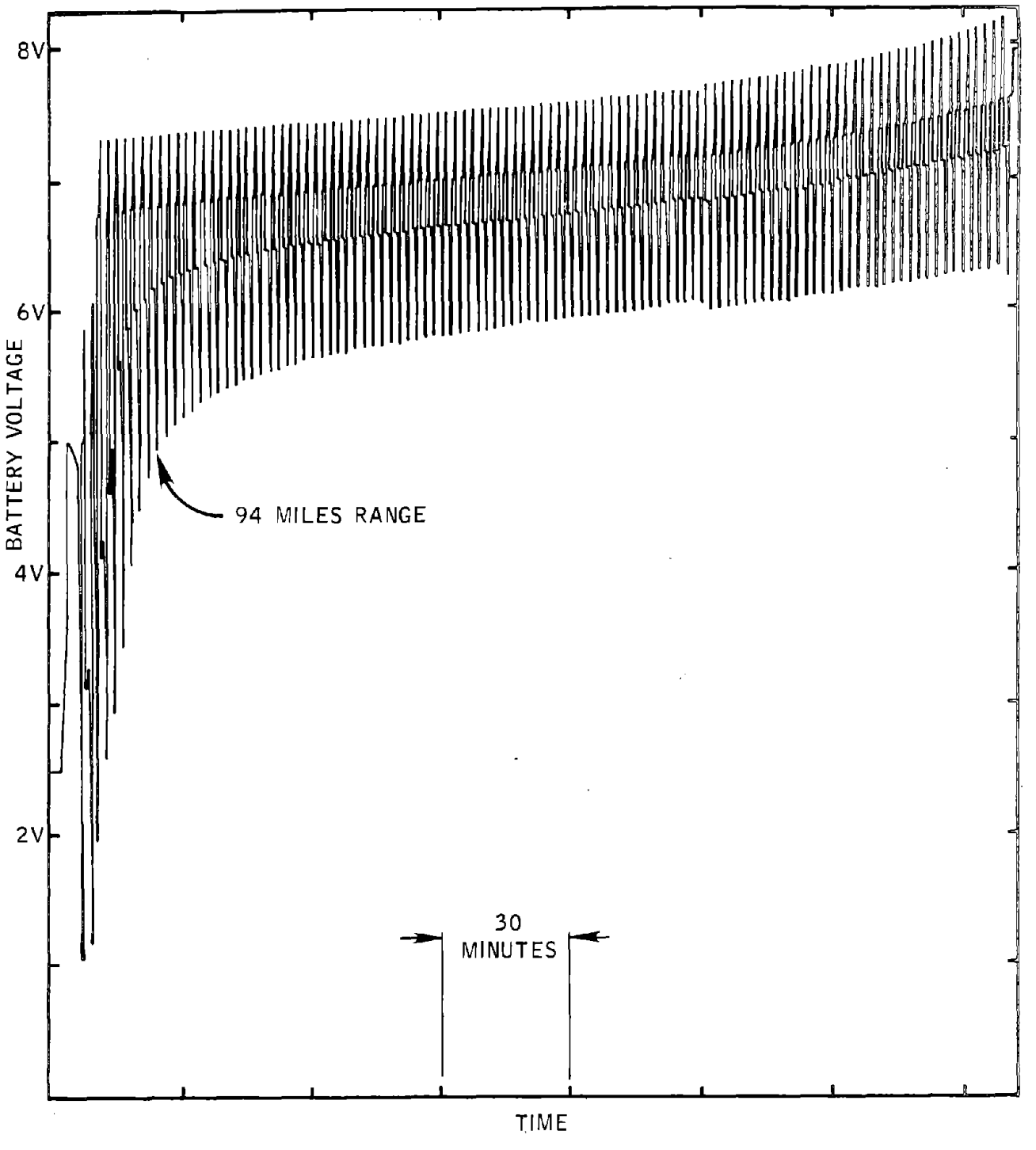

Figure IV-12 J227aD E vs t Curves for Proprietary Additive

Table IV-3 Summary of J227aD Cycle Data

	Miles Range	
	Zinc Loading 90 mAh/cm^2	Zinc Loading 120 mAh/cm^2
3M $ZnBr_2$/1M QBR	38	55
	(17)*	
3M $ZnBr_2$/1M QBr	72	95
		(65)*
3M $ZnBr_2$/1M QBr	81	94
+ Proprietary Additive		(76)*

*Without regenerative braking

During the testing of this supported electrolyte, the open circuit voltage of the battery was observed to be higher in the presence of the supporting electrolyte. The E-I data in Figure IV-13 have extrapolated OCVs of 1.84V for the supported electrolyte and 1.76V for the standard (non-supported) electrolyte. Figure IV-14 shows the E-I curves obtained as a function of battery state-of-charge (SOC). Here we define battery SOC in terms of the actual capacity delivered. For example, the data in Figure IV-14 were obtained during discharge of a battery which had been charged at 30 mA/cm^2 for 3 hours (90 mAh/cm^2). The actual discharge capacity was equivalent to 73 mAh/cm^2 (82% coulombic efficiency). The data at 45% SOC were taken after 45% or 40 mAh/cm^2 had been discharged at 40 mA/cm^2 or one hour into discharge.

Least squares analysis of the data shown in Figure IV-14 gives an empirical equation which expresses cell voltage as a function of SOC and discharge current density. This equation is:

$$E = [1.858-0.233(1-SOC)] - 3.71\ I \qquad \text{(IV-1)}$$

where

E = cell voltage

SOC = state-of-charge (100% SOC = 1.00, 10% SOC = 0.1)

I = Current density (A/cm^2)

The term in brackets in equation IV-1 expresses the dependence of OCV on state-of-charge, while the second term is essentially the IR drop in the cell at a constant internal impedence of 3.71 ohm·cm^2. Based on this equation, the calculated peak power densities (@ $E = E_{OCV} \div 2$) are 233 mW/cm^2 at 100% SOC and 188 mW/cm^2 at 20% SOC; a decrease of 20%. This OCV behavior in the presence of supporting electrolytes is distinctly different than that observed in unsupported electrolytes where the OCV is essentially independent of battery state-of-charge. The reason for this unusual behavior will be studied in the next phase of the contract.

IV.2.3 Br_2 Electrode Catalytic Layer Performance

A four-cell (250 Wh) battery constructed from co-extruded bipolar electrodes with a modified cathode catalytic layer (PV-2) and insert injection-molded Daramic separators has been tested at high discharge rates to evaluate the performance of the PV-2 layer. Figure IV-15 summarizes the data obtained as shown by E-I curves at three states-of-charge in the standard 3 M $ZnBr_2$-1 M quaternary ammonium bromide electrolyte. While the polarization curve appears to be equivalent to "standard" PV-1 containing cells at high states-of-charge, at 50% SOC the rate capability of the PV-2 layer drops significantly. This dependence of rate capability on SOC shows itself in J227aD cycle testing of this PV-2 containing stack where 76 miles range was obtained (at 120 mAh/cm^2 zinc loading) compared to the 94 mile range projected with a PV-1 containing stack under the same conditions. At normal discharge rates ($\leq$40 mA/cm^2), performance of the PV-2 layer is quite satisfactory. Under a cycle regime involving a 30 mA/cm^2 charge and discharge rate, coulombic efficiency was 81%, giving a net electrochemical energy efficiency of 64%.

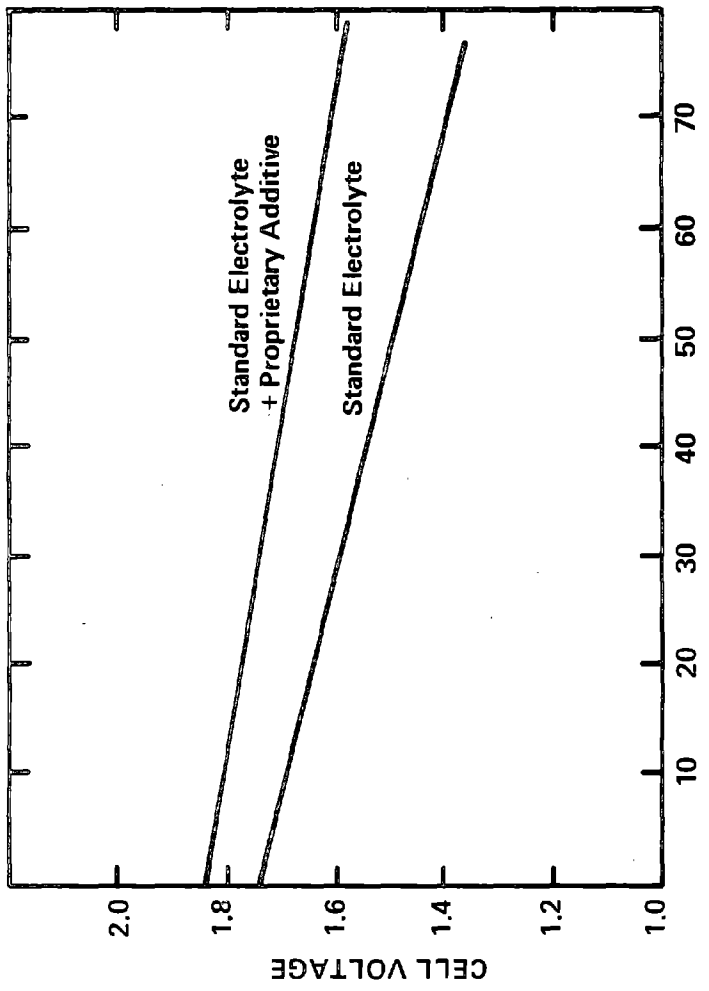

Figure IV-13 E vs I Curves for Unsupported vs Supported Electrolyte

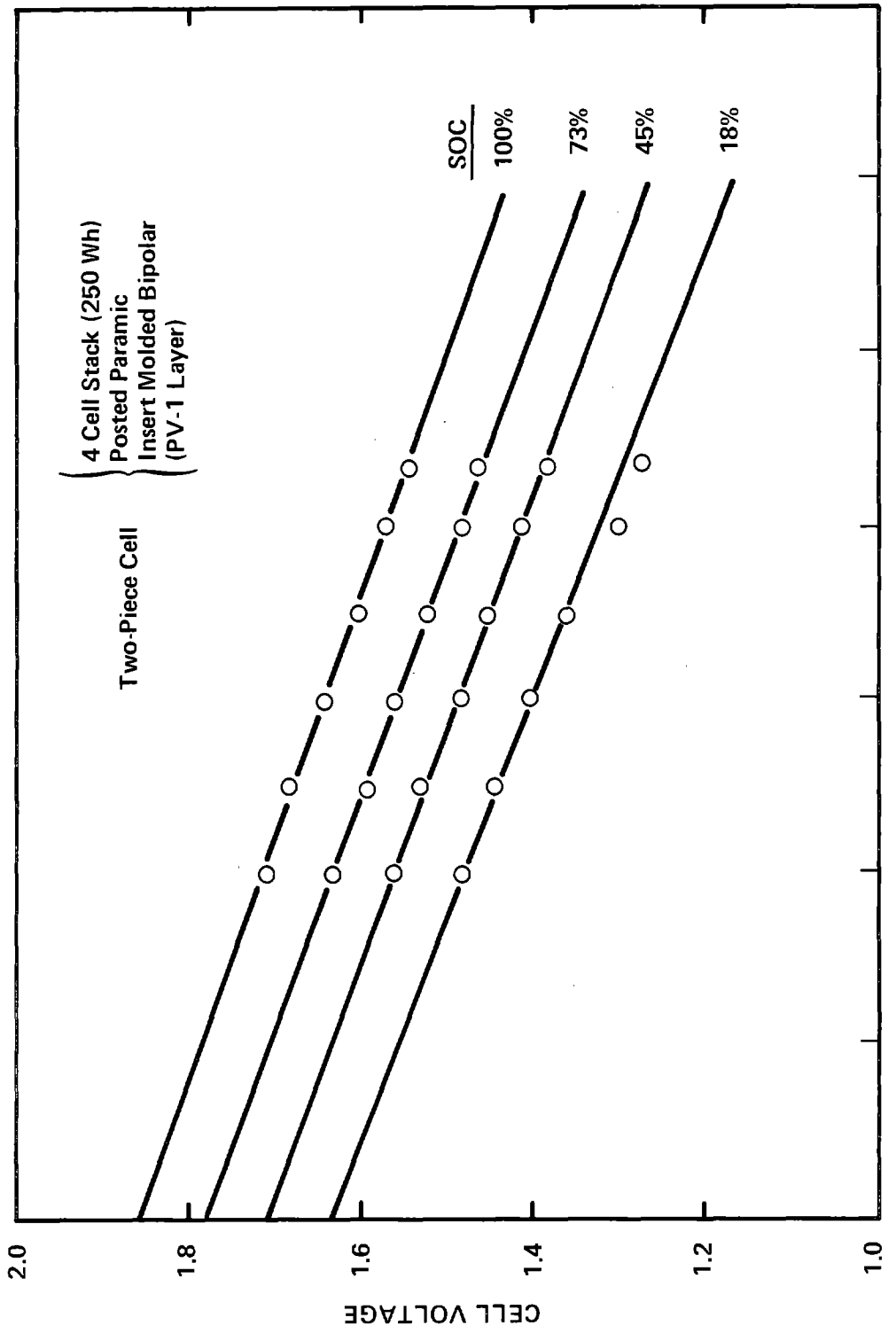

Figure IV-14 E vs I Curves as f(SOC)

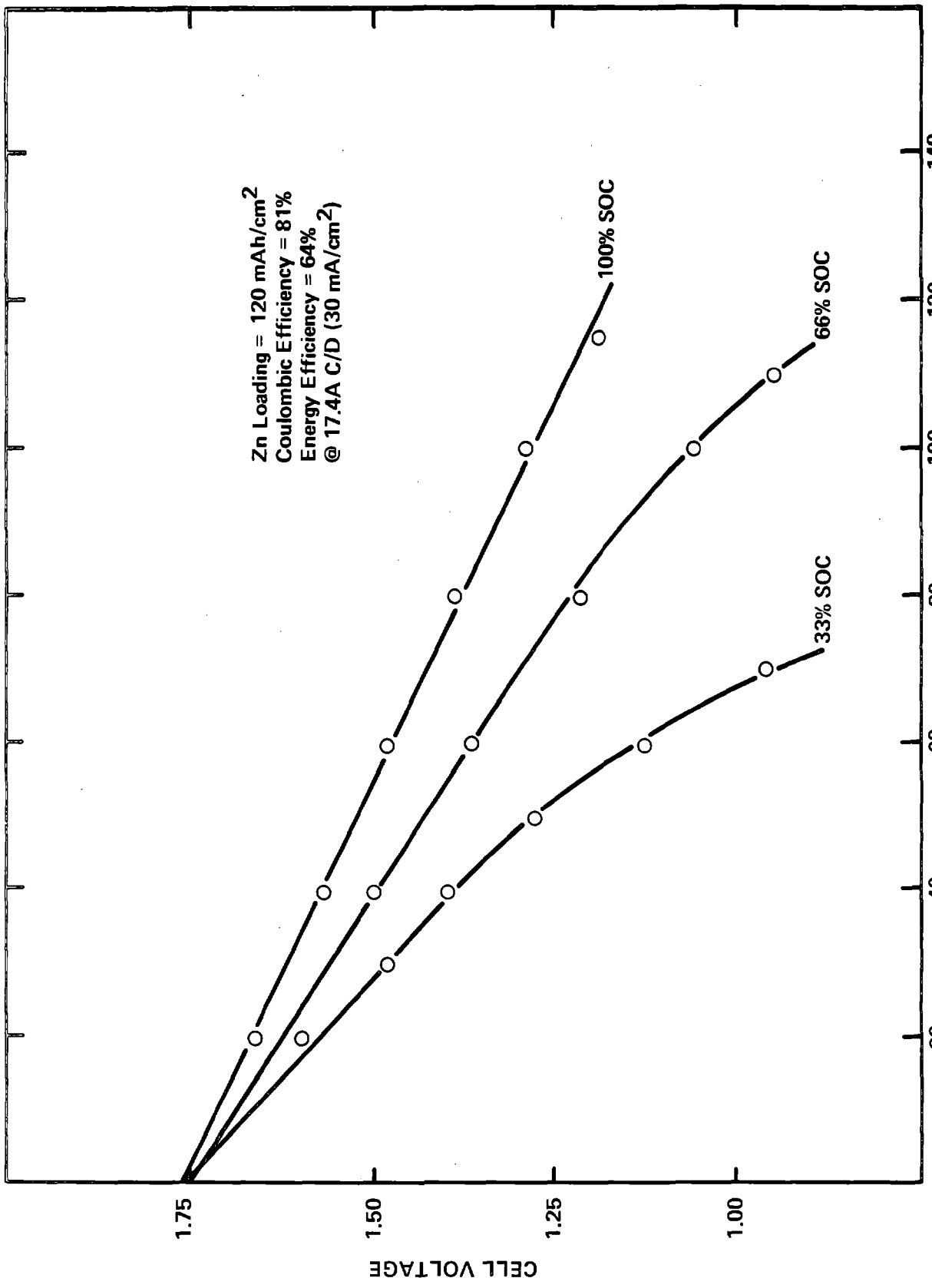

Figure IV-15 Polarization Curves at Various SOC
(2 Piece Construction with PV-2)

IV.3 Summary of Electrolyte Species Mass Balance Study

During zinc-bromine battery operation, the concentration of the various electrolyte components will vary depending on the battery state-of-charge. In order to gain a better understanding of these concentration changes, we carried out a study of the variations in electrolyte species over the course of four complete charge-discharge cycles using a 26-cell, 1.5-kWh battery stack system.

The experimental battery electrolyte phases were sampled periodically during each charge-discharge cycle and samples were analyzed for Zn^{+2}, MEM^{+}, $Q\text{-}14^{+}$, Br^{-}, and Br_2. Appendix IV describes the N^{14} NMR technique used for quaternary ammonium analysis. In addition, pH and conductivity measurements were made on all aqueous phase samples. Sampling was done under open circuit conditions and with circulating pumps off, roughly at the end of each hour of charge or discharge. A 10-15 minute period was allowed for catholyte phases to separate in the reservoir. Volumes of aqueous and oil phase catholyte and of anolyte were calculated from reservoir heights, and recorded before removing samples of the three phases (~10 ml each) for analyses. Charge and discharge portions of a cycle were carried out under constant current of 10 amps (17.2 mA/cm^2) and under constant electrolyte flow of 3.8 l/min. Charging was continued until coulombs equivalent to approximately 70% of the available Zn^{+2} were passed (5 hours). Discharge was carried out at 10 amps until stack voltage dropped to 1V/cell or 26 volts (~3.5 hours). Two conditions were varied over the four cycles. These pertain to: (1) a valve connecting the anolyte and catholyte reservoirs; and (2) a polyelectrolyte additive (Versa) When the valve connecting the two reservoirs is open, extreme volume differences due to transfer of solvent through the membranes are avoided by allowing flow from the reservoir in which the fluid height exceeds the transfer valve height. The polyelectrolyte is added to the extent of 0.10-0.15% w/o of total electrolyte to impart some ion selectivity to the Daramic porous membrane separators, and thus reduce self-discharge. These factors were varied over the four cycles as follows, namely:

Run 8112-76 - transfer valve open, no polyelectrolyte added
Run 8112-77 - transfer valve closed, no polyelectrolyte added
Run 8112-78 - transfer valve closed, polyelectrolyte added
Run 8112-79 - transfer valve open, polyelectrolyte added

For the four cycles used to obtain mass balance data, overall coulombic efficiencies, defined as follows:

$$\text{C.E.} = \frac{\text{hours at 10 amps discharge to one volt/cell}}{\text{hours at 10 amps charge}} \times 100,$$

are given in Table IV.4.

Table IV-4

Coulombic Efficiency During Mass Balance Testing

Run #	Coulombic Efficiency, %
8112-76	67.5
8112-77	68.3
8112-78	68.6
8112-79	70.8

The values range from 67.5% - 70.8%, and there appears to be a slight improvement on addition of the polyelectrolyte to the electrolyte.

Another measure of coulombic efficiency in the zinc-bromine battery is the ratio of zinc equivalents removed from the electrolyte per unit time of charge to the number of coulombic equivalents passed. These coulombic efficiency values were readily obtainable from mass balance run data, and are presented in Table IV.5 as functions of state-of-charge for each of the four runs. The data (Table IV.5) show a small increase in coulombic efficiency when the polyelectrolyte is added to the electrolyte, regardless of the position of the reservoir transfer valve. This is an anticipated result, since the purpose of the polyelectrolyte addition is to retard the transfer of Br_3^- through the separators, and thus reduce self-discharge at the anodes. A suprising conclusion that may be drawn from the data in Table IV.5 is that coulombic efficiencies, as determined by zinc analyses, are significantly higher when the reservoir transfer valve is closed, regardless of the presence or absence of the polyelectrolyte. Indeed, as shown by Figure IV-16 the shapes of the coulombic efficiency (vs charge time) curves are drastically different (particularly during the first hour of charge) depending on the position of the transfer valve. We observed no transfer of fluid during the first hour of charge when the valve was open. In fact, the greatest reservoir volume changes occurred in the runs in which the valve was closed. In these runs, the total catholyte reservoir volume increased by 800-1000 ml (with a corresponding decrease in anolyte reservoir volume) as a function of time of charge.

The results obtained for species analyses, pH measurements, and resistivity measurements on electrolyte samples taken over a given charge-discharge cycle, were reduced to graphical form for each of the four runs. Only in the case of aqueous zinc ion content did these show any significant dependency on the position of the reservoir transfer valve, or on the presence or absence of the polyelectrolyte. For the sake of brevity, only graphs representing the results obtained over a single charge-discharge cycle are presented. These are shown in Figures IV-17 to IV-23.

Table IV-5

Coulombic Efficiency based on Zinc Analysis

Run #8122-76

Valve Open No Versa

S.O.C.	Zinc Coulombic Efficiency (%)
0.0	0.0
14.3	29.5
28.6	64.3
42.9	73.7
57.1	78.3
71.4	76.4

Run #8112-79

Valve Open W/Versa

S.O.C.	Zinc Coulombic Efficiency (%)
0.0	0.0
14.4	36.1
28.8	68.9
43.2	84.0
57.6	83.0
75.7	85.9

Run #8112-77

Valve Closed No Versa

S.O.C.	Zinc Coulombic Efficiency (%)
0.0	0.0
15.0	88.2
30.0	77.9
45.0	82.3
60.1	82.4
78.5	72.8

Run #8112-78

Valve Closed W/Versa

S.O.C.	Zinc Coulombic Efficiency (%)
0.0	0.0
14.3	98.6
28.7	85.8
43.0	88.5
57.4	80.6
75.0	84.1

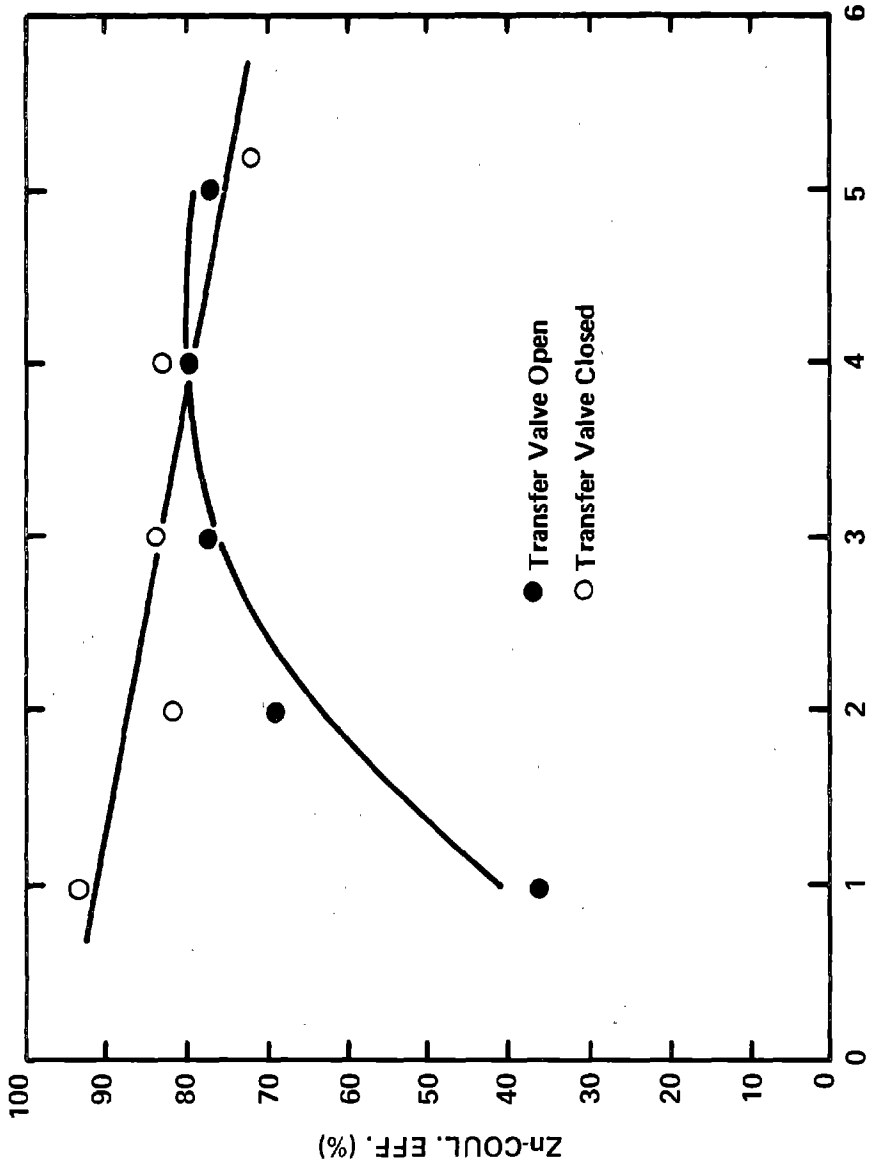

Figure IV-16 Zinc Coulombic Efficiency

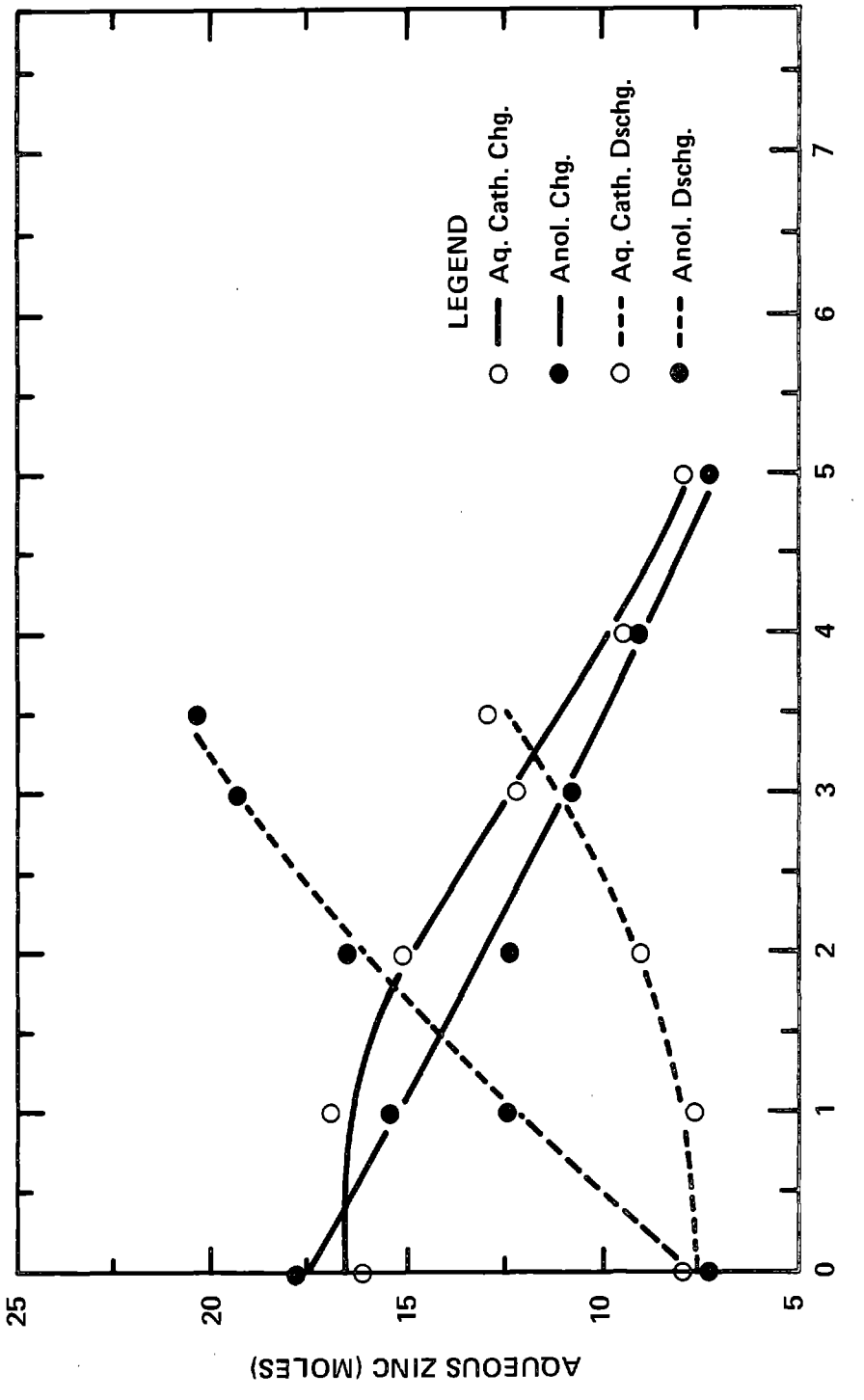

Figure IV-17 Zinc Ion Behavior

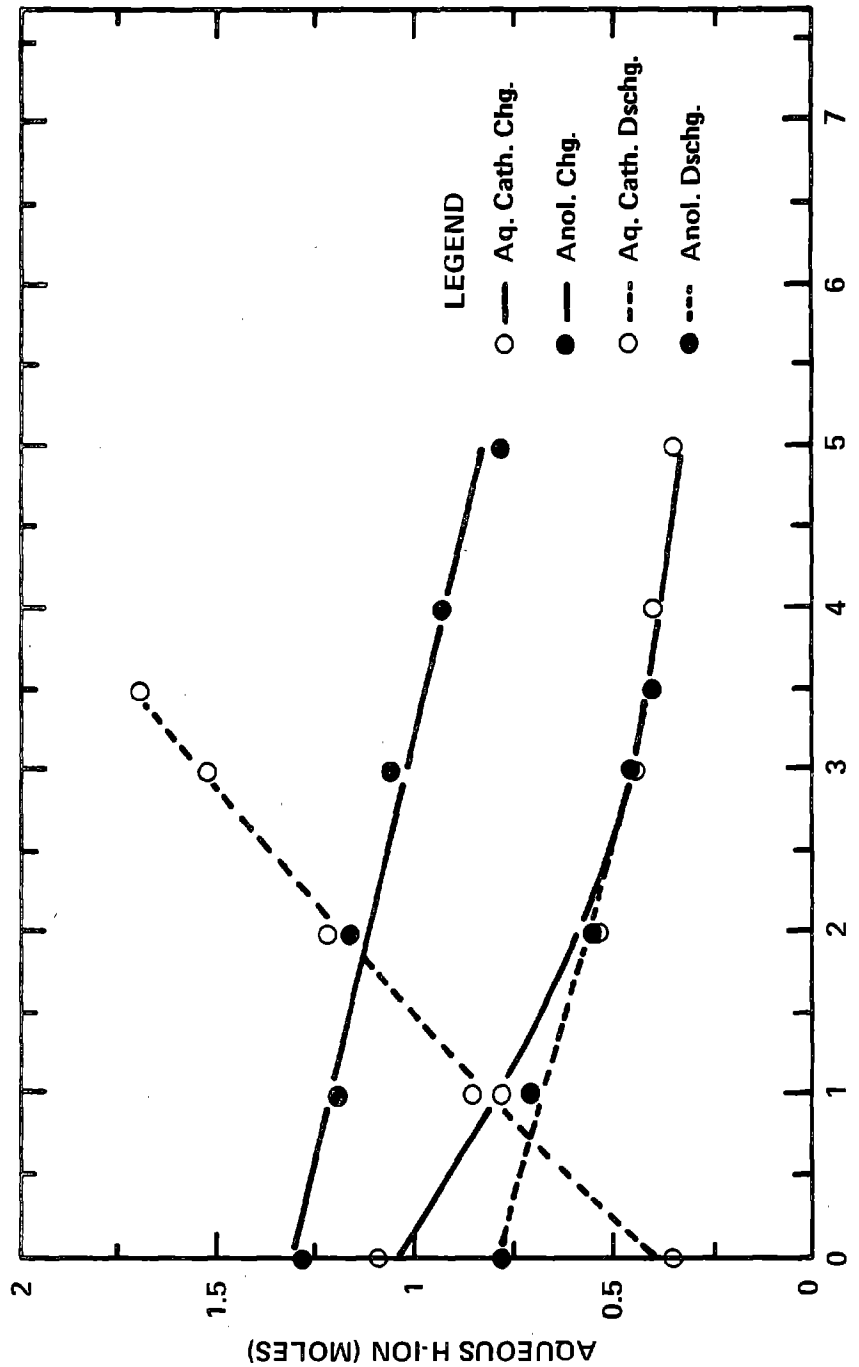

Figure IV-18 Hydrogen Ion Behavior

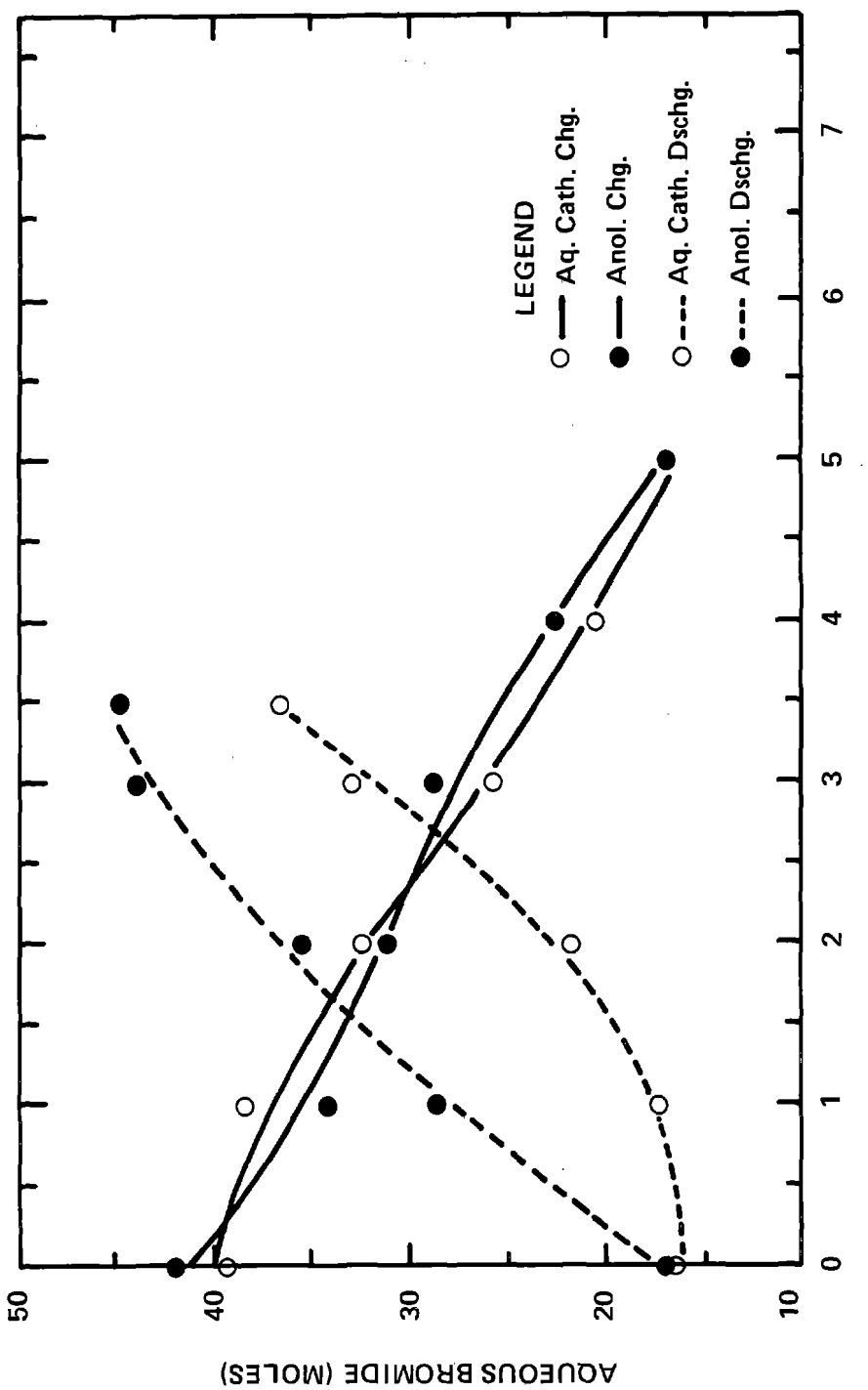

Figure IV-19 Bromide Ion Behavior

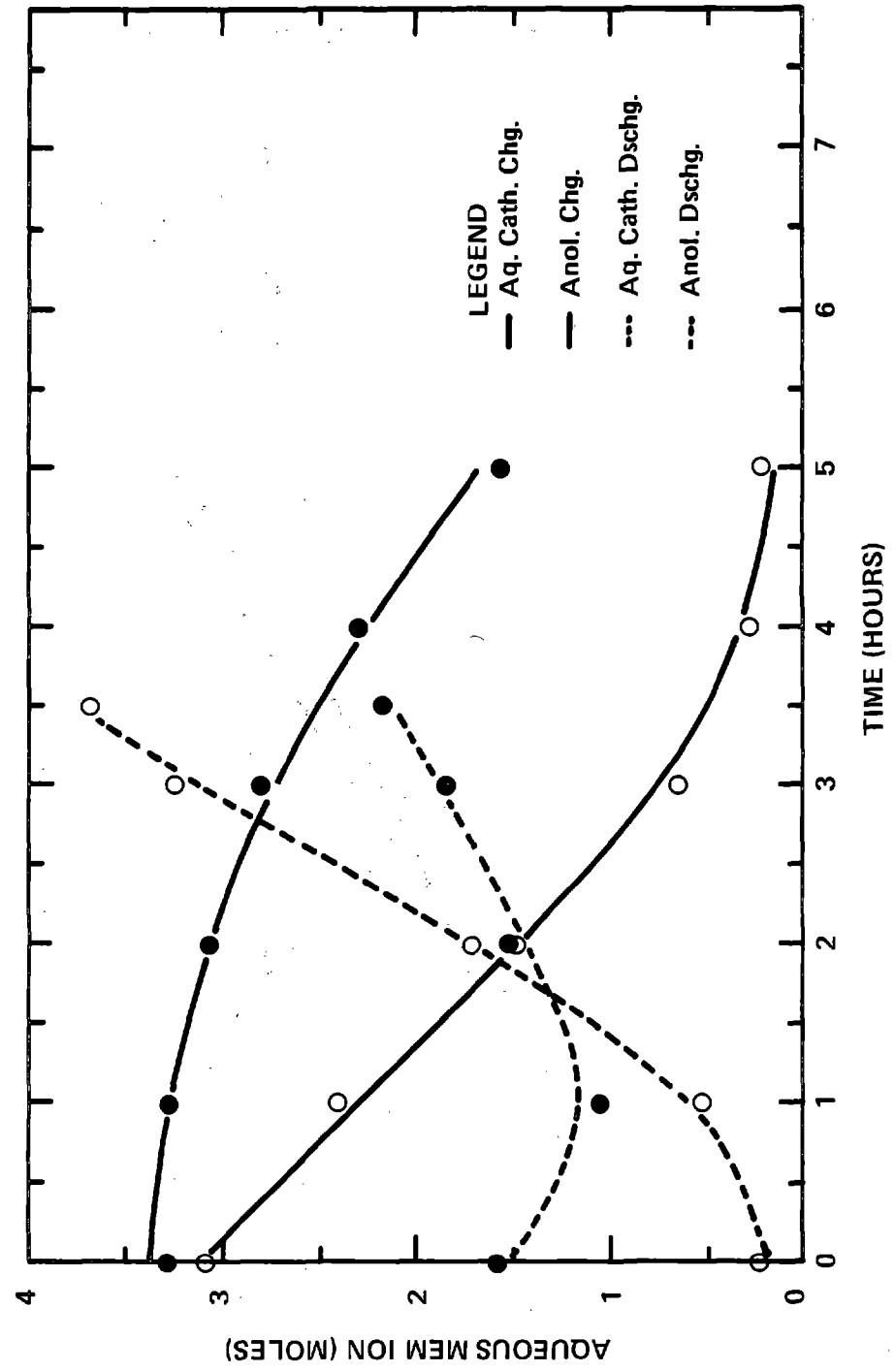

Figure IV-20 MEM^{+} Ion Behavior

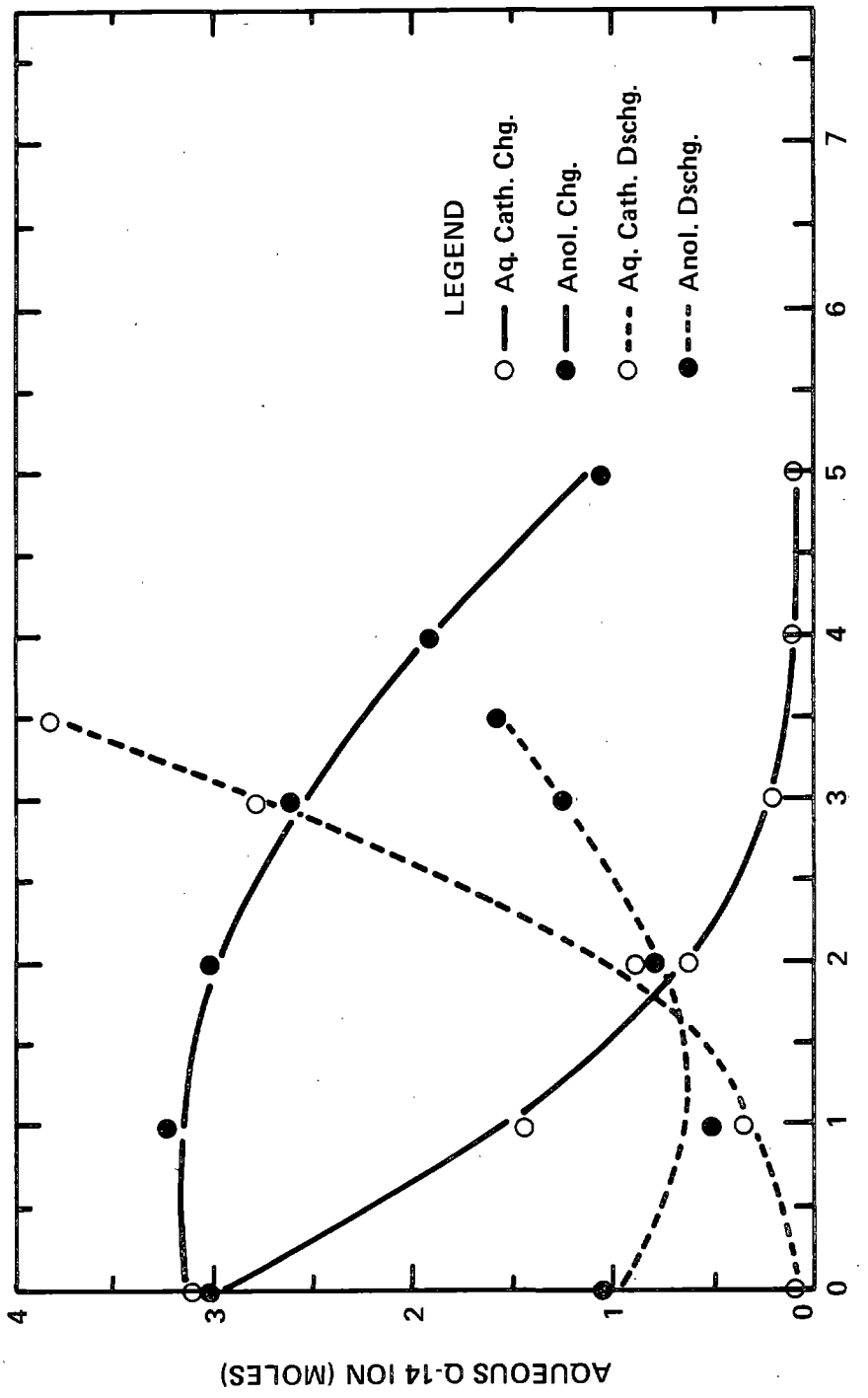

Figure IV-21 Q-14^{+} Ion Behavior

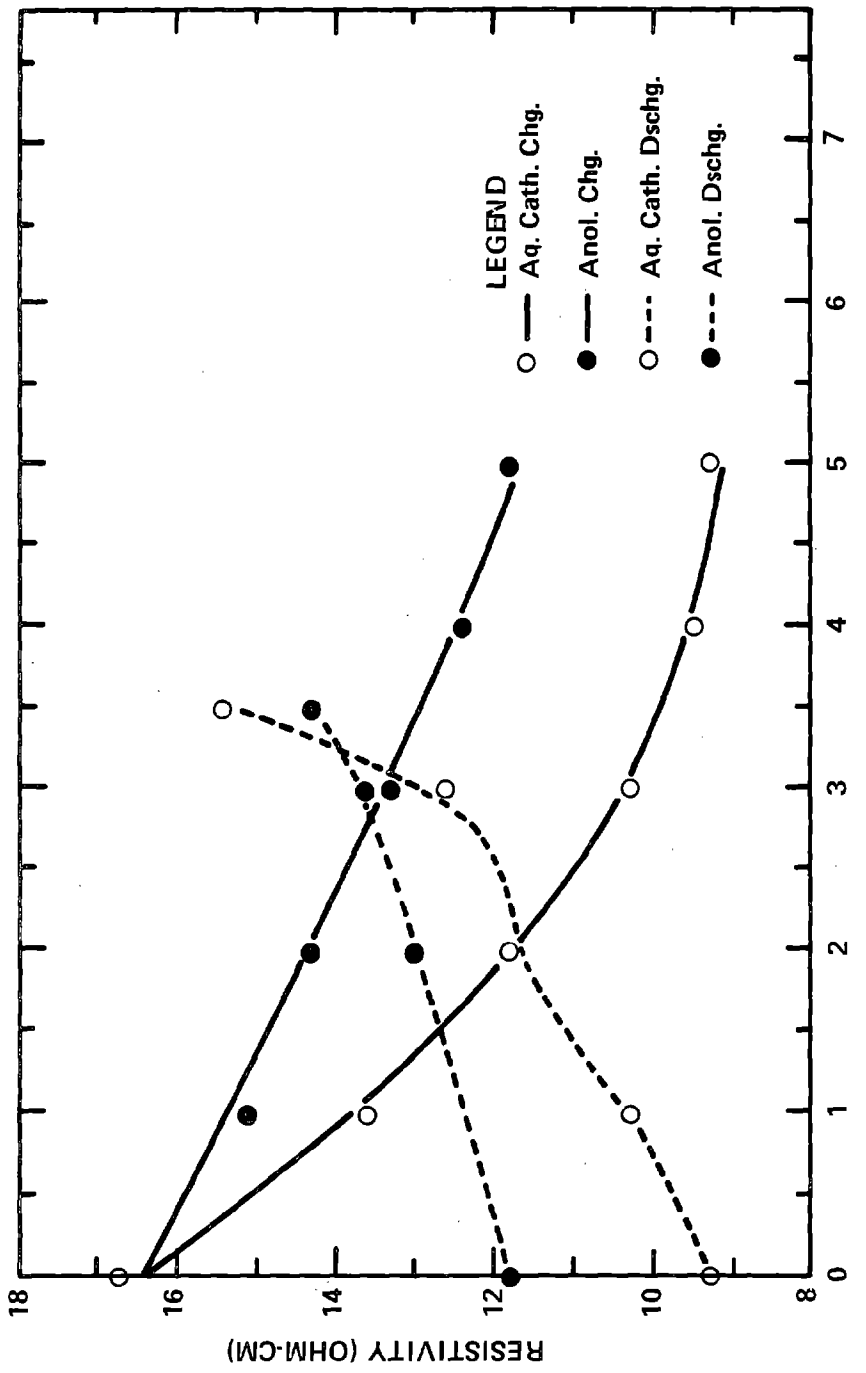

Figure IV-22 Electrolyte Resistivity Changes

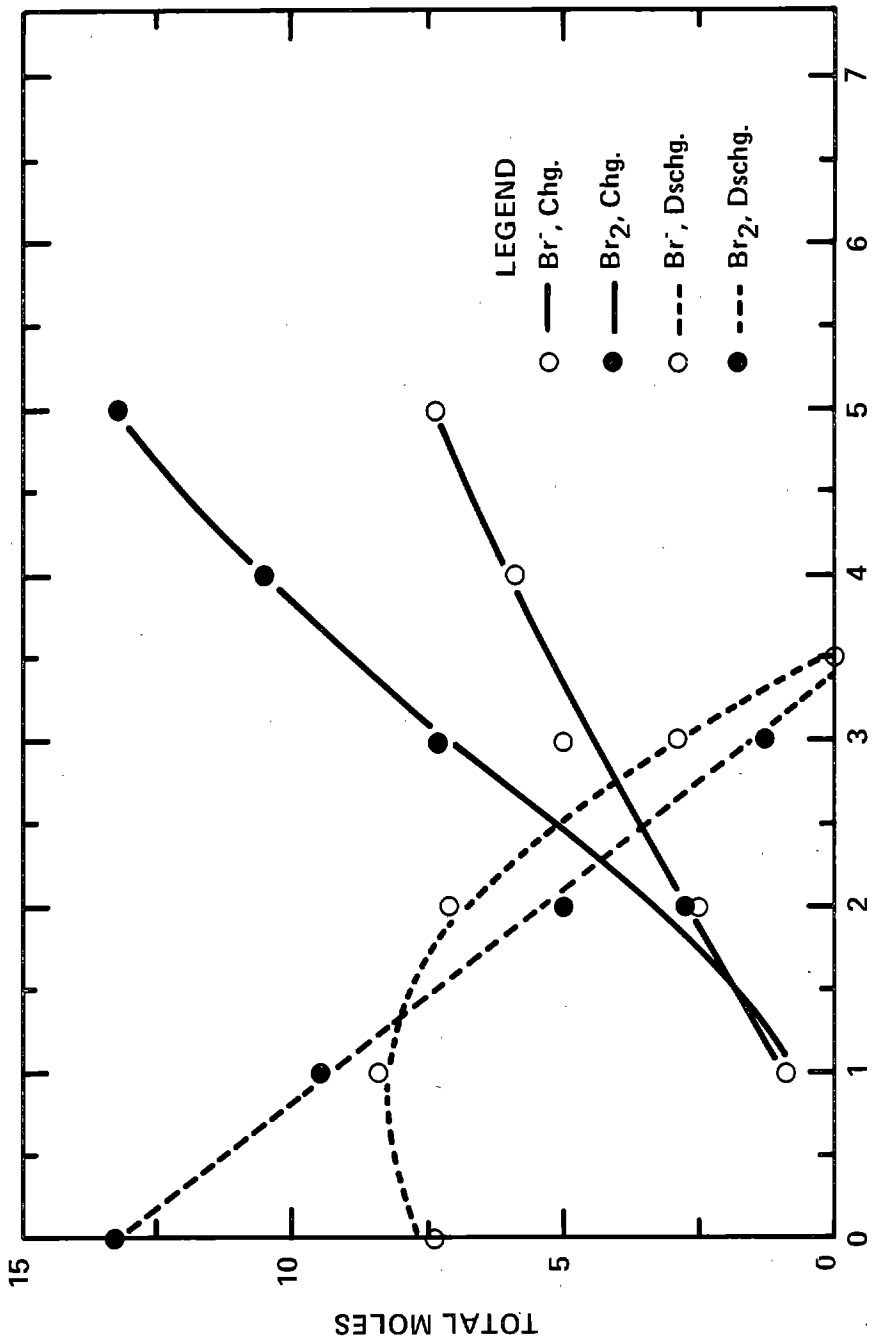

Figure IV-23 Catholyte Oil Behavior

On plotting electrolyte zinc contents (Figure IV-17) as functions of time of charge (discharge), one observes an increase in catholyte Zn^{+2} over the first hour of charge in those runs in which the transfer valve was open (8112-76, 8112-79). This behavior is undoubtedly related to the difference in the shape of the coulombic efficiency curves (based on electrolyte zinc content) for the same runs, as discussed earlier. In general, Zn^{+2} content decreases on charge (Figure IV-17 solid curves), and increases on discharge (dashed curves) more rapidly in the anolyte than in the catholyte, as expected. At the end of discharge, the zinc content of the anolyte is nearly twice that of the catholyte.

The hydrogen ion content (Figure IV-18) of both anolyte and catholyte decrease as zinc ions are removed from the electrolyte during the charging process. On discharge (Figure IV-18, dashed curves) the process reverses itself in the catholyte, but the anolyte hydrogen ion content continues to decrease linearly. Rationalization of this behavior requires detailed analysis of hydrogen ion activity in the system, $ZnBr_2$-HBr-H_2O. This is not presently understood.

The behavior of bromide and quaternary ammonium ions in the aqueous electrolyte phases on charge-discharge cycling are shown in Figures IV-19, IV-20 and IV-21. It is evident from the charge curves of Figures IV-20 and IV-21 that the Q-14 salt complexes somewhat more rapidly with bromine than the morpholinium salt (MEMBr).

The resistivity of dilute aqueous zinc bromide decreases with increasing concentration, goes through a minimum and then increases with further increasing zinc bromide concentration. At approximately 3 molar $ZnBr_2$, our initial electrolyte lies on the high concentration side of the minimum in the aqueous $ZnBr_2$ resistivity-concentration curve. Accordingly, during the charge portion of the cycle, the resistivities of both anolyte and catholyte decrease due to lowering of zinc bromide concentrations (Figure IV-22). The fact that the resistivity of catholyte decreases much more rapidly on charge than that of the anolyte, may be correlated with disappearance of bulky quaternary ammonium ions due to complexation with bromine. On discharge (Figure IV-22, dashed curves), the resistivities increase toward their initial values (15-18 ohm·cm).

The final figure in this series (Figure IV-23) shows how the catholyte oil composition varies over one charge-discharge cycle. Total moles of bromine are represented by filled circles and total moles of bromide by open circles, on both charge (solid curves) and discharge (dashed curves). During the early stages of complex formation, the bromine and bromide contents are nearly equal ($QNBr_3$). At the end of charge, the bromine content is approximately twice that of bromide ($QNBr_5$).

The fates of the various electrolyte species over the four cycle mass balance study are summarized by Figures IV-24 and IV-25. At the end of each charge-discharge cycle, the battery was short circuited

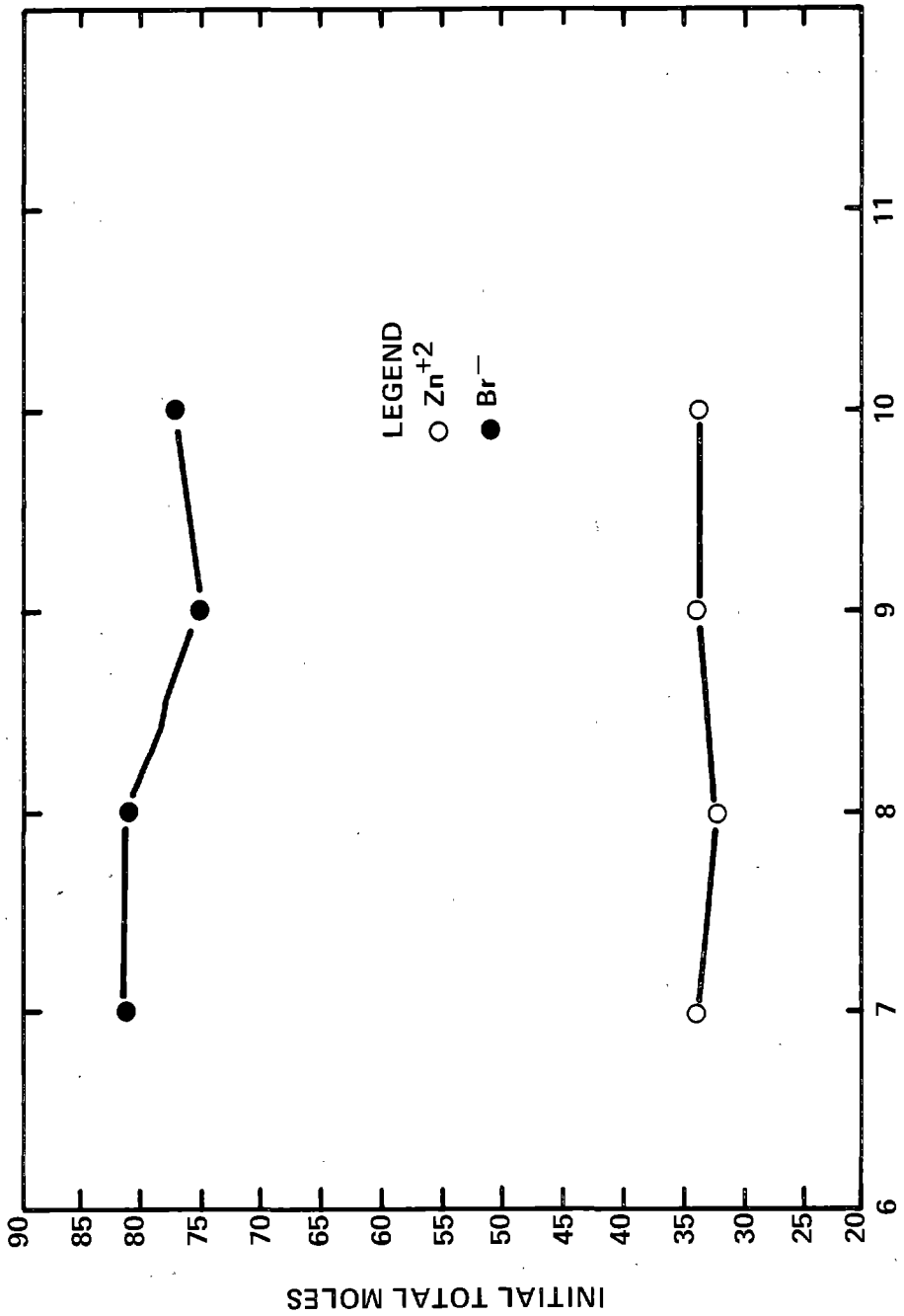

Figure IV-24 Zn^{++}/Br^{-} vs Cycle Number

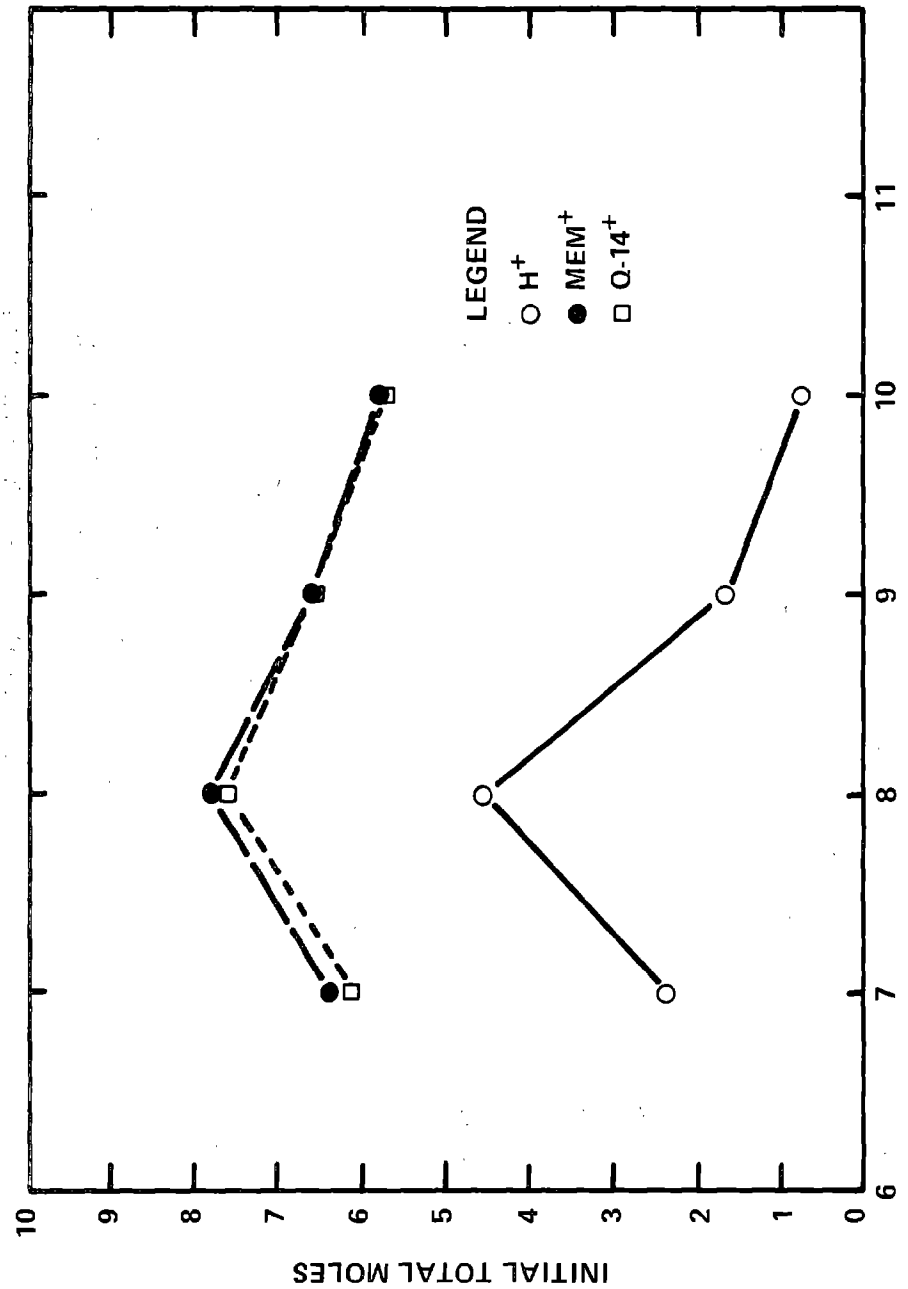

Figure IV-25 $H^+/MEM^+/Q\text{-}14^+$ vs Cycle Number

to dissolve remaining anodic zinc (and cathodic bromine complex). The electrolyte was then circulated for 1-2 hours under open circuit conditions in order (to the extent possible) to equalize the concentrations of species in the catholyte and anolyte fluids, before recharging the battery.

As shown in Figure IV-24, the zinc content of the electrolyte remained virtually constant over the four charge-discharge cycles of this study. There are slight decreases in bromide (Figure IV-24) and quaternary ammonium (Figure IV-25) ions over the four cycles. This opens up the possibility of significant loss of bromine complexing agents by some, as yet unknown, mechanism after a very large number of cycles. The validity of this observation should be investigated further now that we have a rapid method of analysis for quaternary ammonium ions. The very definite decrease in hydrogen ion content (Figure IV-25) over the four cycles is undoubtedly due to H_2 evolution, which is observed during operation of zinc-bromine batteries. The upward excursions of hydrogen ion and quaternary ammonium ion contents at the beginning of cycle #8 (Figure IV-25) are probably due to analyses of non-representative samples.

IV.4 Evaluation of Electrolyte Additives

Eventual application of Exxon's zinc-bromine battery to vehicular propulsion will require achievement of high power density levels, and demonstration of an ability to operate the battery within a wide range of ambient temperatures. These requirements relate to the conductivity and liquid range of our "standard" electrolyte as a function of state-of-charge. We have looked at electrolyte additives with the intent of favorably modifying these properties. This area of study is aimed at achieving the goal of a high conductivity, wide liquid range electrolyte for the zinc-bromine battery. The results obtained to date are discussed below.

The present "standard" electrolyte composition, prior to charging, consists of the following:

> 3M zinc bromide, 0.5M N-methyl, N-ethylmorpholinium bromide (MEMBr), 0.5M Q-14 Br, plus sufficient HBr to adjust the pH to the range 2-3. This "standard" composition has a resistivity of 18 ohm·cm and a freezing point of -28°C (-18°F).

We have measured freezing points and resistivities of compositions estimated to simulate 50% and 70% state-of-charge electrolyte composition. The results of these measurements are shown in Table IV-6.

Table IV-6

Electrolyte Freezing Points and Resistivity as f(SOC) (Simulated)

State-of-Charge* (%)	Composition	Freezing Point (°C)	Resistivity (ohm·cm)
0	3M $ZnBr_2$, 1M QN^+	-28	18
50	1.5M $ZnBr_2$, 0.5M-QN^+	-17	13
70	0.9M $ZnBr_2$, 0.1M-QN^+	-10	10

*SOC = $\frac{\text{Coulombic Equivalents Passed}}{\text{Initial Total } Zn^{+2} \text{ Equivalents}} \times 100$

Shortly after having made measurements on simulated electrolytes, we carried out material balance studies on an actual battery electrolyte during charge-discharge cycling (Section IV.3.3). Periodic analyses of aqueous samples during cycling gave the results summarized in Table IV-7.

Table IV-7

Electrolyte Freezing Points and Resistivity as f(SOC) (Actual)

State-of-Charge	Aqueous Catholyte			Anolyte		
(%)	Zn^{+2} (m/l)	QN^+(Total) (m/l)	Res. (ohm cm)	Zn^{+2} (m/l)	QN^+(Total) (m/l)	Res. (ohm cm)
0	2.56	0.98	16.7	2.66	0.94	16.7
50	2.16	0.13	9.7	1.50	0.73	12.8
70	1.79	0.075	9.3	1.14	0.42	11.8

Comparison of the compositions shown in Tables IV-6 and IV-7 shows that the simulated electrolyte concentrations agree fairly well with measured anolyte compositions, so that the range of measured freezing points (-28 to -10°C) and resistivities (10-18 ohm·cm) obtained for the simulated electrolytes are roughly valid for an operating battery electrolyte.

Some measured values of freezing points and resistivities obtained on addition of non-discharging ions to simulated electrolyte compositions are shown in Figure IV-26. The resistivity-lowering effects of added monovalent metal chlorides to "standard" zero percent state-of-charge electrolyte are shown in Figure IV-26. It appears that on a molar basis, resistivity decreases more rapidly with increasing size of added cation.

Resistivities (Figure IV-27) and freezing points (Figure IV-28) of simulated electrolyte compositions containing a mixture of monovalent (KCl) and divalent cations ($CaCl_2$) as supporting electrolyte show that monovalent additives are more effective in lowering resistivity (Figure IV-27), while divalent additives are more effective in lowering freezing point.

In general, "test tube" freezing point determinations on electrolyte mixtures showed a tendency for additives to totally redissolve at significantly higher temperatures than the observed freezing points on the cooling portion of a freezing-melting cycle. This apparent slow rate of redissolution of electrolyte additives will have to be studied further under flow conditions in an actual battery. In addition, we need to examine the flow properties of the non-aqueous catholyte complexes at low temperatures. We have mounted a four cell battery in an environmental chamber in which temperatures down to -50°C can be obtained. The practical operating temperature range of this battery as a function of electrolyte composition will be studied in Phase III.

IV.5 Properties of Bromine Complexes

As stated in section IV-4, we need to get data on the low (and elevated) temperature properties of nonaqueous catholyte complexes as functions of composition in order to define practical operating temperature ranges. During Phase II, we obtained data on the properties of MEMBr-Br_2 complexes as a function of composition.

Figure IV-29 shows Br_2 vapor pressures over MEMBr-Br_2 compositions. These data were obtained by an optical method using the visible Br_2 absorption peak at 460 nm. In our recently completed mass balance study of the zinc-bromine battery (Section IV.3), a plot of catholyte oil Br_2 and Br^- ratio of 2 after five hours of charge. This corresponds to the composition $QNBr_5$, which (if QN were MEM) would have a vapor pressure of approximately 3mm mercury.

Similarly, Table IV-8 shows measured boiling ranges (with decomposition) of some MEMBr-Br_2 complexes. As expected, the boiling ranges approach the boiling point of Br_2 (60°C) as the bromine content of the complex is increased.

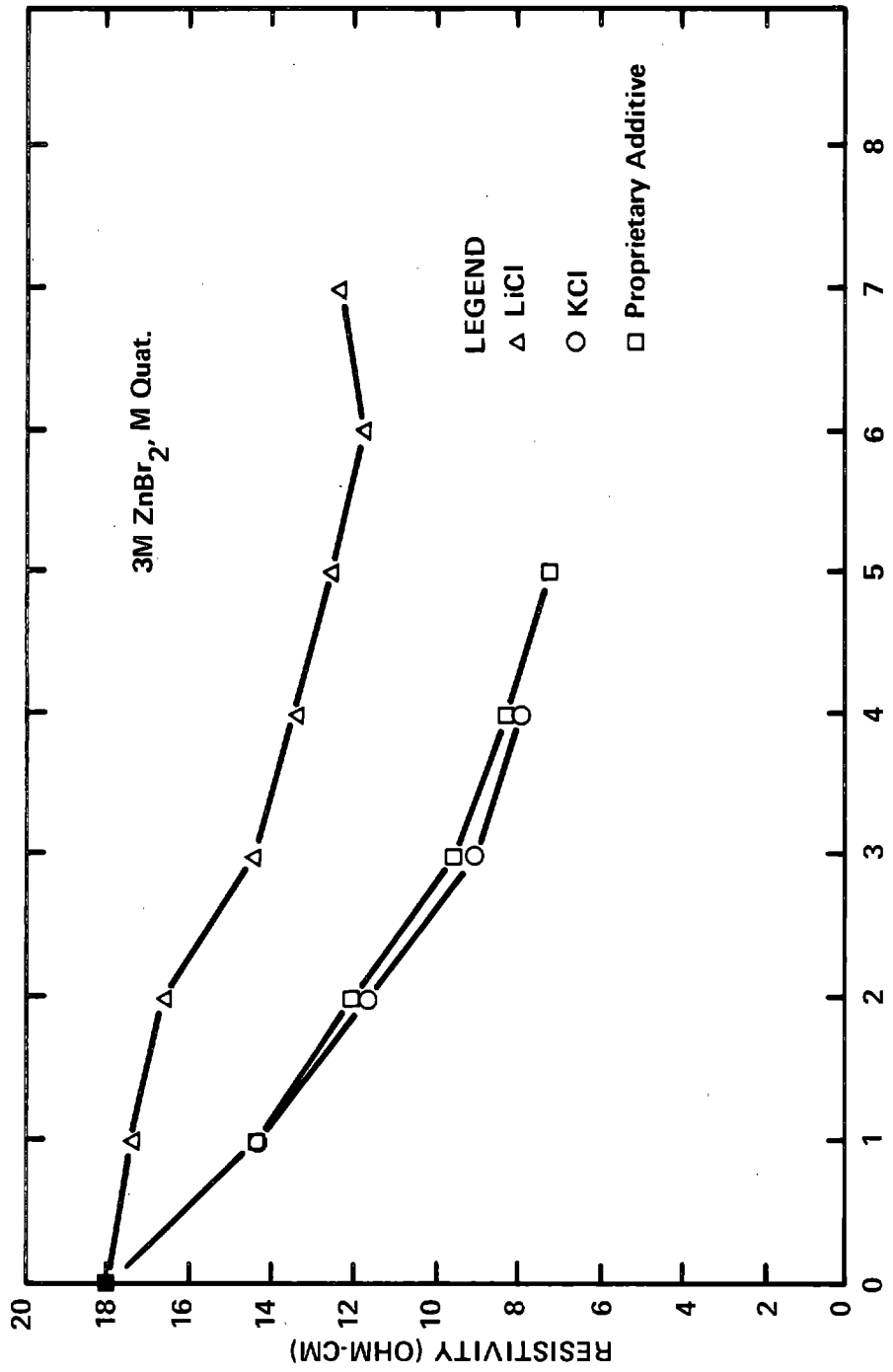

Figure IV-26 Resistivity vs LiCl, KCl, Proprietary Additive

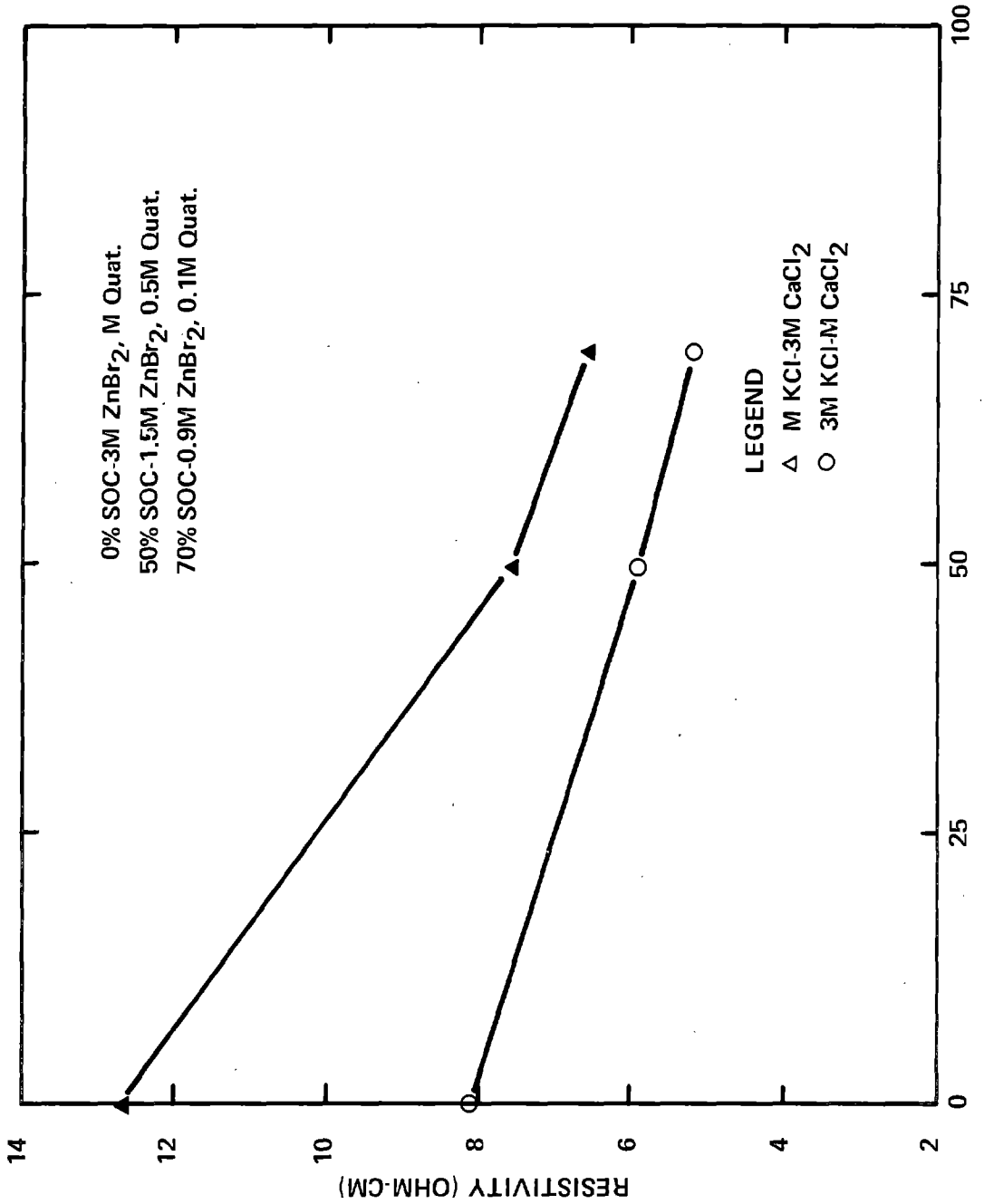

Figure IV-27 Resistivity vs SOC for $KCl/CaCl_2$ Mixtures

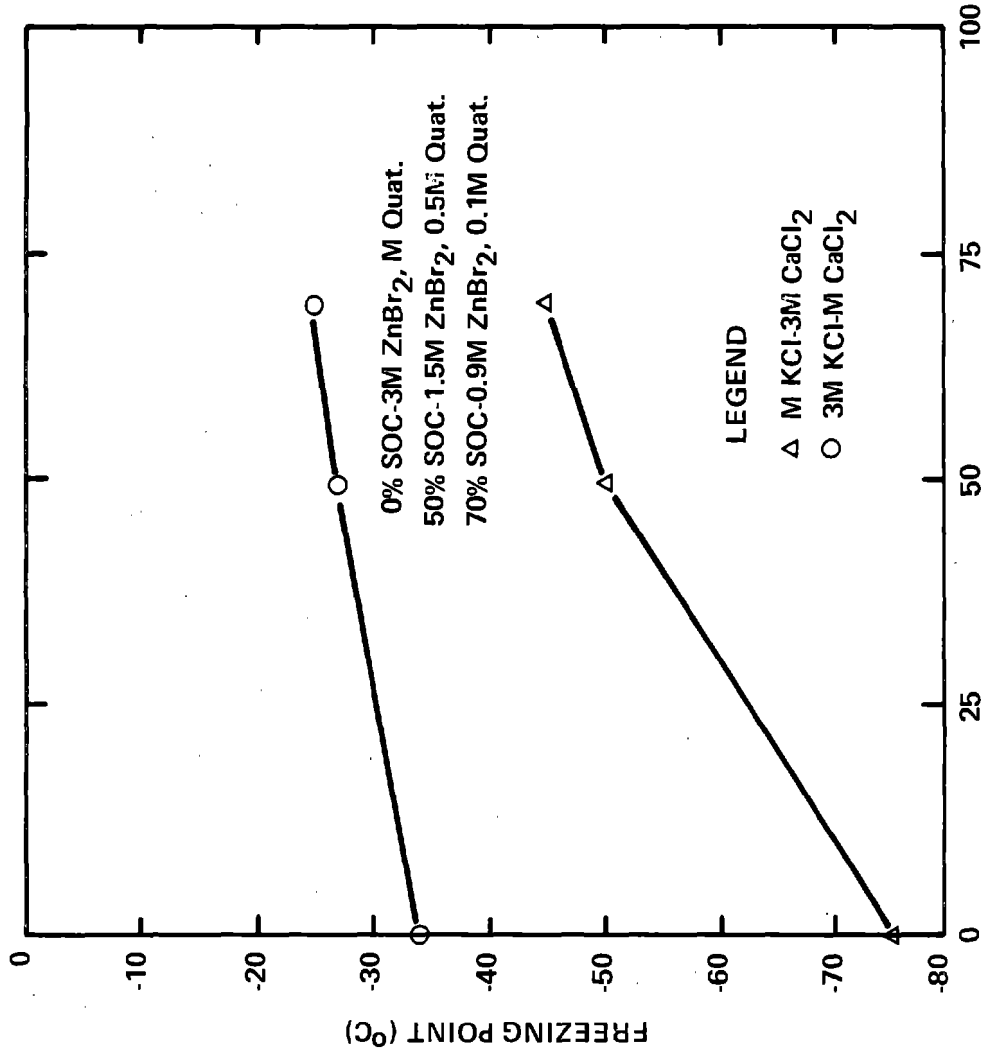

Figure IV-28 Freezing Point vs SOC with Added $KCl/CaCl_2$ Mixtures

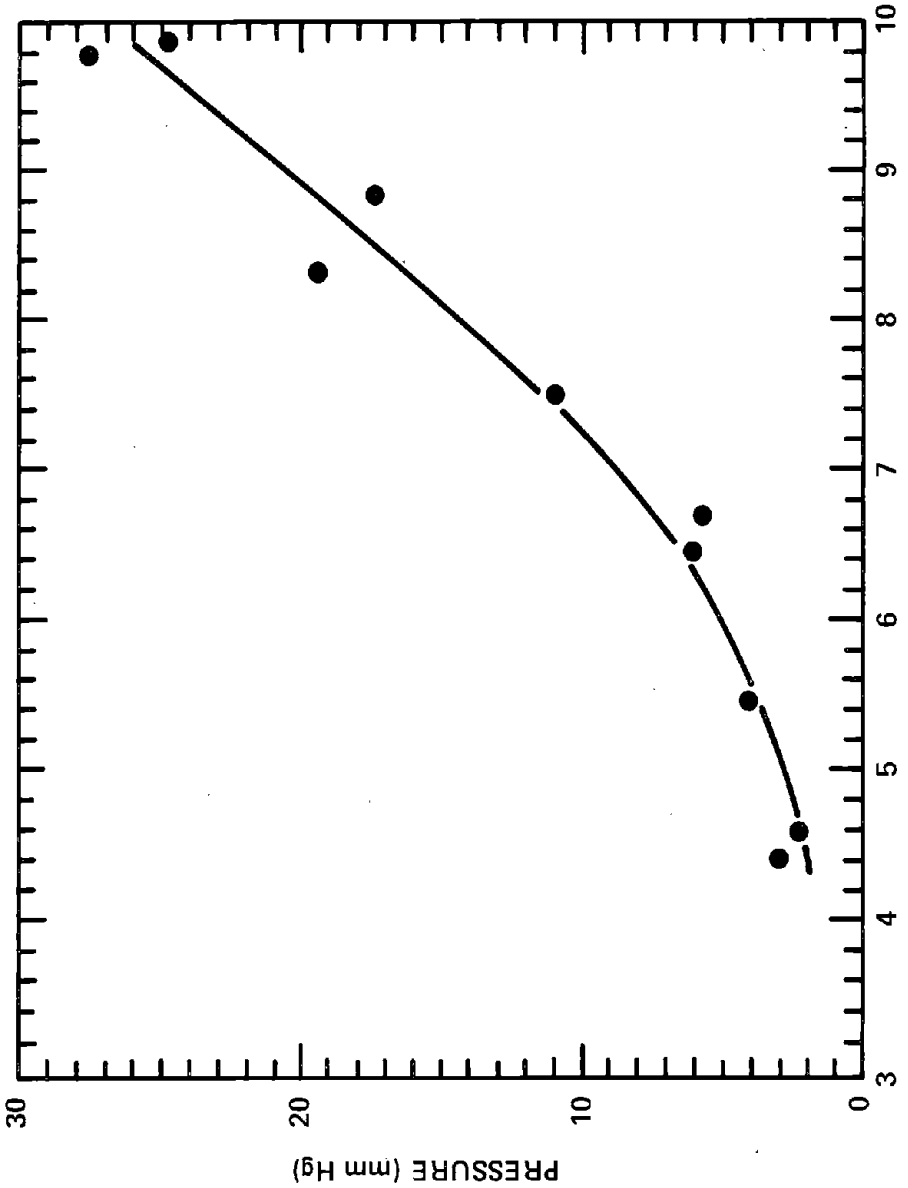

Figure IV-29 Br_2 Vapor Pressure vs Br_2/Complexing Agent Ratio

Table IV-8

Boiling Ranges of MEMBr-Br_2 Complexes

Composition	Boiling Range (^oC)
$(QN)Br_{4.9}$	158-162
$(QN)Br_{6.1}$	134-136
$(QN)Br_{7.9}$	126-128

REFERENCES

1. R. Bellows, H. Einstein, P. Grimes, E. Kantner, P. Malachesky, K. Newby, H. Tsien, Exxon Research and Engineering Company Advanced Energy Systems Laboratory, SAND82-7022 (Albuquerque: Sandia National Laboratories, January 1983).

2. M. Zahn, P. Grimes, and R. J. Bellows, U.S. Patent 4,197,169, April 18, 1980.

3. P. Grimes, R. Bellows, and M. Zahn, U.S. Patent 4,312,735, January 26, 1982.

4. D. Eustace, J. Electrochem. Soc., 127, 528 (1980).

5. Final Report by Arthur D. Little, Inc., EPRI Project 1198-2, 1979.

6. F. Hornstra, E. Berrell, P. Cannon, D. Corp, D. Fredrickson, M. Genge, C. Swoboda, and N. P. Yao, Proceedings of the International Conference on Transportation Electronics (Convergence 80), September 15-17, 1980, Paper C-412.

7. D. W. Kurtz, T. W. Price, and J. A. Bryant, SAE Paper No. 810418, February 1981.

8. N. B. Sargent and M. O. Dustin, SAE Paper No. 810414, February 1981.

APPENDIX I

COST ANALYSIS USING THE ADL METHOD

THE EXXON 20-kWh ZINC-BROMINE BATTERY

A COST ANALYSIS

Based on the

'Revised Guidelines for Estimating the Capital Costs of Advanced Battery Systems for Utility Energy Storage'

(Arthur D. Little, Inc., September 1979)

ARTHUR D. LITTLE COST GUIDELINES

1. Annual product rate - 2500 MWh (125,000 20-kWh modules/year)

2. Production yield - 95% on all required quantities of material and components.

3. Labor rate @ 10.00/h - includes material handling, shipping, receiving and quality control.

4. Overhead rates @ 150% on direct labor and 10% on purchased materials and components. This covers fringe benefits, supervision and general administrative expenses.

5. Rent - (plant) @ $5.00/square foot

6. Equipment Cost and Depreciation - 25% mark-up added to cover installation. Total amortized linearly over 10 year period.

7. Working Capital @ 30% - Value of annual production costs, plus rent and depreciation.

8. $5.00 per kWh added to factory cost. $2.00/kWh of this to represent cost of marketing including related engineering effort. $2.00/kWh represents cost of returns, replacements and field service over the life of the warranty. $1.00/kWh represents remaining miscellaneous costs.

9. After-Tax Return on Investment - Constant annual amount equal to 15% of the initial invested capital (Equipment investment plus working capital).

10. Taxes - The consolidated total of federal, state and local taxes and is to equal the after-tax return on investment.

BATTERY CAPITAL COSTS

Includes factory cost (Items 2, 3, 4, 5, and 6) and items 8, 9 and 10 above.

"The battery capital cost is computed by first deriving a factory cost for one year's production according to the above procedure and then calculating the total investment by summing the working capital requirement (30% of factory cost) and marked-up equipment costs. Return on investment and taxes, together equivalent to 30% per annum of the invested capital, are then added to the factory cost. Finally, $5/kWh are added for marketing, warranty, and miscellaneous costs. The capital cost (selling price) per battery can be obtained by dividing the total by the number of batteries produced annually" (Arthur D. Little, September 1979).

20 kWh ZINC-BROMINE BATTERY

GENERAL DESCRIPTION

The battery shown in Figure AI-1, consists of two 10-kWh battery stacks placed back-to-back with a common center electrolyte feed block. The two-stack module is fastened to a tray serving as a cover for the plastic electrolyte reservoir.

Each of the two battery stacks consists of 78 cells, for a 120V output. The active electrode area per electrode is 180 in^2 (11" high x 16-3/8" wide) as compared to present prototype cells with 90 in^2 electrodes 9-1/2" x 9-1/2").

Each cell consists of two components:

1. A bipolar electrode fabricated by the co-extrusion of a carbon-plastic strip combined with a top and bottom strip of a non-conducting plastic. One side of the carbon-plastic surface is to have a coating or layer to increase the 'surface area'.

2. A separator consisting of an injection-molded plastic separator frame over a separator. The frame is to have electrolyte flow channels, and the separator is to have numerous 'posts' serving as cell spacers.

In addition to 78 separator assemblies and 77 bipolar electrodes per stack, each of the two stacks will contain a compression-molded anode collector and a compression-molded cathode collector. Each stack will contain an outside plastic end block with shunt protective electrodes. Between the two stacks is a common center feed block. Electrolyte (anolyte and catholyte) inlet and outlet fittings at the base of the center block pass through the tray supporting the battery stacks and covering the electrolyte reservoir. Four tie rods at the battery corners are used to secure the two-stack module, in addition to the support achieved by 'heat sealing' the battery stack sides.

Electrolyte (anolyte and catholyte) will be circulated by pump heads (2), submerged in the electrolyte and driven by a single external motor.

Due to the particular requirements of difficult environment and low cost, control devices will be of special design not available in outside markets. In most cases, the controls will be incorporated into existing components, such as end blocks, center feed blocks, reservoir, etc.

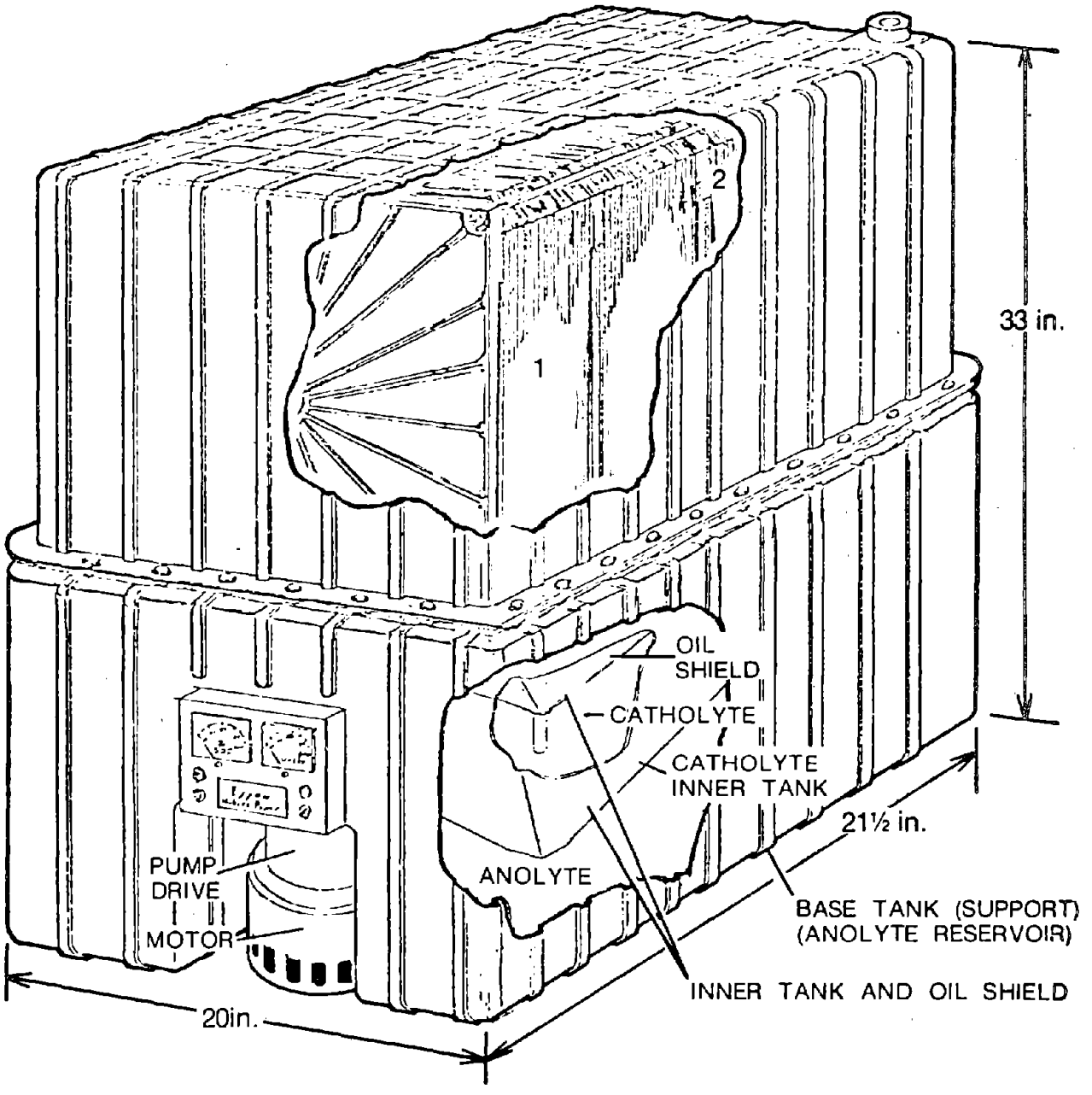

Figure AI-1 20-kWh Zinc-Bromine Battery

20-kWh ZINC-BROMINE BATTERY MODULE

BATTERY WEIGHT ESTIMATES

Electrolyte*	536 lb
Bipolar and Collector Electrodes (158)	31
Separators (156)	5.2
Separator Frames (156)	41.6
End-Support Block (2)	8.3
Center Feed Block	8.3
Reservoir	12.9
Reservoir Tray	3.0

ACCESSORIES

Tie Rods, Nuts, Washers	3.0
Motor and Pumps	25.0
Miscellaneous Controls	8.0
Bus Bars and Miscellaneous Hardware	10.0
Plumbing and Miscellaneous	10.0
	702 lb

Wt./kWh = 35.1 lb/kWh (15.9 kg/kWh)

* Electrolyte weight and volume based on present operational parameters.

*PRODUCTION FLOW LINE - 20-kWh ZINC-BROMINE BATTERY MODULE

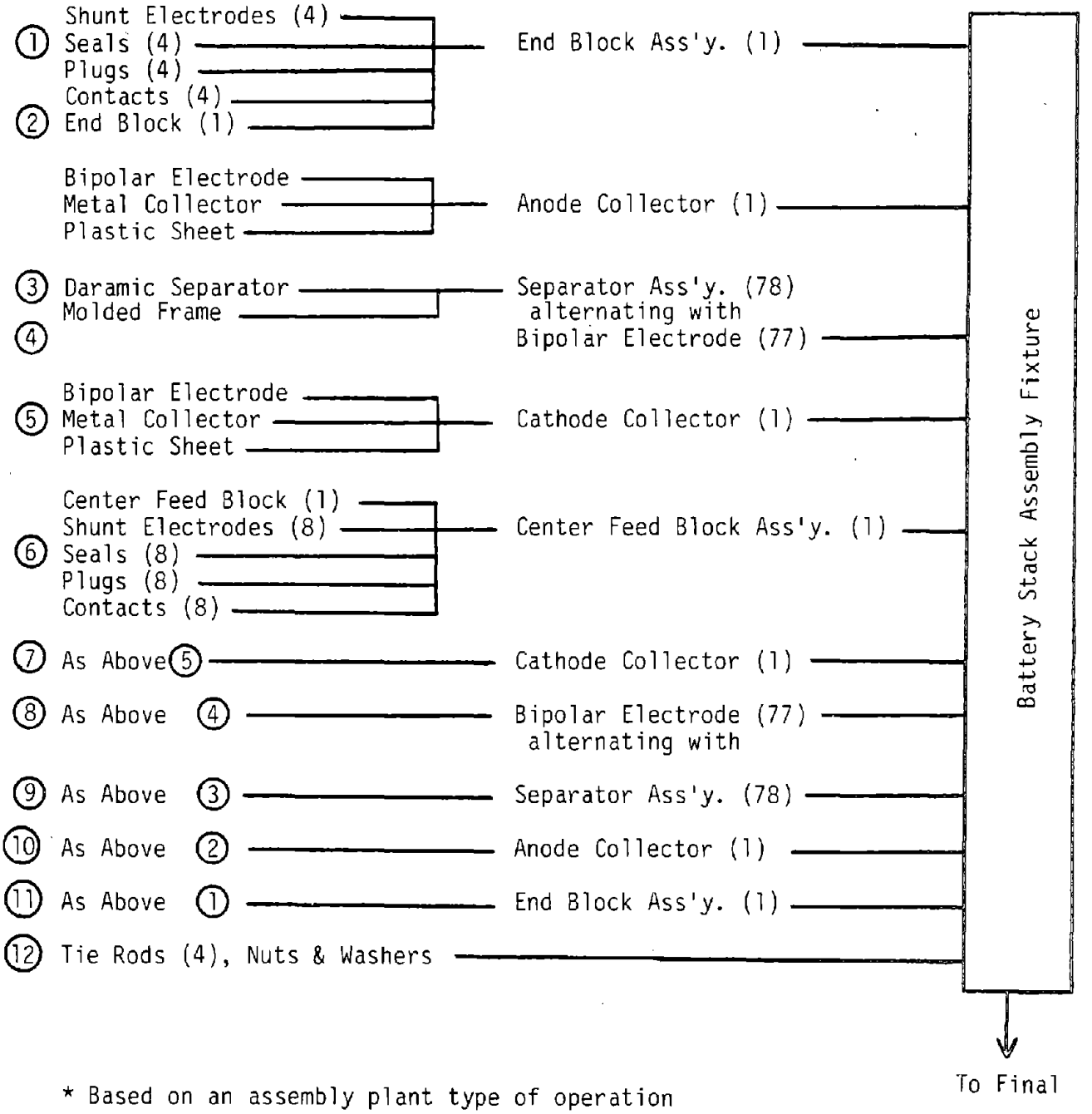

* Based on an assembly plant type of operation

FINAL ASSEMBLY - PRODUCTION FLOW LINE

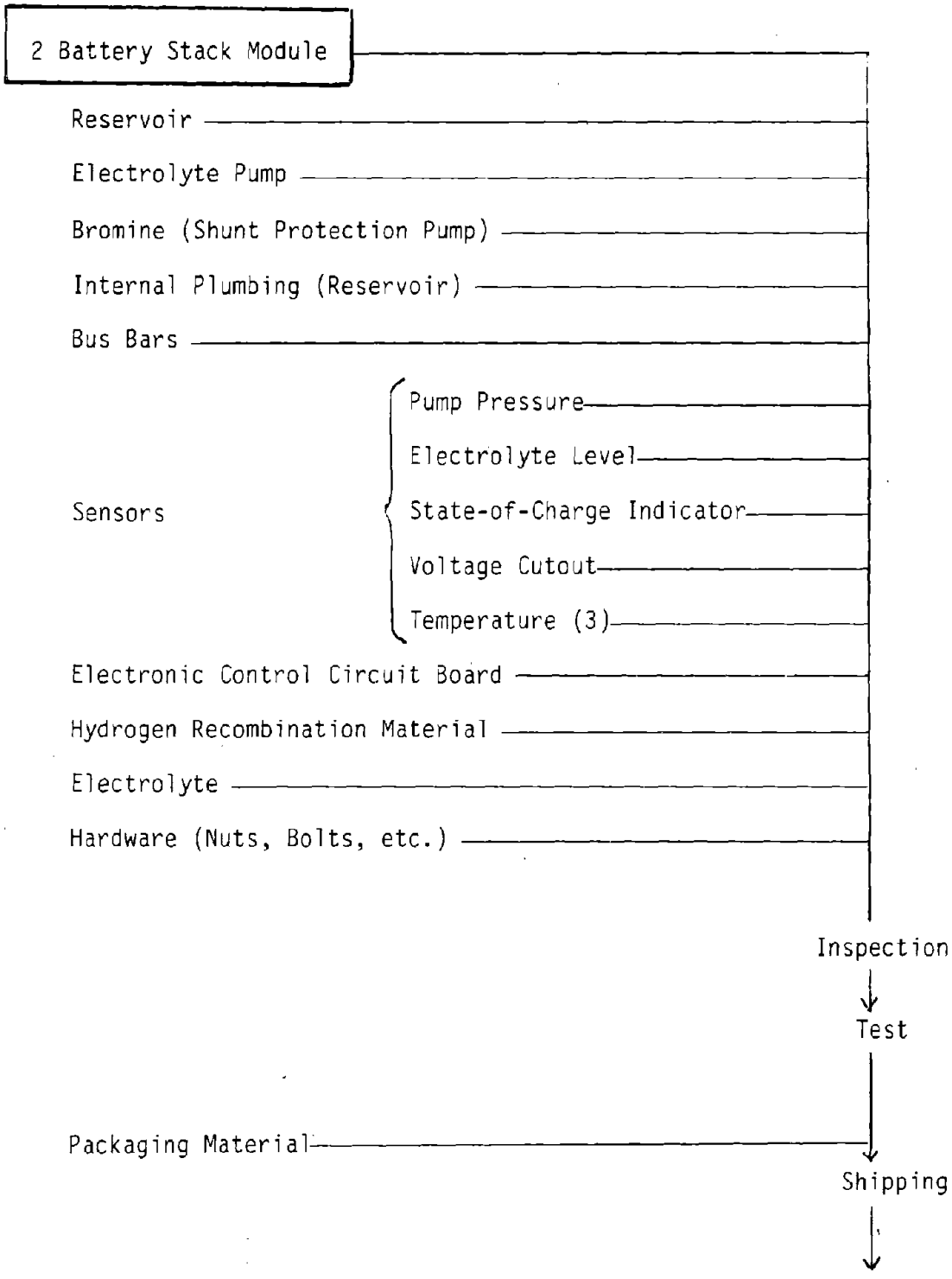

COMPONENT FABRICATION AND COSTS (1980 DOLLARS)

Unit	Material Cost[1]	Factory In-House Labor[2]	Purchased Components[3]	Total Cost Per Module	Description
Bipolar Electrode	.196/each 30.15/Module (154 pcs)	-	.0695 each 10.70 Module (154 pcs)	40.85	Co-extruded conductive plastic strip with non-conductive border. A layer of increased surface area material applied continuously. 1 side part is pierced, blanked, cleaned and stacked continuously.
Current Collector, Consisting of: Silver @ $12.00/troy oz Lead Foil Expanding Foil Silver Plating Plastic Backing Laminating	 3.597 each .165 each - .165 each .150 each - 16.31 Module (4 units)	 .83 each 3.33/Module	 .088 each .35 (4 pcs)	 19.99	'Sandwich' structure of bipolar electrode, silver plated expanded lead-foil and plastic backing. Cycle time-in house labor @ 30 pcs/h.
Separator Assembly, Consisting of: Separator Injection Molded Frame	 .126 each 19.66 (156 pcs)		 .179 each .211 each .39 each 60.84 (156 pcs)	 80.50	Consists of an injection molded frame around a separator sheet. Frame contains manifold holes and electrolyte flow channels. Separator is extruded, cleaned, pierced and blanked continuously. Molding cycle 60 s. 2 per mold yields 120 pcs/h.
End Support Block	4.114 each 8.2 (2 pcs)	.833 each 1.67 (2 pcs)	.847 each 1.69 (2 pcs)	11.59	Injection-molded, glass-filled polypropylene. In-house secondary operations - tapping and deflashing
Total this page	74.35	5.00	73.58	152.93	30 pcs/h.

COMPONENT FABRICATION AND COST (1980 DOLLARS)

Unit	Material Cost[1]	Factory In-House Labor[2]	Purchased Components[3]	Total Cost Per Module	Description
End Support Block Assembly					In-House Assembly of Components 30 pcs/h.
Assembly Blocks	-	-	-	-	
Electrodes (4 pcs)			.18		
Seals (4 pcs)			.10		
Plugs (4 pcs)		Total	.18		
Contacts (4 pcs)		.83	.18	1.47	
Center Support Block Assembly		-		-	*Injection Molding Costs (outside)
Center Block	8.64		1.69*		In-House Tapping 30 pcs/h.
Electrodes (8)			.35		
Seals (8)			.18		In-House Assembly 20 pcs/h.
Plugs (8)	Total		.35	13.47	
Contacts (8)		2.08	.18		
Reservoir	6.81	-	2.28*	9.09	*Injection Molded 4 min cycle (outside vendor)
Reservoir tray	1.56		1.61*	3.17	*Injection Molded 3 min cycle (outside vendor)
Total this page	17.04	2.91	7.28	27.20	1. Base Material Cost @ 95% yield plus 10% Overhead
From previous page	74.35	5.00	73.58	152.93	2. Based at $10.00/h + 150% overhead
Totals	91.36	7.91	80.86	180.13	3. Base Cost @ 95% yield plus 10% overhead - Includes Outside Machine Time and Labor
					Factory Cost (1980 Dollars)

Accessories	Purchased Component Cost*
Electrolyte Pump	$ 26.40
Electrolyte Pump Motor	17.60
Drive System	11.00
Bromine Pump Head	4.40
Bromine Pump Motor	6.60
Pump Pressure Sensor	4.40
Electrolyte Level Sensor	2.20
State-of-Charge Sensor	4.40
Voltage Cutout	1.65
Temperature Probes (3)	3.30
Electronic Control Board	13.70
Hydrogen Recombination	2.20
Plumbing Fittings	11.00
Bus Bars - Tie Rods and and Misc. Hardware	22.00
TOTAL (Accessories)	$130.85
Electrolyte	$220.00

*Base cost @ 95% yield plus 10% overhead includes outside machine time and labor

Assembly Costs

Operation	Cost Per Module*
Stack Assembly - End Blocks, 77 Electrodes Alternating with Separators - Collectors Center Block Assembly - 77 Electrodes Alternating with Separators Collector End Block - Estimated at 6 s per part (Includes Handling and Visual Inspection)	
Assemble 4 Tie Rods, etc. 4 min Heat Seal and Inspect 4 min	
Total time 38 minutes	$15.83
Final Assembly	
Assemble Stack Assembly to Tray and Tray to Reservoir - Assembly Pumps - Controls Bus Bars, Hardware Probes - Gaskets Inspect	
Total time 38 minutes	15.83
Final Test and Inspection	
Inspect and Test - A Percentage of Batteries to Undergo Complete Test Including Several Cycles	
Average time 60 minutes	25.00
Packaging-Shipping - 10 minutes	$ 4.17
Total Labor[2] (In-House)	$60.83
Packaging Materials Est.	$10.00

*Based at $10.00/h + 150% Overhead

Total Factory and Capital Costs

Material (Includes Electrolyte @ $220/Module)	$	321.36
Purchased Components (Includes Outside Molding Costs and Accessories)		211.71
In-House Labor Costs		68.74
Total Material, Components & Labor Cost/20 kWh Module		601.81
Total Material, Components & Labor Cost/kWh		30.09

1. @ 2500 MWh Material, Components & Labor Cost per Year	$75,225,000.00
2. Marked-up Equipment Costs (10% of estimated ($12,500,000)	1,250,000.00
3. Rent (100 sq. ft. Plant @ 5.00/ft^2)	500,000.00
4. Total Factory Costs (Lines 1 + 2 + 3)	76,975,000.00
5. Working Capital Requirement (30% line 4)	23,092,500.00
6. Total Investment ($12,500,000 + line 5)	35,592,500.00
7. Return on Investment & Taxes (30% line 6)	10,677,750.00
8. Additional @ $5.00/kWh	12,500,000.00
9. Total Capital Cost (lines 4, 7 & 8)	100,152,750.00
Capital Cost per 20 kWh Module	801.22
Capital Cost per kWh	40.06

- Net Capital Costs Following Page -

Salvage Value and Net Costs

Electrolyte Salvage Value	
225 lbs Zn/Br_2 @ .30/lb	$ 67.50
50 lbs Quaternary Ammonium Bromide @ .70/lb	35.00
$16.31 Silver @ 50% Recovery	
Value (Includes Disassembly Costs)	8.15
Copper - Est. $9.00 @ 50% Value	4.50
Total per 20 kWh	115.15
Salvage Value/kWh	5.76
From Previous Page	
Capital Cost per kWh	40.06
- Salvage Value	- 5.76
Net Capital Cost/kWh	$ 34.30

Notes:

- Additional salvage possible but minimal (motors, controls, etc.)
- Indicated costs are based on 80% coulombic efficiency and 10% auxiliary power (present battery design and parameters). Further cost reductions are possible in future batteries. Larger battery modules consisting of 8 to 12 battery stacks with single pumps and reservoirs serving all stacks in comparison to only two stacks in this analysis would obviously reduce cost appreciably.

APPENDIX II

COMPUTER SIMULATION OF ZINC-BROMINE BATTERY PERFORMANCE

Introduction

Exxon's zinc-bromine battery consists of parallel connections of bipolar stacks of secondary zinc-bromine cells [1]. The energy capacity of this battery is decreased by the pumping energy requirement, the protective energy required to reduce shunt current losses and the unproductive side reactions such as hydrogen generation and self-discharge due to bromine attacking the deposited zinc. While the extent of the side reactions are primarily controlled by battery construction materials, the energy capacity losses due to pumping and protective energy can be minimized by proper selection of design parameters such as the flow channel width (see Figures AII-1a and AII-1b) and the electrolyte resistivity.

In this appendix, a simple theoretical model of Exxon's zinc-bromine battery is developed which can be used to select the electrolyte resistivity and flow channel width which maximize the energy efficiency of the battery. The model is based on the geometry of the cells as shown schematically in Figures AII-1a and AII-1b. (Note that for simplicity of presentation the separators between the electrodes have been excluded from Figure AII-1b.) The pumping energy requirement is based on equations for assumed hydrodynamic conditions of the electrolyte with the manifolds and flow frames. The equations which describe the protective energy required to reduce the shunt current losses are described elsewhere [2].

Model

The energy efficiency (η_E) of Exxon's zinc-bromine battery is defined here to be the energy capacity (E_c) of the battery minus the protective energy required to minimize shunt current losses (E_{SD}) and the pumping energy (E_{pD}) during discharge divided by the sum of the input energy, the pumping energy on

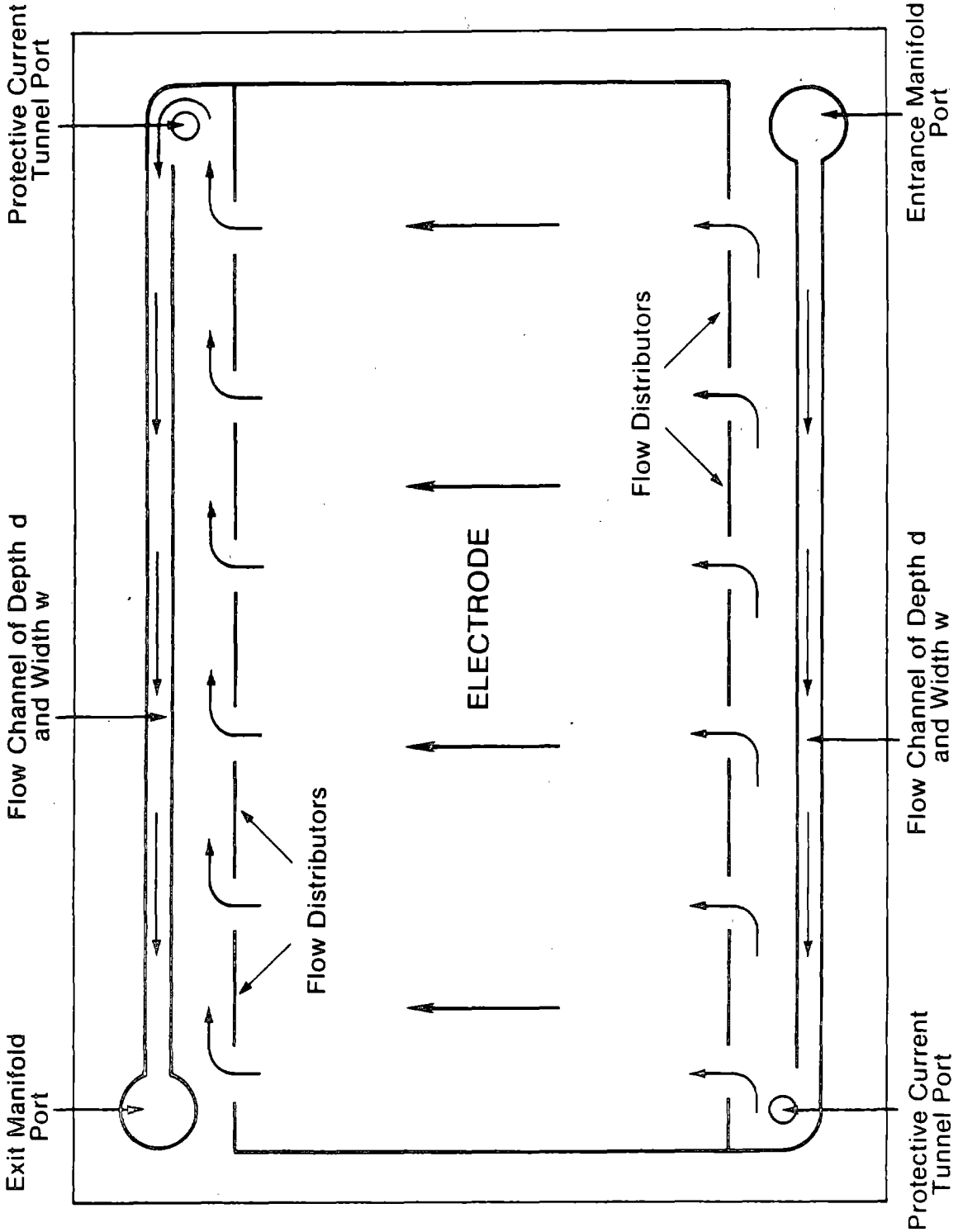

Figure AII-1a Schematic of an Electrode Flow Frame Showing Flow Channels of Length ℓ, Manifold Ports, and Tunnel Ports

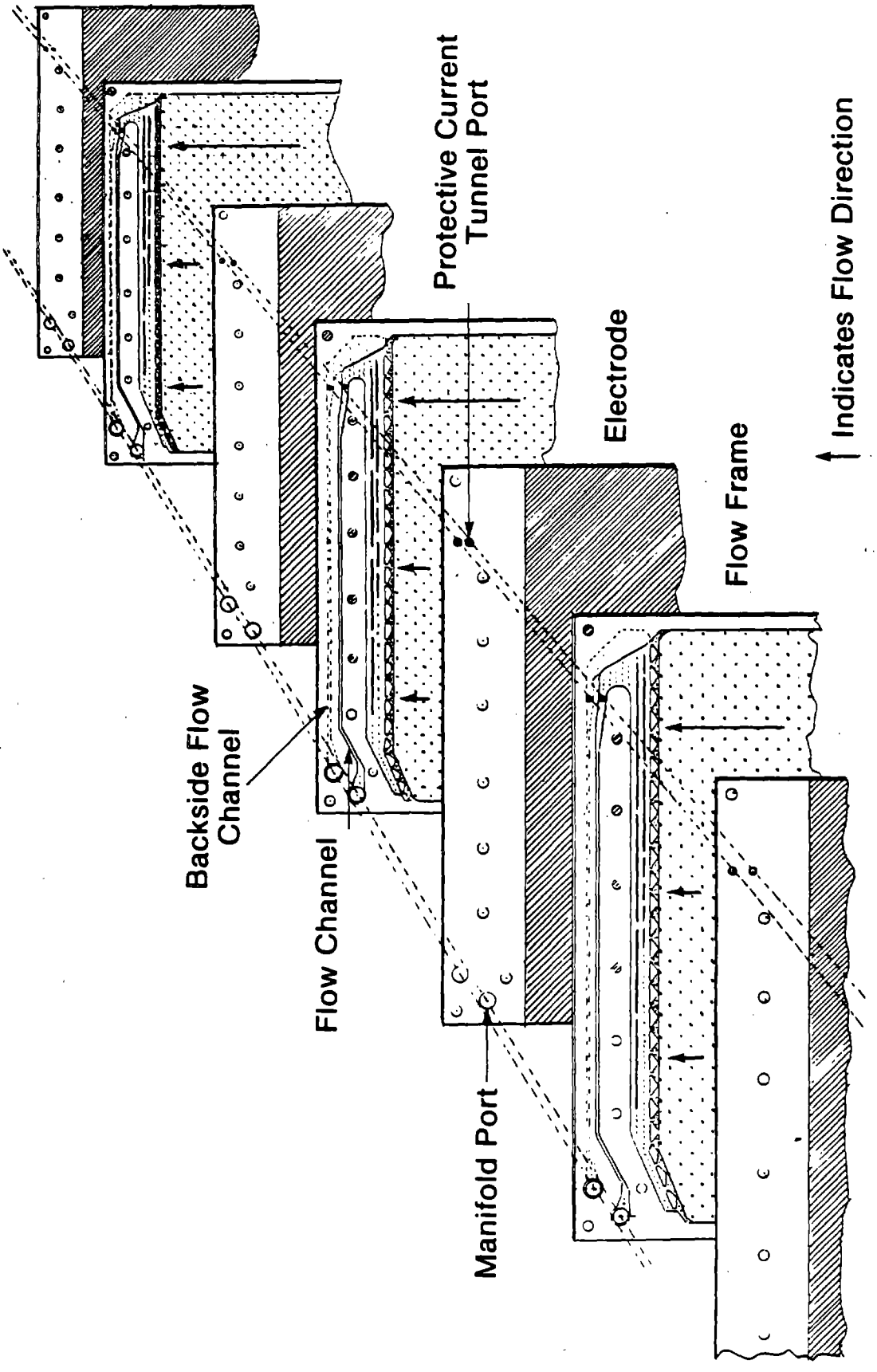

Figure AII-1b Schematic Showing Multiple Flow Frames and Electrodes

charge and the protective energy on charge:

$$\eta_E = \frac{E_c - (E_{SD} + E_{pD})}{E_I + E_{SC} + E_{pC}} \tag{1}$$

The energy capacity of the battery, input energy, protective energy, and pumping energy can be predicted based on simple equations which are functions of the design and operating parameters of the battery as described below.

Energy Capacity and Input Energy

The energy capacity of the battery depends on the number of stacks (N_s), the voltage of a stack on discharge (V_{TD}), the terminal current on discharge per stack (I_{TD}), and the time of discharge (T_D):

$$E_c = N_s V_{TD} I_{TD} T_D \tag{2}$$

The terminal current on discharge per stack depends on the specified current density on discharge (i_D) and the length (L) and width (W) of the electrodes of a cell:

$$I_{TD} = i_D L W \tag{3}$$

The voltage of a stack on discharge depends on the number of cells in a stack (N), the open-circuit voltage of a single cell (V^o), the terminal current on discharge per stack, and the resistance of an individual cell (R_e):

$$V_{TD} = N(V^o - I_{TD} R_e) \tag{4}$$

The individual cell resistance depends on the electrode length and width, the specific resistivity of the electrolyte (ρ_e), and the effective electrolyte thickness of the anolyte chamber ($t_1\tau_1/\varepsilon_1$), separator ($\lambda\tau/\varepsilon$), and the catholyte chamber ($t_2\tau_2/\varepsilon_2$) of a cell:

$$R_e = \frac{\rho_e \left[\frac{t_1 \tau_1}{\varepsilon_1} + \frac{\lambda \tau}{\varepsilon} + \frac{t_2 \tau_2}{\varepsilon_2} \right]}{LW} \tag{5}$$

The time of discharge depends, as can be shown by a charge balance, on the specified current density on charge (i_c), the specified time of charge (T_C) and the calculated self-discharge current density (i_{Sd}):

$$T_D = \frac{T_C \, (i_c - i_{Sd})}{i_D + i_{Sd}} \tag{6}$$

(Note that for convenience the sign of the self-discharge current density i_{Sd} is defined to be positive.) The self-discharge current density is the sum of the self-discharge due to bromine attacking the deposited zinc and hydrogen generation. The self-discharge current density due to the bromine reaction is a function of the number of electrons involved in the self-discharge (corrosion) reaction (n_e), the diffusion coefficient of bromine ($\mathcal{D}_{Br_2}$), the concentration of bromine in the anolyte (C_1) and the catholyte (C_2) chambers of a cell, the effective electrolyte thickness of the separator, and the thicknesses of the diffusion layers on the anolyte (δ_1) and catholyte (δ_2) sides of the separator and on the deposited zinc (δ_{Zn}):

$$i_{Sd} = \frac{n_e F \mathcal{D}_{Br_2} \, (C_2 - C_1)}{\frac{\lambda \tau}{\varepsilon} + \delta_1 + \delta_2 + \delta_{Zn}} + i_{H_2} \tag{7}$$

The input energy is related simply to the voltage of a stack on charge (V_{TC}), the terminal current on charge per stack (I_{TC}), the number of stacks and the specified time of charge (T_c):

$$E_I = N_s \, V_{TC} \, I_{TC} \, T_C \tag{8}$$

where

$$V_{TC} = N(V^{o} + I_{TC}\, R_e) \tag{9}$$

and

$$I_{TC} = i_c\, L\, W \tag{10}$$

Protective Energy

The protective energy per stack required to minimize the shunt current losses during charging is related simpy to the tunnel protective current during charging (t_{oC}), the number of stacks, the number of cells per stack, the open-circuit voltage of a cell, and the charging time (T_C):

$$E_{SC} = 4N_s\, N\, (V^{o} + I_{TC}\, R_e)\, t_{oC} T_C \tag{11}$$

where the 4 is used because there are 4 protective current tunnels in each stack. Similarly, the protective energy per stack during discharge is

$$E_{SD} = 4N_s\, N(V^{o} - I_{TD}\, R_e)\, t_{oD}\, T_D \tag{12}$$

The protective current depends on the design parameters of the cell as follows [2,3,4]:

$$t_{oC} = \frac{V^{o} + I_{TC}\, R_e}{R_m} \quad \frac{(\lambda_t^{N/2} - 1)^2}{\lambda_t^{N} + 1} \tag{13}$$

where

$$R_m = \frac{4\rho_e(\lambda + t_1 + t_2 + t_3)}{\pi D^2} \tag{14}$$

in which t_3 and D represent the thickness of a bipolar electrode and the manifold diameter, respectively. The quantity λ_t is related to the design

parameters of the battery:

$$\lambda_t = \frac{\beta}{2} + \left[\left(\frac{\beta}{2}\right)^2 - 1\right]^{1/2} \tag{15}$$

where

$$\beta = 2 + \frac{R_m}{R_c} \tag{16}$$

in which the resistance of a channel (R_c, either inlet or outlet) is given by

$$R_c = \frac{\rho_e \ell}{wd} \tag{16}$$

where ℓ, w, and d represent the channel length, width, and depth, respectively, as shown in figure AII-1a. Similarly, the protective current during discharge (t_{oD}) depends on the design parameters of the cell and it differs from t_{oC} only in the voltage requirement:

$$t_{oD} = \frac{(V^o - I_{TD} R_e)}{R_m} \quad \frac{(\lambda_t^{N/2} - 1)^2}{\lambda_t^N + 1} \tag{18}$$

Finally, if the open circuit time is neglected, the cycle time is simply the sum of the time on charge and discharge

$$CT = T_D + T_C \tag{19}$$

Pumping Energy

The total pumping energy required to move electrolyte through the battery is the sum of the pumping energy during charge and discharge and is related to the number of stacks, the cycle time, the total pressure drop per stack (ΔP_T), the volumetric flow rate per stack per electrolyte (Q_T), and the pump efficiency (η_p):

$$E_p = E_{pC} + E_{pD} = \frac{2N_s \Delta P_T Q_T T_C}{\eta_p} + \frac{2N_s \Delta P_T Q_T T_D}{\eta_p} \quad (20)$$

where the 2 is used because it is assumed that the pumping energy is the same for the anolyte and catholyte. When the pressure drop across the electrodes is neglected, the total pressure drop per stack is the sum of the pressure drop in the manifolds (includes both the inlet and the outlet) and the channels

$$\Delta P_T = \Delta P_m + 2\ \Delta P_C \quad (21)$$

where ΔP_C is the pressure drop per channel and the 2 is used to account for the pressure drop in the inlet and outlet channel of each flow frame. The pressure drop through the manifolds is given by the following correlation [5]:

$$\Delta P_m = \frac{\rho (Q_{Tg})^2}{790.6\ D^4} \quad (22)$$

where ΔP_m is in psi, ρ is the density of the electrolyte in g/cm^3, D is the manifold diameter in inches, and Q_{Tg} is the total volumetric flow rate in gallons per min. A value for Q_{Tg} can be obtained from the total volumetric flow rate of each electrolyte in cm^3/min (Q_T) by using the appropriate conversion factor and the design parameters of the battery and a specified volumetric flow rate per unit electrode area (Q_1):

$$Q_T = N\ L\ W\ Q_1 \quad (23)$$

The pressure drop per channel (ΔP_C) is assumed to be given by the following expression for laminar flow in a slit [6]:

$$\Delta P_C = \frac{1.5 \mu \ell Q_T}{N \left(\frac{d}{2}\right)^3 w} \qquad (24)$$

where μ is the viscosity of the electrolyte.

A program was developed to calculate the energy efficiency of the battery by utilizing the above equations in essentially reverse order. That is, the design and operating parameters are specified and the above equations used sequentially to calculate intermediate values and the energy efficiency of the system.

RESULTS

Consideration of the above equations reveals that the energy efficiency of the battery is a complicated function of the channel width (w) and the electrolyte resistivity (ρ_e) when the operating conditions, and the other geometric parameters and physical constants are specified. That is, when the design parameters of Table AII-1 are specified, the protective energy ($E_S = E_{SC} + E_{SD}$) is a function of both the channel width and the electrolyte resistivity while the energy capacity (E_c) and the input energy (E_I) are only functions of the electrolyte resistivity; also, the pumping energy (E_p) is only a function of the channel width.

Figures AII-2-4 show the responses of these individual contributions (i.e., E_p, E_c, E_I, E_s) to the energy efficiency of the battery as a function of the channel width and electrolyte resistivity when the other parameters are specified according to Table AII-1.

Figure AII-2 shows that the pumping energy during discharge is less than the pumping energy required during charge which emphasizes that the discharge time is less then the charge time due to the self-discharge current density (see

Table A II-1 Design Parameters

Variable Name	Brief Description
C_1	Concentration of bromine in the anolyte
C_2	Concentration of bromine in the catholyte
d	Channel depth
D	Manifold diameter
$\mathcal{D}_{Br_2}$	Bromine diffusion coefficient
i_c	Charging current density
i_D	Discharge current density
i_{H_2}	Self-discharge current density due to hydrogen evolution
ℓ	Channel length of the flow channel of width w and depth d
L	Electrode length
n_e	Number of electrons in bromine self-discharge reaction
N	Number of cells per stack
N_s	Number of stacks
Q_1	Volumetric flow rate per unit of electrode area
t_1	Anolyte chamber thickness of a cell
t_2	Catholyte chamber thickness of a cell
t_3	Bipolar electrode thickness
T_c	Time of charge
V^o	Open-circuit voltage of a cel
W	Electrode width

GREEK SYMBOLS

δ_1	Diffusion layer thickness on anolyte side of separator
δ_2	Diffusion layer thickness on catholyte side of separator
δ_{Zn}	Diffusion layer thickness on deposited zinc
ε	Porosity of the separator
ε_1	Porosity of the anolyte chamber
ε_2	Porosity of the catholyte chamber
η_p	Electrolyte pump efficiency
λ	Separation thickness
ρ	Electrolyte density
τ	Separator tortuosity
τ_1	Anolyte tortuosity
τ_2	Catholyte tortuosity

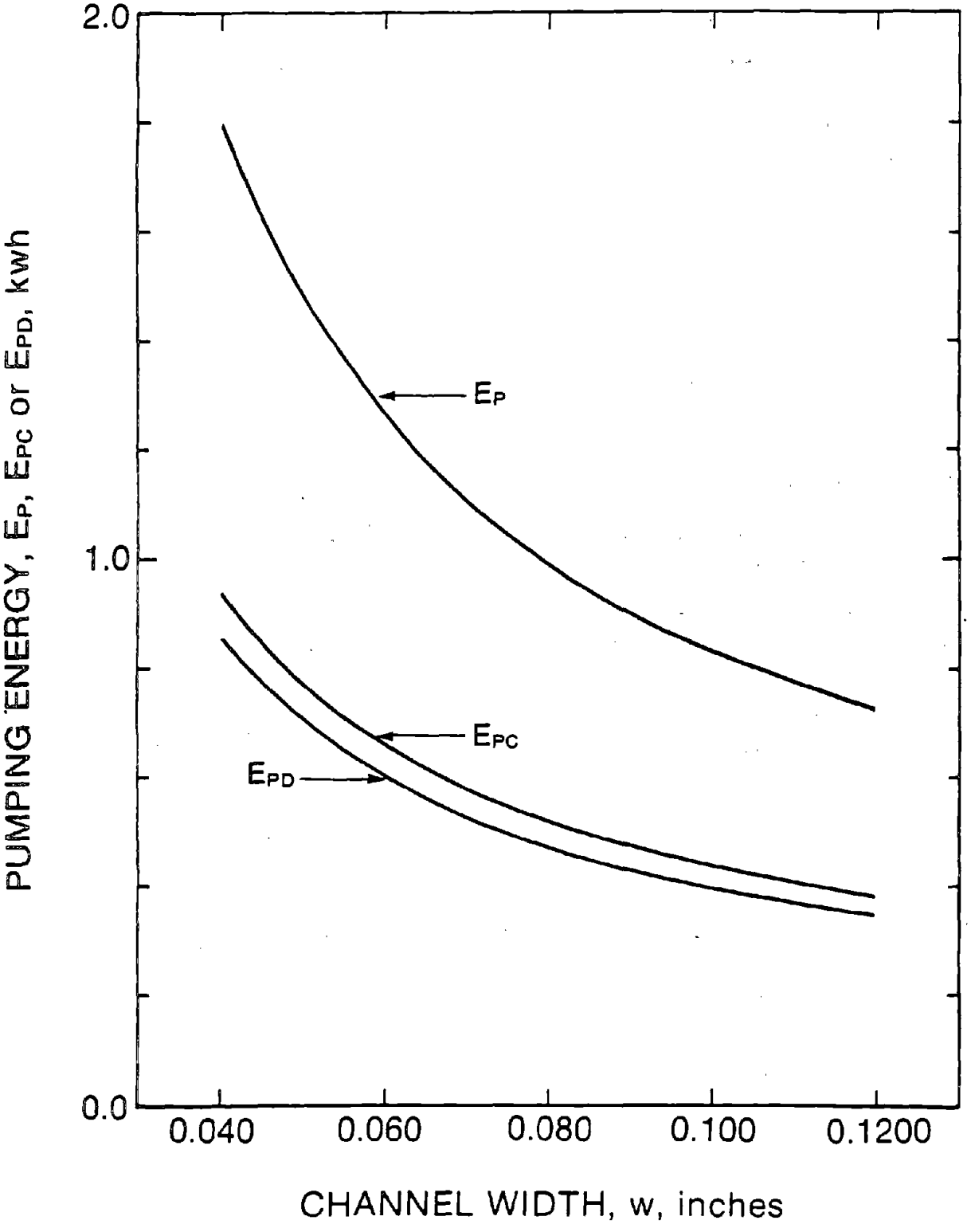

Figure AII-2 Dependence of Pumping Energy on Channel Width

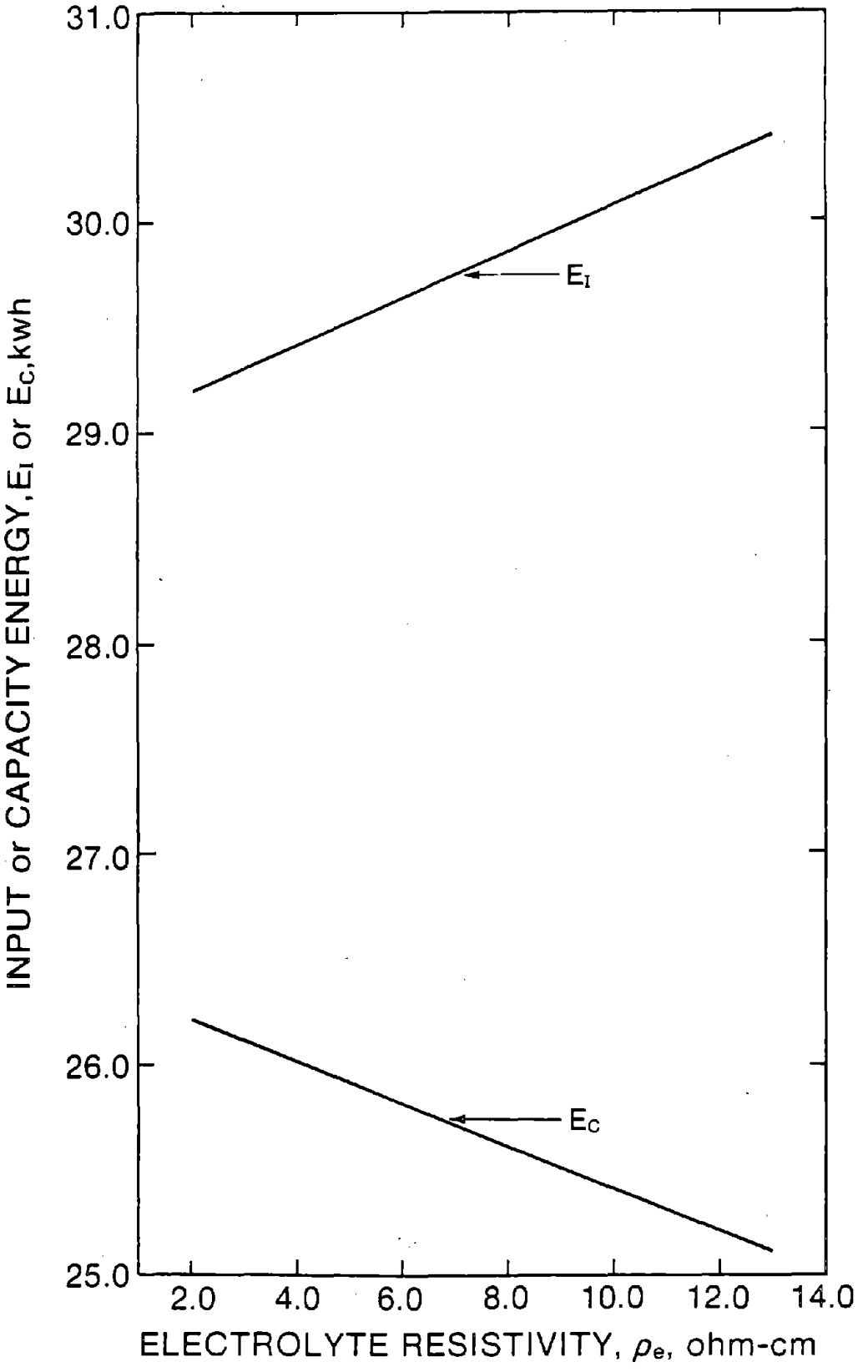

Figure AII-3 Effect of Electrolyte Resistivity on Input Energy and Battery Capacity

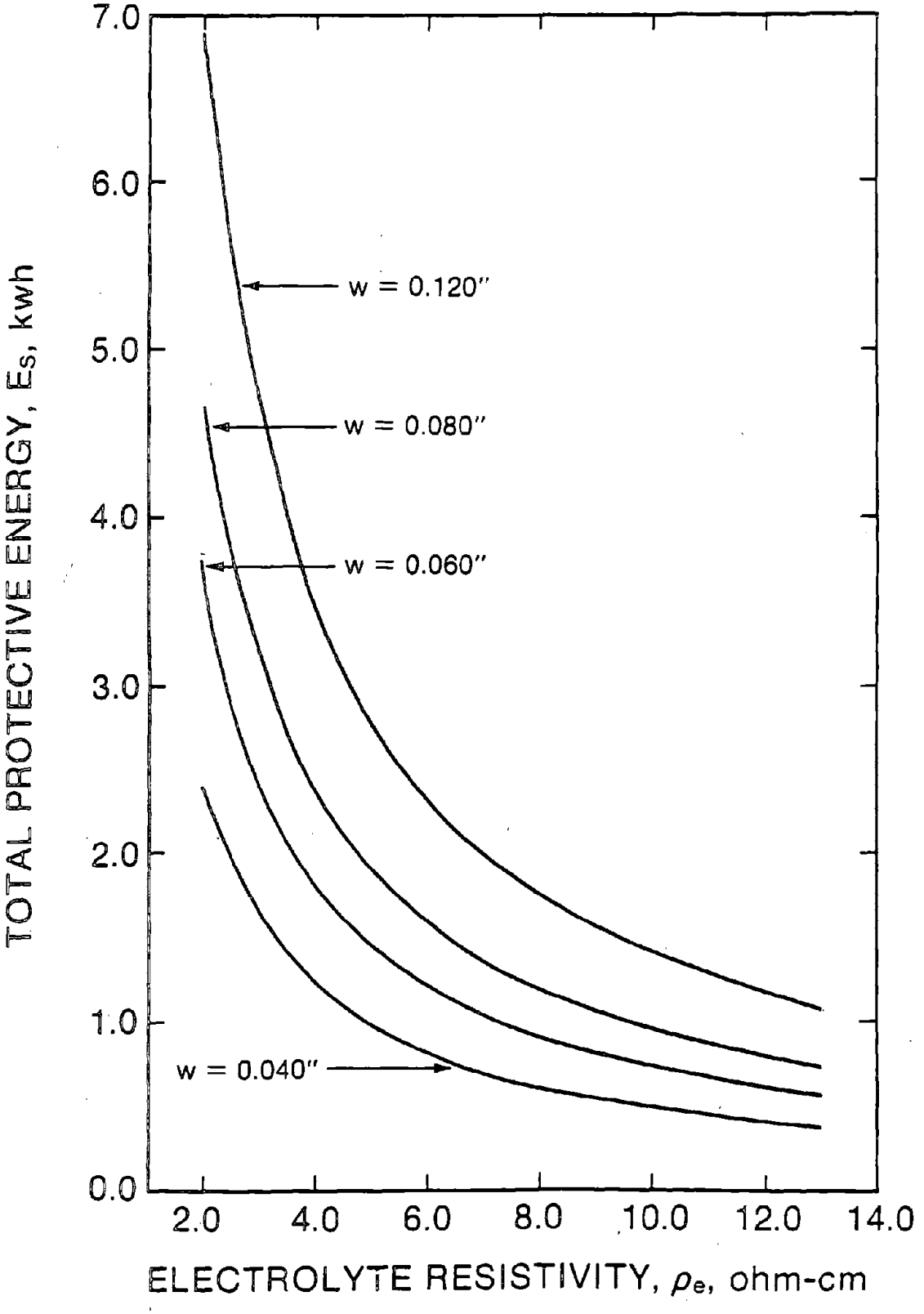

Figure AII-4 Dependence of Protective Energy on Channel Width and Electrolyte Resistivity

equation 6). Comparison of the scale for pumping energy and the scale for the input or capacity energy of Figure AII-3 indicates that the pumping energy consumes about 3-4 percent of the energy on charge or discharge. The difference between the input energy (E_I) and the battery capacity (E_c) in Figure AII-3 results from both the self-discharge current density (often known as a coulombic loss) and the voltage inefficiency caused by the internal resistance of the cell. Figure AII-4 shows that the protective energy (E_s) increases with both electrolyte resistivity and channel width and that the total protective energy requirement is approximately the same as the total pumping energy requirement at low channel widths and high electrolyte resistivities. Figure AII-5 shows the dependence of the energy efficiency (as calculated from equation 1) on these two design parameters. Thus for the set of operating conditions and geometric parameters of Table 1, Exxon's zinc/bromine battery has a maximum energy efficiency of 79.6% for ρ_e and w equal to 5.5 ohm-cm and 0.062 inches, respectively.

Figure AII-6 indicates that this maximum may be increased 1% by changing separator thickness (λ) from the Table AII-1 (and Figs. AII-2,3,4,5) values of 0.024 inches to a thickness of 0.035 inches at an electrolyte resitivity of 6 ohm-cm. This increased thickness increases the internal cell resistance (R_e) but it decreases the self discharge current density (i_{Sd}); thus, the increase in coulombic efficiency is greater than the decrease in voltage efficiency at a channel width of 0.062 inches and with the other design parameters specified in Table AII-1.

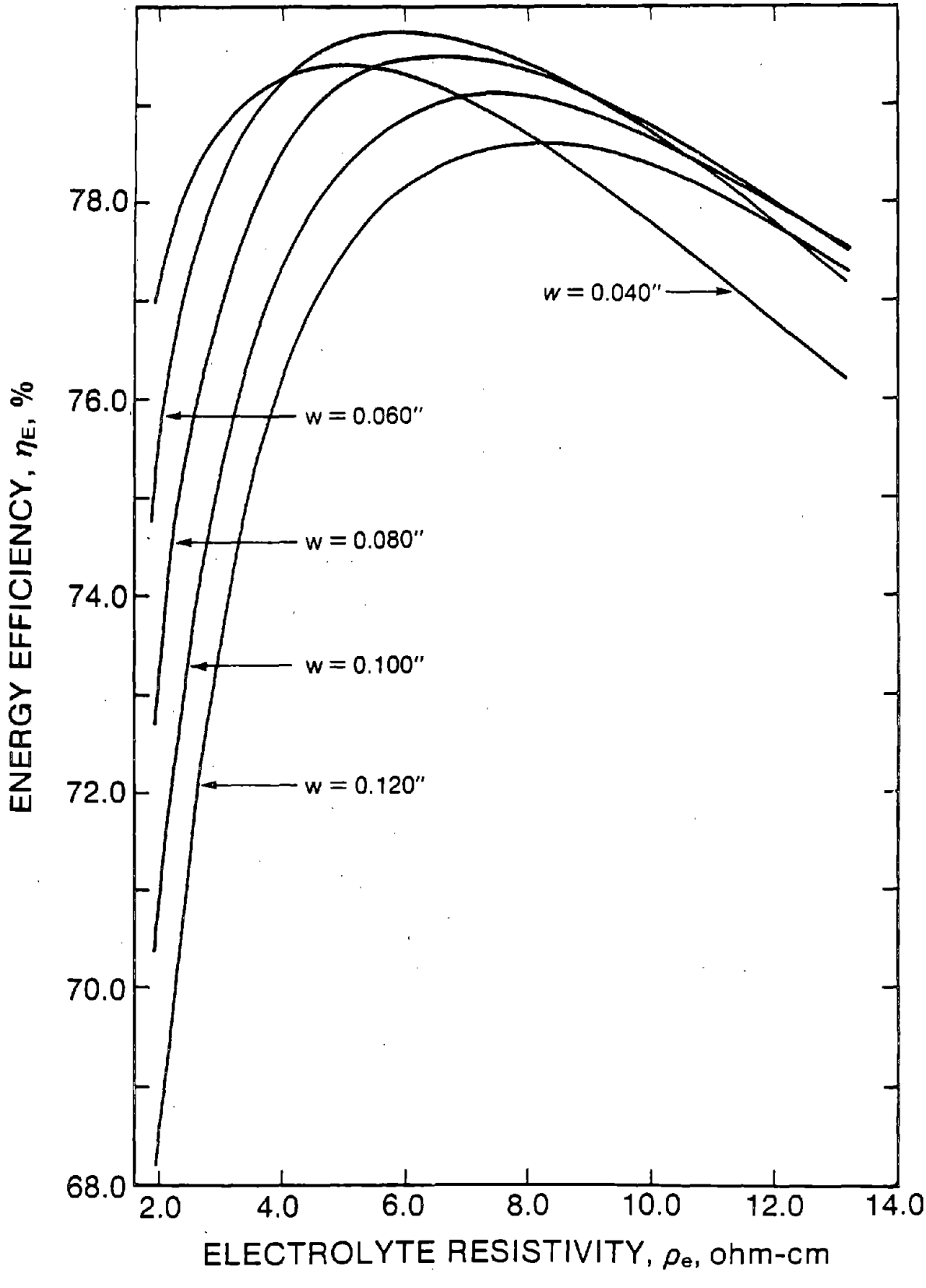

Figure AII-5 Effect of Channel Width and Electrolyte Resistivity on Energy Efficiency

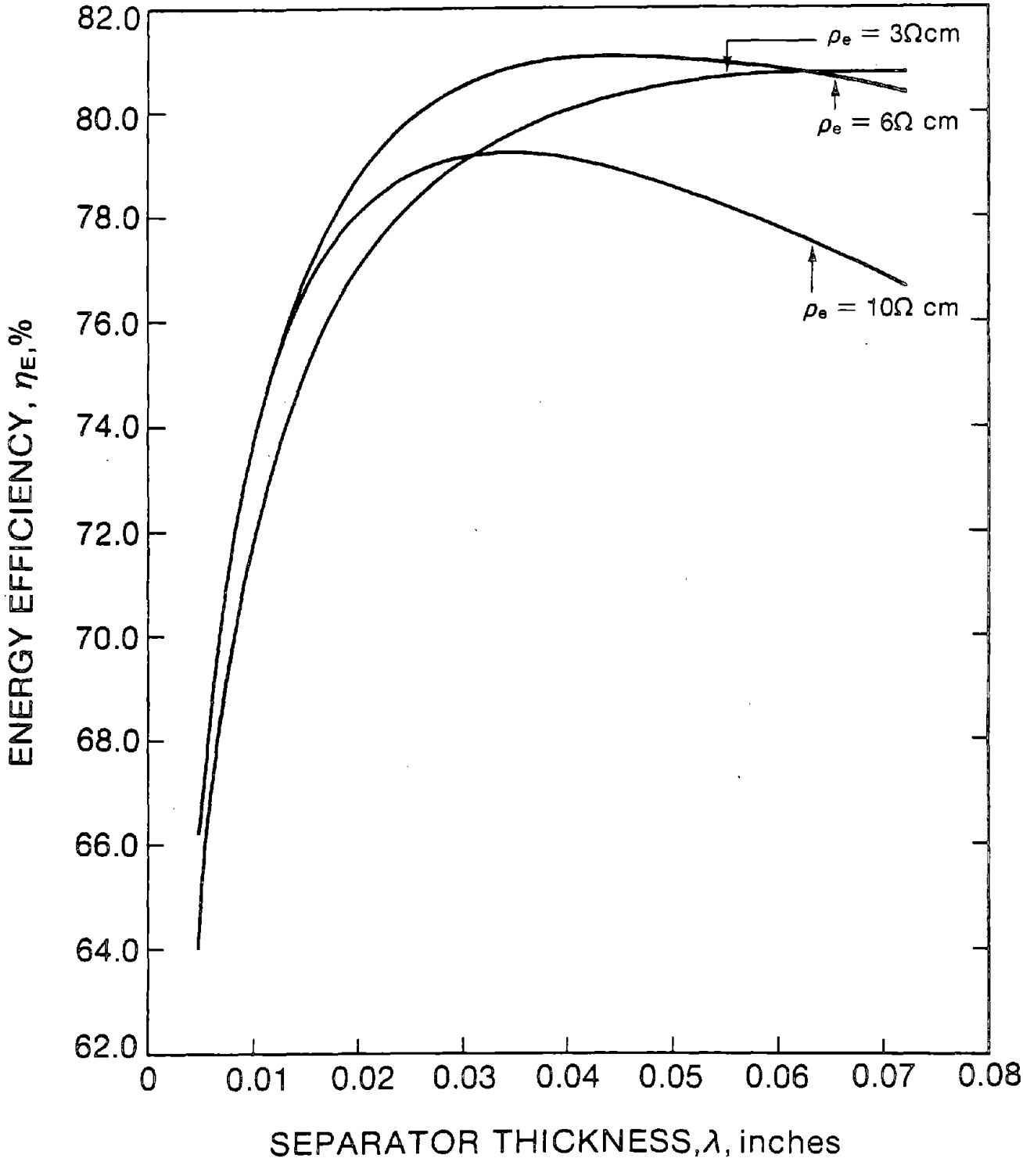

Figure AII-6 Dependence of Energy Efficiency on Separator Thickness and Electrolyte Resistivity When the Channel Width is 0.062 Inches

CONCLUSIONS

The simple model of Exxon's zinc-bromine battery presented here can be used to predict the energy efficiency of the battery as a function of the design variables. Consequently, the model may be useful as an aid to help select among alternative designs.

REFERENCES

1. Grimes, P. G. and Bellows, R. J., "Shunt Current Control Methods in Electrochemical Systems - Applications", Recent Advances in Electrochemical Cell Design - AIChE Symposium, American Institute of Chemical Engineers Meeting, Houston, TX March 27-31, 1983.

2. Grimes, P. G., Bellows, R. J. and Zahn, M. "Shunt Current Control in Electrochemical Systems - Theoretical Analysis," Recent Advances in Electrochemical Cell Design - AIChE Symposium, AIChE Meeting, Houston, TX, March 27-31. 1983.

3. Zahn, M., Grimes, P. and Bellows, R., "Parasitic Current Elimination in Series-Connected Electrochemical Cell Systems with Shared Electrolyte. Part III - Channel Interconnects," Extended Abstracts 81-1, Electrochemical Society Meeting, Minneapolis, MN, May 1981.

4. Grimes, P., Zahn, M. and Bellows, R. "Shunt Current Elimnation," U.S. Patent 4,312,735, January 26, 1982.

5. Private communication, C. E. Jahnig (1981)

6. Bird, R. B., Stewart, W. E. and Lightfoot, E. N., Transport Phenomena, John Wiley, NY, 1961, p. 62.

NOMENCLATURE

Variable Name	Brief Description
CT	Cycle time
C_1	Concentration of bromine in the anolyte
C_2	Concentration of bromine in the catholyte
d	Channel depth
D	Manifold diameter
$\mathcal{D}_{Br_2}$	Bromine diffusion coefficient
E_c	Energy capacity of the battery without auxiliaries
E_I	Energy input into the battery without auxiliaries
E_p	Total energy required for pumping
E_{pC}	Energy required for pumping on charge
E_{pD}	Energy required for pumping on discharge
E_S	Total required energy for shunt current position, $E_S = E_{SC}+E_{SD}$
E_{SC}	Energy required for shunt current protection on charge
E_{SD}	Energy required for shunt current protection on discharge
F	Faraday's constant
i_c	Charging current density
i_D	Discharge current density

Variable Name	Brief Description
i_{Sd}	Self-discharge current density due to bromine attack and hydrogen evolution
i_{H_2}	Self-discharge current density due to hydrogen evolution
I_{TC}	Terminal current on change
I_{TD}	Terminal current on discharge
ℓ	Channel length of the flow channel of width w and depth d
L	Electrode length
n_e	Number of electrons in bromine self-discharge reaction
N	Number of cells per stack
N_s	Number of stacks
ΔP_c	Pressure drop through a channel
ΔP_m	Pressure drop through the inlet and outlet manifold for one electrolyte
ΔP_T	Total pressure drop through the inlet and outlet manifold and through 2 channels for one electrolyte
Q_l	Volumetric flow rate per unit of electrode area
Q_T	Volumetric flow rate of one electrolyte
Q_{Tg}	Volumetric flow of one electrolyte
R_c	Channel resistance

Variable Name	Brief Description
R_e	Single cell resistance
R_m	Manifold resistance
t_{oC}	Tunnel current on charge
t_{oD}	Tunnel current on discharge
t_1	Anolyte chamber thickness of a cell
t_2	Catholyte chamber thickness of a cell
t_3	Bipolar electrode thickness
T_C	Time of charge
T_D	Time of discharge
V^o	Open-circuit voltage of a cell
V_{TC}	Total Voltage of a stack on charge
V_{TD}	Total Voltage of a stack on discharge
w	Channel width
W	Electrode width

GREEK SYMBOLS

β	Intermediate calculated value
δ_1	Diffusion layer thickness on anolyte side of separator
δ_2	Diffusion layer thickness on catholyte side of separator
δ_{Zn}	Diffusion layer thickness on deposited zinc
ε	Porosity of the

Variable Name	Brief Description
ε_1	Porosity of the anolyte chamber
ε_2	Porosity of the catholyte chamber
η_E	Energy efficiency of the battery including auxilaries
η_p	Electrolyte pump efficiency
λ	Separation thickness
λ_t	Intermediate calculated value
ρ	Electrolyte density
ρ_e	Electrolyte specific resistivity
τ	Separator tortuosity
τ_1	Anolyte tortuosity
τ_2	Catholyte tortuosity
μ	Viscosity

APPENDIX III

20-kWh (X-20) BATTERY TEST DATA

APPENDIX III

X20A BATTERY PERFORMANCE

CYCLE	DATE	LOADING (MAH/CMSQ)	COUL EFF (%)	VOLT EFF (%)	ENER EFF (%)	CHG CURR (AMPS)	CHG TIME (MIN)	DSC CURR (AMPS)	DSC TIME (MIN)	INPUT (WATT-HR)	OUTPUT (WATT-HR)
1	17SEP81	10.06	36.00	77.25	27.81	35.00	60.00	35.00	21.60	3380	940
2	17SEP81	7.47	44.87	70.11	31.46	52.00	30.00	35.00	20.00	2670	840
3	18SEP81	14.94	71.67	.	.	52.00	60.00	52.00	43.00	.	.
4	21SEP81	40.23	80.00	82.05	65.64	70.00	120.00	70.00	96.00	14000	9190
5	21SEP81	21.46	71.88	80.70	58.00	70.00	60.00	70.00	46.00	7500	4350
6	22SEP81	60.34	80.00	68.03	54.43	70.00	180.00	70.00	144.00	23150	12600
7	23SEP81	20.11	80.00	75.92	60.74	70.00	60.00	70.00	48.00	7590	4610
8	23SEP81	60.34	81.67	75.62	61.76	70.00	180.00	70.00	147.00	22670	14000
9	24SEP81	75.43	76.00	76.08	57.82	70.00	225.00	70.00	171.00	28570	16520
10	25SEP81	10.06	70.00	75.21	52.65	70.00	30.00	70.00	21.00	3780	1990
11	28SEP81	60.34	79.44	77.02	61.19	70.00	180.00	70.00	143.00	22700	13890
12	29SEP81	10.06	76.67	.	.	70.00	30.00	70.00	23.00	.	.
12.5	29SEP81	75.43	78.67	82.56	64.94	70.00	225.00	70.00	177.00	26500	17210
13	30SEP81	75.00	77.22	83.46	64.45	87.00	180.00	87.00	139.00	26300	16950
14	01OCT81	75.43	75.56	82.23	62.13	70.00	225.00	70.00	170.00	26300	16340
15	02OCT81	90.52	74.81	82.68	61.86	70.00	270.00	70.00	202.00	31800	19670
16	05OCT81	95.83	68.57	82.12	56.31	87.00	230.00	70.00	196.00	33600	18920
17	05OCT81	100.00	65.88	80.63	53.12	87.00	240.00	70.00	196.50	35150	18670
18	07OCT81	40.23	80.00	83.16	66.52	70.00	120.00	70.00	96.00	14100	9380
19	08OCT81	89.94	66.72	81.79	54.57	78.25	240.00	70.00	179.00	31520	17200
20	11OCT81	60.34	74.44	75.08	55.90	70.00	180.00	70.00	134.00	23240	12990
21	12OCT81	60.34	77.22	76.29	58.91	70.00	180.00	70.00	139.00	23000	13550
23	14OCT81	60.54	69.00	82.60	57.00	79.00	160.00	70.00	124.60	21000	11970
24	16OCT81	60.34	72.78	74.89	54.51	70.00	180.00	70.00	131.00	21080	11490
25	20OCT81	50.00	73.89	75.13	55.51	58.00	180.00	58.00	133.00	17240	9570
26	21OCT81	60.34	75.56	74.65	56.40	70.00	180.00	70.00	136.00	21170	11940
27	22OCT81	75.43	72.44	75.55	54.73	70.00	225.00	70.00	163.00	26220	14350
28	23OCT81	75.43	72.44	77.18	55.91	70.00	225.00	70.00	163.00	26040	14560
29	26OCT81	75.43	70.22	74.95	52.63	70.00	225.00	70.00	158.00	26240	13810
30	27OCT81	75.43	70.67	74.39	52.57	70.00	225.00	70.00	159.00	26250	13800
31	28OCT81	75.43	72.00	74.67	53.76	70.00	225.00	70.00	162.00	26300	14110
32	29OCT81	60.34	74.44	75.31	56.06	70.00	180.00	70.00	134.00	21120	11840
33	30OCT81	75.43	72.89	76.87	56.03	70.00	225.00	70.00	164.00	26130	14640
34	02NOV81	75.43	72.00	74.26	53.47	70.00	225.00	70.00	162.00	26520	14180
35	03NOV81	75.43	72.89	75.95	55.36	70.00	225.00	70.00	164.00	26300	14560
36	04NOV81	75.43	73.78	76.65	56.55	70.00	225.00	70.00	166.00	26190	14810
37	05NOV81	75.43	72.89	76.78	55.97	70.00	225.00	70.00	164.00	26480	14820
38	06NOV81	77.11	71.74	75.09	53.87	70.00	230.00	70.00	165.00	26990	14540
39	09NOV81	75.43	72.89	77.04	56.16	70.00	225.00	70.00	164.00	26070	14610
40	10NOV81	75.43	73.78	76.41	56.37	70.00	225.00	70.00	166.00	26290	14820
41	12NOV81	77.78	73.28	76.80	56.28	70.00	232.00	70.00	170.00	26920	15150
42	13NOV81	75.43	72.89	74.70	54.45	70.00	225.00	70.00	164.00	26520	14440
43	15NOV81	43.58	78.46	75.14	58.95	70.00	130.00	70.00	102.00	15300	9020
44	16NOV81	75.43	73.78	75.98	56.06	70.00	225.00	70.00	166.00	26240	14710
45	17NOV81	75.43	74.22	74.71	55.45	70.00	225.00	70.00	167.00	26490	14690
46	18NOV81	75.43	74.22	75.54	56.07	70.00	225.00	70.00	167.00	26480	14790
47	19NOV81	75.43	74.22	.	.	70.00	225.00	70.00	167.00	26360	.
48	20NOV81	75.43	73.78	.	.	70.00	225.00	70.00	166.00	26280	.
49	23NOV81	75.43	73.78	75.30	55.55	70.00	225.00	70.00	166.00	26480	14710
50	24NOV81	75.43	73.78	74.54	54.99	70.00	225.00	70.00	166.00	26550	14600
51	30NOV81	75.43	73.78	76.40	56.37	70.00	225.00	70.00	166.00	26220	14790

X20A BATTERY PERFORMANCE

CYCLE	DATE	LOADING (MAH/CMSQ)	COUL EFF (%)	VOLT EFF (%)	ENER EFF (%)	CHG CURR (AMPS)	CHG TIME (MIN)	DSC CURR (AMPS)	DSC TIME (MIN)	INPUT (WATT-HR)	OUTPUT (WATT-HR)
52	01DEC81	75.43	73.33	74.79	54.85	70.00	225.00	70.00	165.00	26510	14540
53	02DEC81	75.43	73.78	74.89	55.25	70.00	225.00	70.00	166.00	26480	14630
54	03DEC81	75.43	73.78	75.36	55.60	70.00	225.00	70.00	166.00	26350	14650
55	04DEC81	75.43	73.33	75.53	55.39	70.00	225.00	70.00	165.00	26360	14600
56	07DEC81	75.43	72.44	75.20	54.48	70.00	225.00	70.00	163.00	26470	14420
57	08DEC81	75.43	73.33	76.18	55.86	70.00	225.00	70.00	165.00	26350	14720
58	09DEC81	81.13	71.49	75.53	54.00	70.00	242.00	70.00	173.00	28390	15330
59	10DEC81	75.43	73.78	74.44	54.92	70.00	225.00	70.00	166.00	26510	14560
60	11DEC81	75.43	73.33	75.25	55.18	70.00	225.00	70.00	165.00	26440	14590
61	14DEC81	75.43	73.33	75.17	55.12	70.00	225.00	70.00	165.00	26360	14530
62	15DEC81	75.43	72.89	74.84	54.55	70.00	225.00	70.00	164.00	26470	14440
63	17DEC81	75.43	73.33	76.47	56.08	70.00	225.00	70.00	165.00	26250	14720
64	18DEC81	75.43	72.89	74.81	54.52	70.00	225.00	70.00	164.00	26520	14460
65	21DEC81	75.43	72.44	74.87	54.24	70.00	225.00	70.00	163.00	26550	14400
66	23DEC81	75.43	73.33	76.21	55.89	70.00	225.00	70.00	165.00	26230	14660
67	28DEC81	75.43	72.44	76.78	55.62	70.00	225.00	70.00	163.00	26160	14550
68	29DEC81	60.34	76.11	76.59	58.29	70.00	180.00	70.00	137.00	21050	12270
69	30DEC81	75.43	72.44	75.81	54.92	70.00	225.00	70.00	163.00	26420	14510
70	05JAN82	75.43	72.89	76.02	55.41	70.00	225.00	70.00	164.00	26260	14550
71	08JAN82	75.43	71.11	74.39	52.90	70.00	225.00	70.00	160.00	26560	14050
72	11JAN82	60.34	78.33	72.72	56.97	70.00	180.00	70.00	141.00	21820	12430
73	12JAN82	75.43	72.44	75.22	54.49	70.00	225.00	70.00	163.00	26500	14410
74	18JAN82	83.81	67.60	76.06	51.41	70.00	250.00	70.00	169.00	29330	15080
75	19JAN82	76.10	72.25	74.94	54.14	70.00	227.00	70.00	164.00	26780	14500
76	21JAN82	75.43	72.00	74.80	53.85	70.00	225.00	70.00	162.00	26590	14320
77	26JAN82	75.43	73.33	.	.	70.00	225.00	70.00	165.00	26360	.
78	28JAN82	75.43	72.44	76.01	55.06	70.00	225.00	70.00	163.00	26370	14520
79	02FEB82	80.46	69.17	74.61	51.61	70.00	240.00	70.00	166.00	28330	14620
80	04FEB82	75.43	72.89	78.03	56.87	70.00	225.00	70.00	164.00	26340	14980
81	08FEB82	75.43	71.56	74.96	53.63	70.00	225.00	70.00	161.00	26550	14240
82	09FEB82	75.43	72.00	74.69	53.78	70.00	225.00	70.00	162.00	26590	14300
83	11FEB82	75.43	70.67	76.84	54.30	70.00	225.00	70.00	159.00	26610	14450
84	16FEB82	75.43	72.00	76.45	55.04	70.00	225.00	70.00	162.00	26270	14460
85	18FEB82	75.43	73.78	76.13	56.17	70.00	225.00	70.00	166.00	26420	14840
86	19FEB82	76.10	72.69	74.80	54.37	70.00	227.00	70.00	165.00	26870	14610
87	22FEB82	75.43	73.33	74.56	54.68	70.00	225.00	70.00	165.00	26520	14500
88	23FEB82	76.44	73.25	74.85	54.82	70.00	228.00	70.00	167.00	26960	14730
89	24FEB82	75.43	74.67	76.03	56.77	70.00	225.00	70.00	168.00	26440	15010
90	25FEB82	75.43	73.78	74.43	54.91	70.00	225.00	70.00	166.00	26680	14650
91	26FEB82	75.43	73.33	73.31	53.76	70.00	225.00	70.00	165.00	26840	14430
92	01MAR82	75.43	73.78	76.15	56.18	70.00	225.00	70.00	166.00	26450	14860
93	02MAR82	75.43	74.22	75.71	56.19	70.00	225.00	70.00	167.00	26480	14880
94	03MAR82	75.43	74.22	75.81	56.27	70.00	225.00	70.00	167.00	26480	14900
95	04MAR82	77.44	76.19	75.69	57.67	70.00	231.00	70.00	174.00	27190	15680
96	05MAR82	75.43	76.89	75.64	58.16	70.00	225.00	70.00	173.00	26480	15400
97	08MAR82	75.43	77.33	75.75	58.58	70.00	225.00	70.00	174.00	26460	15500
98	09MAR82	75.43	76.44	73.97	56.54	70.00	225.00	70.00	172.00	26740	15120
99	10MAR82	75.43	74.22	74.00	54.92	70.00	225.00	70.00	167.00	26710	14670
100	11MAR82	75.43	75.11	73.64	55.31	70.00	225.00	70.00	169.00	26730	14780

PASS 121 DETACHED

APPENDIX IV

ANALYTICAL METHODS FOR DETERMINING QUATERNARY AMMONIUM IONS

APPENDIX IV

Analytical Methods for Determining Quaternary Ammonium Ions

In order to obtain meaningful material balance determinations on zinc-bromine battery electrolytes undergoing charge-discharge cycling, it became necessary to modify existing analytical methods for certain electrolyte species, and to develop new methods for others. New method development efforts focused on quaternary ammonium ion analysis, and for the most part, were carried out by Exxon Research Engineering Analytical and Information Division (AID) personnel[1]. Two modifications of a method for determining bromine in catholyte oil complexes, and three methods for the determination of quaternary ammonium ions are described briefly below.

Determination of Br_2 in Catholyte Oils

Initially, catholyte oil samples were agitated in an acidic aqueous mixture of KBr and KI. The KBr was present to facilitate breakdown of the oily phase via formation of tribromide ion, namely:

$$QNBr.xBr_2\ (oil) + x\ KBr\ (aq) \rightleftharpoons x\ KBr_3\ (aq) + QNBr\ (aq)$$

However, this process proved to be painfully slow. Oil samples as small as 0.1 ml required agitation for 24 hours or more before complete breakdown occurred, and the iodine, liberated by tribromide ion ($Br_3^- + 2I^- \rightleftharpoons 3\ Br^- + I_2$) could be titrated with thiosulfate.

Two observations led to procedures for rapid breakdown and dissolution of catholyte oil bromine into aqueous media. In the case of the acidic KBr-KI procedure, it was observed that a dark purple coating appeared on the surface of the oil drops shortly after they were added to the KBr-KI solution. This suggested that iodine was coating the oil, and, thus, inhibiting formation of aqueous tribromide ion. Therefore, we modified the procedure by adding the oil sample to aqueous acidic KBr in the absence of KI. After complete breakdown of the oil sample, which for 0.1-0.2 ml samples required only a few minutes, we added KI and titrated liberated iodine with thiosulfate ion.

The second procedure resulted from the observation that catholyte oil breaks down and dissolves rapidly in strong aqueous alkali (3-4M NaOH). This is due to the disproportionation of bromine in strong base as follows, namely:

$$Br_2 + 2\ NaOH \rightleftharpoons NaOBr + NaBr + H_2O$$

If, then, one reduces hypobromite with hydrogen peroxide ($OBr^- + H_2O_2 \longrightarrow Br^- + H_2O + O_2$), the sum of bromine and bromide contents of the oil sample can be determined (as bromide) by acidifying the solution and titrating with $AgNO_3$. A second oil sample is added to water and the bromine removed by gently warming for 10-15 minutes. The remaining solution contains the quaternary ammonium bromide content of the oil, which can be determined

by a second $AgNO_3$ titration. Thus, the bromine content of the oil is given by the following calculation, namely:

$$Br_2 \text{ (oil)} = 1/2 \text{ (Total bromide - QNBr)}.$$

Determination of Quaternary Ammonium Ions

Three methods were developed[1] for determining quaternary ion contents, both singly and in mixtures. Our present application for these analytical procedures is the determination of methylethyl morpholinium bromide (MEMBr) and methylethyl-pyrollidinium bromide (Q-14Br) in aqueous and oil phase electrolyte samples. The three methods developed by AID are ion chromatography, ^{13}C NMR spectroscopy, and ^{14}N NMR spectroscopy.

Ion chromatographic analysis of quaternary ammonium ions in Zn/Br_2 battery electrolytes requires complete removal of Zn^{+2} before absorption, separation, and detection of quaternary ammonium ions (as well as other monovalent cations present). This was accomplished by means of an anionic (chloride form) ion exchange resin that removes zinc as $ZnCl_4^-$. Although quite accurate MEMBR AND Q-14 Br analyses were obtained by ion chromatography of actual aqueous electrolyte samples, the necessity of removing zinc prior to analysis makes this method excessively time-consuming compared to NMR approaches.

NMR spectrographic methods for distinguishing between MEM^+ and $Q\text{-}14^+$ ions are based on the difference in chemical environment of the target nucleus (or nuclei) due to the difference in ring size (MEM^+=6, $Q\text{-}14^+$=5) and the presence (MEM^+) or absence ($Q\text{-}14^+$) of an ether linkage (-C-O-C). The ^{13}C NMR spectrum of an aqueous mixture of MEMBr and Q-14Br is presented in Figure AIV-1. Fortunately, only one of the eight peaks is due to overlap of MEM^+ and $Q\text{-}14^+$ ^{13}C absorptions. The remaining peaks may be integrated for purposes of quantification. Quite satisfactory results were obtained on analyzing electrolyte samples for quaternary ammonium bromides, in the presence of zinc bromide, by ^{13}C NMR spectroscopy.

On the basis of significantly lower required data acquisition times, ^{14}N NMR proved to be preferable to ^{13}C NMR for quaternary ammonium ion analysis. ^{13}C is present only to the extent of 1.1% in naturally occurring carbon, and it has a low NMR receptivity. On the other hand, ^{14}N is the predominant nitrogen isotope (99.6%) and has a receptivity greater than ^{13}C by a factor of 5.74. As an example of the consequences of these factors, a solution of quaternary ammonium ions that required 3.5 minutes of data acquisition to obtain an ^{14}N spectrum required 75 minutes for a ^{13}C spectrum. It should be pointed out that the ^{14}N nucleus has a spin number of 1, and, therefore, has a quadruple moment. For most nitrogen compounds (e.g. amines) quadrupolar relaxation effects wash out ^{14}N NMR resonance, yielding broad lines. Only quaternary ammonium ion nitrogen atoms given sharp ^{14}N lines, due to the spherically symmetric field at the nuclei.

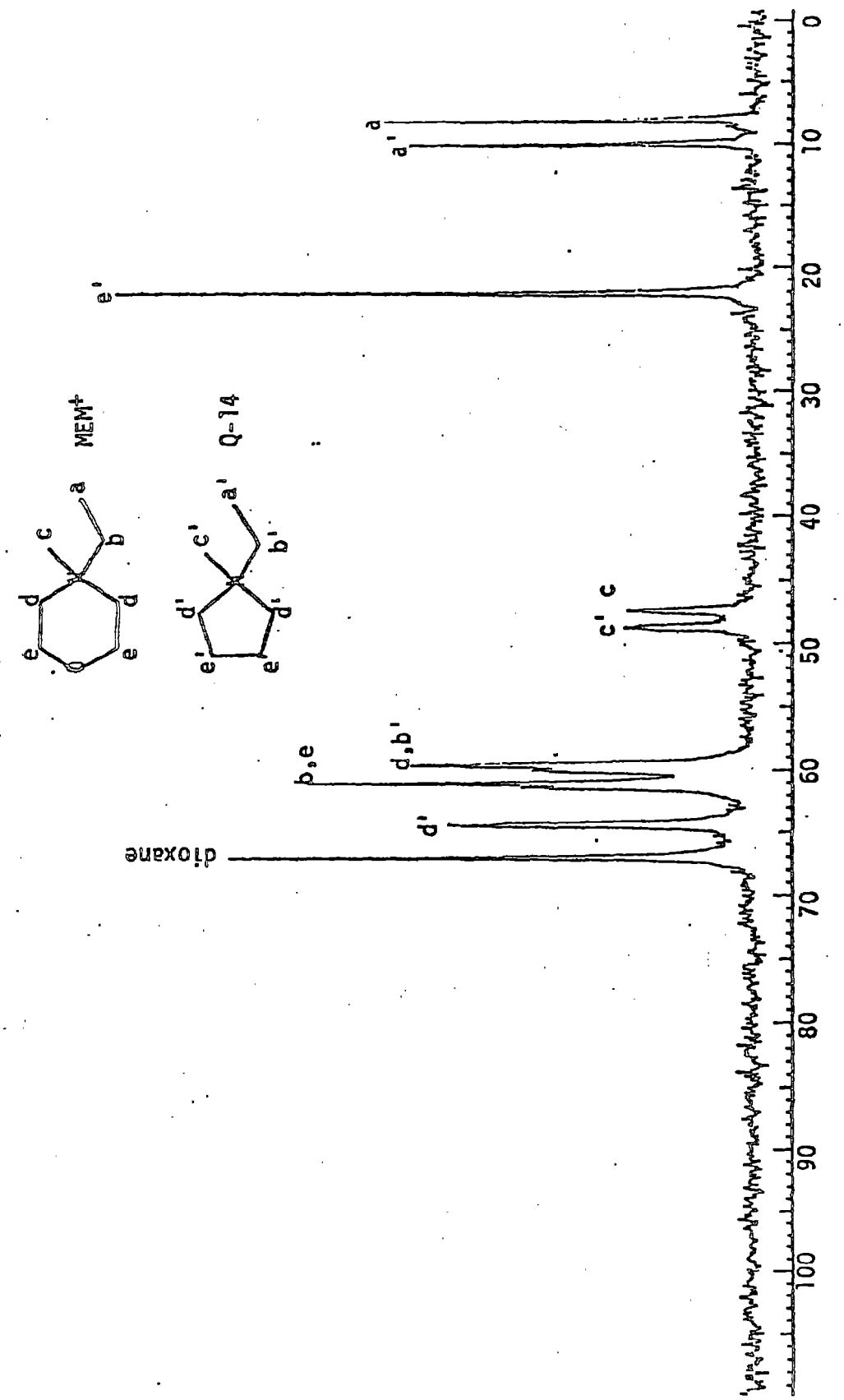

Figure AIV-1 ^{13}C NMR Spectrum of Mixed Quaternary Salts

The ^{14}N NMR spectrum of an aqueous mixture of MEMBr and Q-14 Br is shown in Figure AIV-2. The spectrum is very simple and can be easily quantified using NH_4^+ as an internal standard. ^{14}N NMR was also used to analyze quaternary ammonium ions in catholyte oil samples, with $(C_2H_5)N^+$ (in $HCCl_3$) as an internal standard (Figure AIV-3).

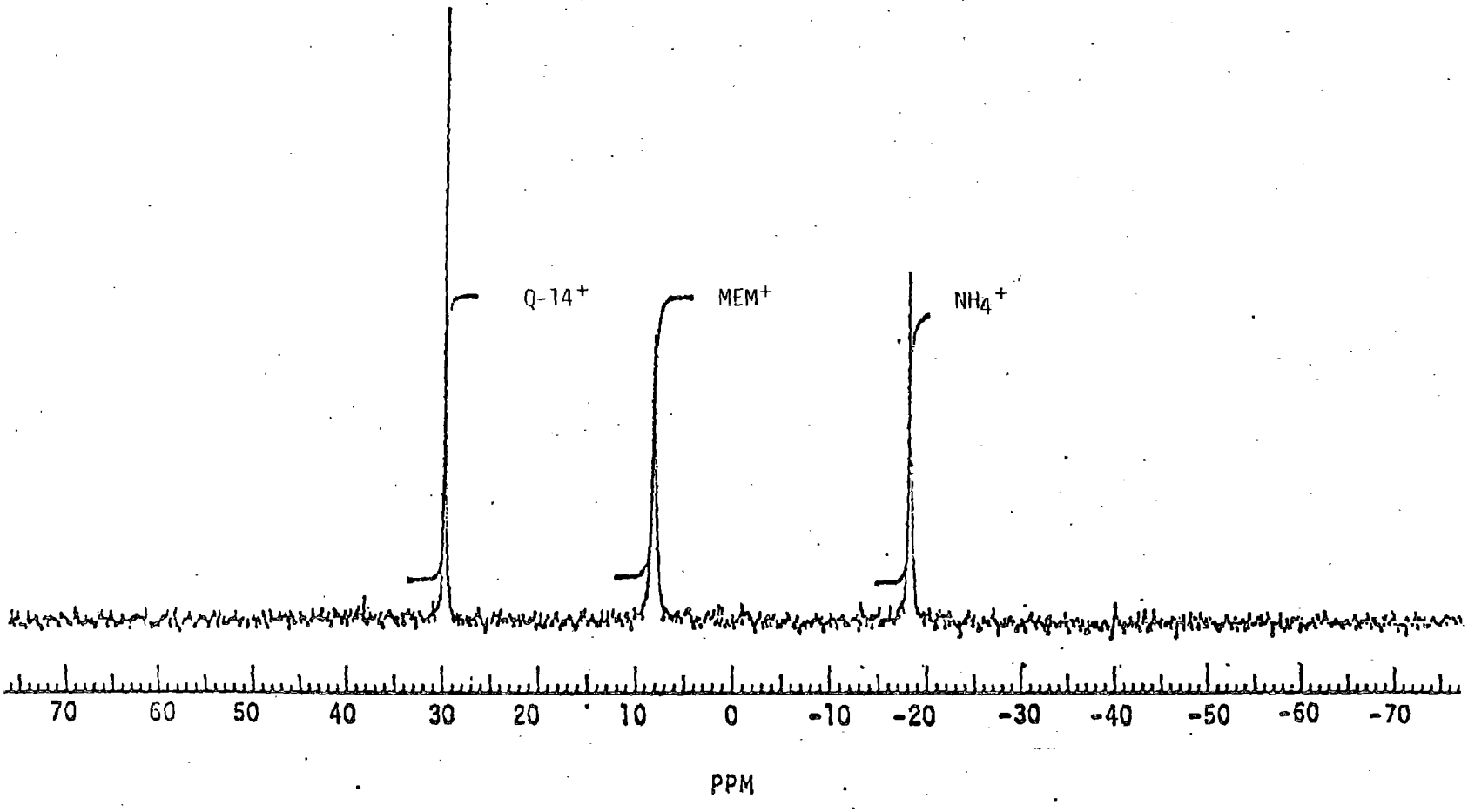

Figure AII-2 ^{14}N NMR Spectrum of Mixed Quaternary Salts

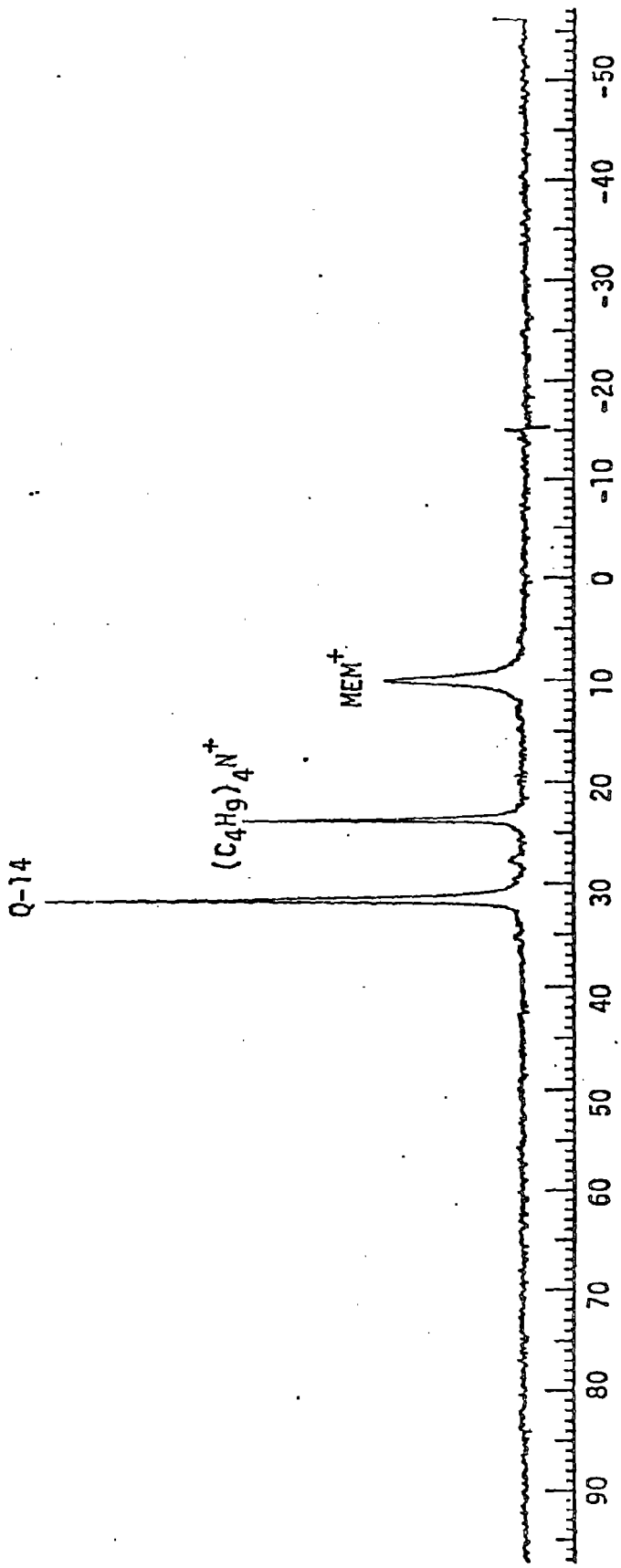

Figure AIV-3 ^{14}N NMR Spectrum of $HCCl_3$ Solution of Catholyte Oil